UNIVERSITÀ
degli STUDI
di CATANIA

DEPARTMENT OF BIOLOGICAL, GEOLOGICAL AND ENVIRONMENTAL SCIENCES
PH.D. SCHOOL IN EARTH AND ENVIRONMENTAL SCIENCES
CYCLE XXXVIII°

ALBERTO SALERNO

REMOTE SENSING AND GIS APPROACHES FOR ELABORATING SENTINEL-2 IMAGES: APPLICATION ON VOLCANIC AREAS

Tutor: Prof. Stefano Catalano
Co-Tutor: Dr. Harald Van der Werff
Prof. Marco Viccaro
Coordinators: Prof. ssa Rosanna Maniscalco

Academic Year 2024/25

INDEX

1. Introduction

In the volcanic areas, understanding the relative chronology of volcanic units is fundamental for reconstructing the eruptive history, assessing volcanic hazards, and supporting land use and emergency planning. In many volcanic settings, especially in remote or inaccessible areas, traditional field-based methods for dating lava flows (e.g., radiometric dating, stratigraphic correlation) are logistically challenging, time-consuming and expensive (Trusdell, 1995). This thesis arises from the need for a cost-effective, scalable, and remote methodology to estimate the relative age of lava flows, using satellite-based reflectance data. In particular, the launch of the Sentinel-2 satellites enabled unprecedented access to frequent, high-resolution multispectral imagery, which can be used to infer surface properties that evolve over time after an eruption. These properties, such as reflectance changes in the visible, near-infrared (NIR), and shortwave infrared bands, are linked to physical and chemical weathering, biological colonization, and surface alteration processes (Pieri & Abrams, 2004; Gillespie et al., 1986). The motivation behind this study is to test and apply reflectance-based techniques to identify relative age groupings of basaltic lava flows, using Sentinel-2 imagery as a remote sensing tool. The approach is designed to provide a practical framework that could eventually be extended to other volcanic areas, especially where dating constraints are poor or fieldwork is limited by safety or accessibility (Ramsey & Flynn, 2004). Volcanic terrains are composed of successions of lava flows with varying degrees of alteration and surface roughness, depending on their emplacement age and post-eruption evolution. Over time, lava surfaces become smoother, lighter in colour, and biologically colonized, leading to gradual increases in surface reflectance particularly in the visible and NIR bands (Gillespie et al., 1986; Rowland & Walker, 1987). These changes make spectral reflectance a promising proxy for surface age.

1.1 Volcanoes and Satellite-Based Lava Flow Dating

Throughout geological time, the volcanic activity has played a fundamental role in shaping the Earth's surface in most of the geodynamically active regions of the planet. The study of eruptive history of volcanic regions, thus, provides crucial information not only about the evolution of volcanism, but also about the broader associated geodynamic processes that affect active geodynamic settings. A reliable chronostratigraphy of lava units, essential for validating models of volcanic activity recurrence and volcanic hazard appraisal, have been obtained by traditional methods, combining field mapping supported by radiometric data. This accurate approach, which requires decades of study, has often focused on volcanic areas close to populated regions (e.g. the volcanic areas of southern Italy; De Beni et al., 2011; Orsi, 2022), where minimizing the related risks justifies the high costs of research. In recent years, the use of satellite remote sensing has revolutionized the ability to monitor and analyse volcanic landscapes. High-resolution satellite imagery, combined with advanced spectral analysis techniques, enables researchers to estimate the relative age of lava flows over large, often inaccessible areas. Volcanoes are distributed across the globe, primarily along tectonic plate boundaries, in subduction zones, mid-ocean ridges, and hotspots. Regions such as the Pacific Ring of Fire, the East African Rift, and the Icelandic volcanic system are characterized by intense volcanic activity that continuously reshapes the landscape. Volcanic eruptions can have significant impacts on human populations, infrastructure, climate, and ecosystems, making the study and monitoring of volcanic behaviour a key priority in geosciences. Lava flows represent one of the most common and persistent products of volcanic eruptions. Their ages help volcanologists reconstruct eruption sequences, estimate recurrence intervals, and predict future activity. In addition, the sheer scale of volcanic fields often makes it difficult to achieve comprehensive coverage. Satellite remote sensing provides a transformative solution to these challenges. Through the analysis of multispectral and hyperspectral data, researchers can detect mineralogical and chemical changes on the surface of lava flows that occur as they age. The oxidation of iron minerals, for

example, leads to measurable changes in spectral signatures, which can be quantified to estimate relative lava flow ages. Moreover, satellite-based methods allow for consistent, repeatable measurements over time and can be applied across vast areas that are otherwise inaccessible. The ability to date lava flows from space has significant implications for volcanic risk management. It enables authorities and scientists to map and monitor volcanic fields continuously, identify potentially active flows, and integrate age data into hazard models. Furthermore, the development of robust methodologies for satellite-based age estimation could contribute to the field of planetary geology, offering tools that can be applied to the study of extraterrestrial volcanic features on planets such as Mars and Venus. In summary, understanding global volcanic activity and developing techniques to date lava flows via satellite imagery are crucial steps in advancing both scientific knowledge and practical hazard mitigation strategies. This research addresses these needs by proposing and validating a novel methodological framework for estimating lava flow ages through satellite image analysis.

1.2 Remote sensing for geological purposes

The advent of satellite remote sensing technologies has revolutionized the way we study and understand the Earth's surface, enabling a vast array of applications across multiple scientific disciplines. Among the myriad satellite systems, the European Space Agency's (ESA) Sentinel-2 mission, with its Sentinel-2A and Sentinel-2B satellites, are the present-day sensors that do, with Landsat 8 and 9, routinely Earth observation. The role of satellite imagery in geological studies has gained prominence over the past few decades, with remote sensing offering a non-invasive means of mapping, monitoring, and analysing geological features. In particular, the Sentinel-2 satellites constellation of the European Space Agency high spatial resolution, wide swath width, frequent revisit times (every 5 days at the equator when two satellites are active), and extensive spectral coverage make it an invaluable resource for geologists seeking to understand Earth's dynamic processes (Drusch et al., 2012; Kervyn et al., 2010). The Sentinel-2 satellite, equipped with the MultiSpectral Instrument (MSI), provides 13 spectral bands ranging from the visible to the shortwave infrared (SWIR), enabling multi-band reflectance analysis. The use of multispectral images on volcanic regions not only serve to identify the specific spectral signature of the volcanic terrains, very different from that of other geological substrata, but also to evidence its systematic variation between volcanic units of different compositions and ages. Understanding the rules governing the relationship between age and spectral signature of lava would provide an important proxy for the relative dating of volcanic terrain, responding to the need for a rapid method to outline eruptive chronology, landscape evolution, and associated geological hazard. This thesis focuses on examining spectral indices developed starting from raw bands images especially in the VNIR (visible and near-infrared) and SWIR (shortwave infrared) wavelength ranges, to identify systematic patterns that correlate with lava surface freshness, thus allowing the classification of flows into relative age. The basic assumption is that spectral reflectance changes systematically with surface ageing, as a result of physical and chemical weathering, sediment deposition, biological colonization, and thermal degradation of glassy

surfaces (Rowland & Walker, 1987; Trusdell, 1995; Ramsey & Flynn, 2004). On active volcanoes, the continuous resurfacing due to the emplacements of new lava flows or pyroclastic deposits, cause abrupt changes of the reflectance. Younger lava flows tend to exhibit lower reflectance in visible and near-infrared bands due to their rough, non-weathered surfaces, while older flows generally show higher albedo values, influenced by lichen growth, oxidation, and surface smoothing (Gillespie et al., 1986; Pieri & Abrams, 2004). The variations of the spectral reflectance will be examined in detail on selected volcanic fields characterized by well-documented eruptive histories (e.g., Kilauea, Stromboli, Etna, or Reykjanes), where the relative ages of lava flows have been already independently constrained. This approach aims at validate a cost-effective method for mapping lava flows, according to their age, thus providing a scalable framework for assessing volcanic hazards and planning monitoring strategies in active volcanic regions.

1.3 Study Areas

This research focuses on four volcanic areas that are representative of different tectonic settings, eruption styles, and geological characteristics: Mount Etna (Italy)(Fig. 1), Stromboli (Italy) (Fig. 2), the Grindavík region (Iceland) (Fig. 3) and Hawai'i Island (Hawaii) (Fig. 4).

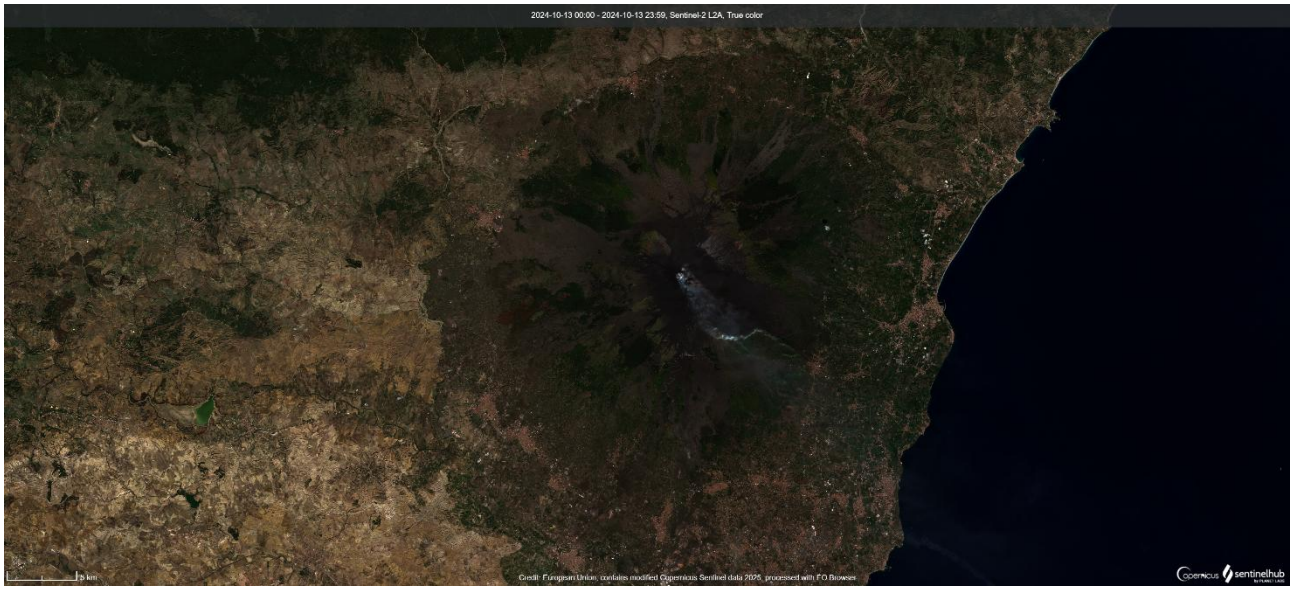

Fig. 1 Sentinel 2 image true colour of Mt. Etna Volcano (Sicily, southern Italy).

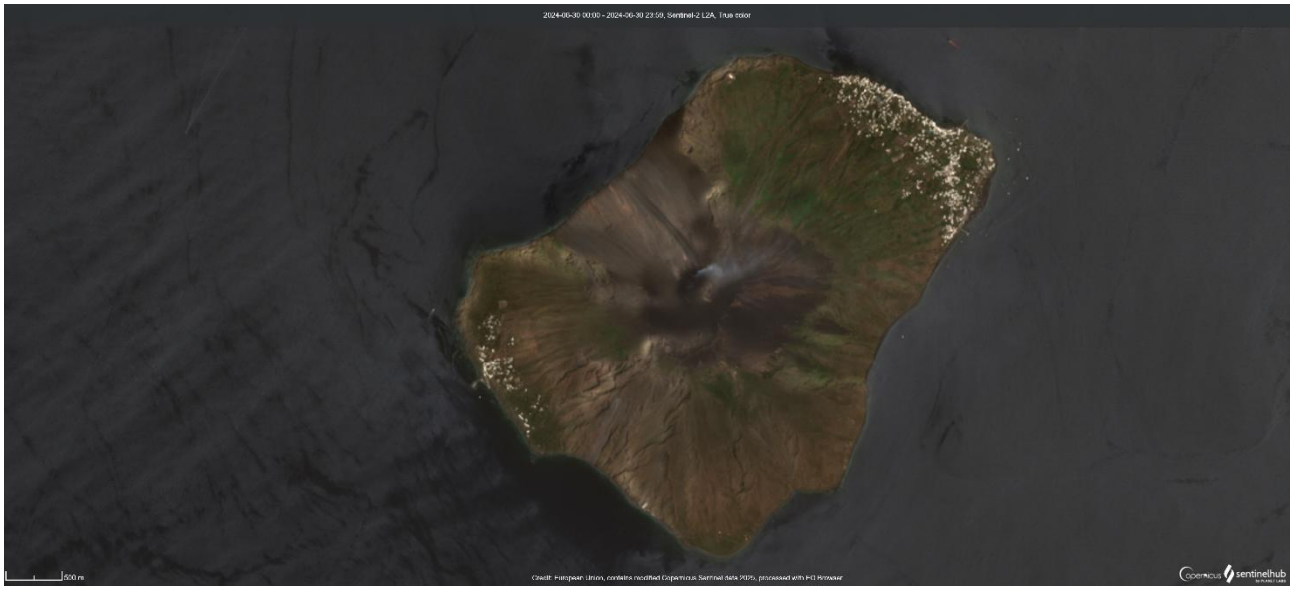

Fig. 2 Sentinel 2 image true colour of Stromboli volcano (Sicily, southern Italy).

Fig. 3 Sentinel 2 image true colour of the Grindavik region (Iceland).

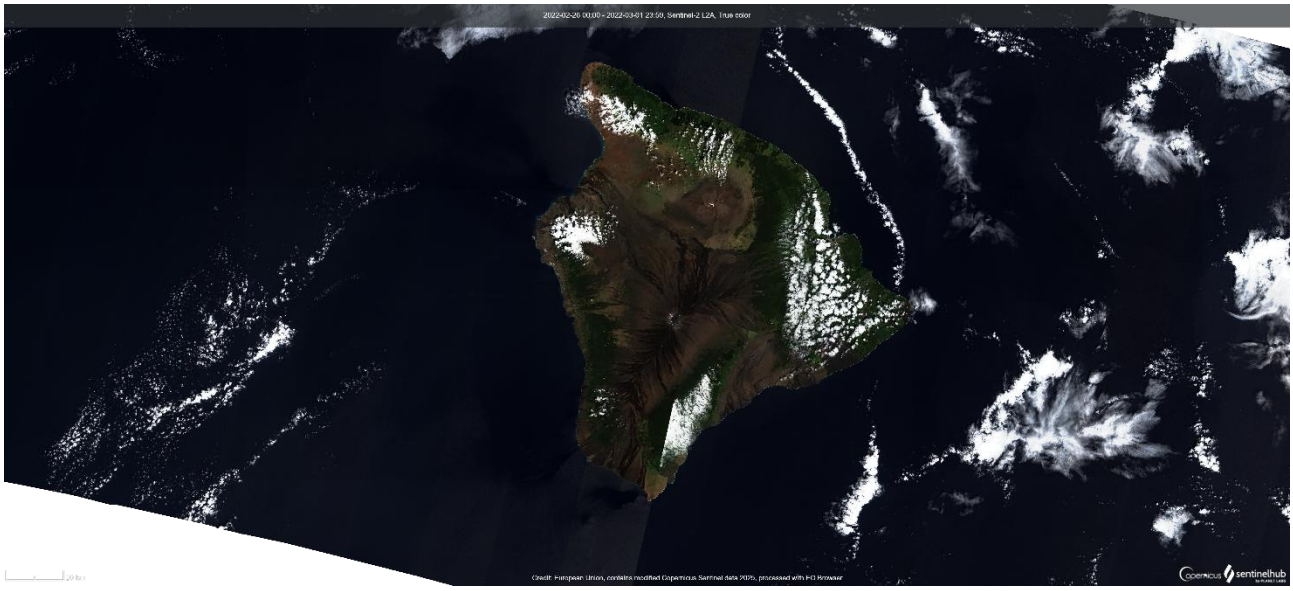

Fig. 4 Sentinel 2 image true colour of the Hawai'i Island (Hawaii, USA).

Mount Etna

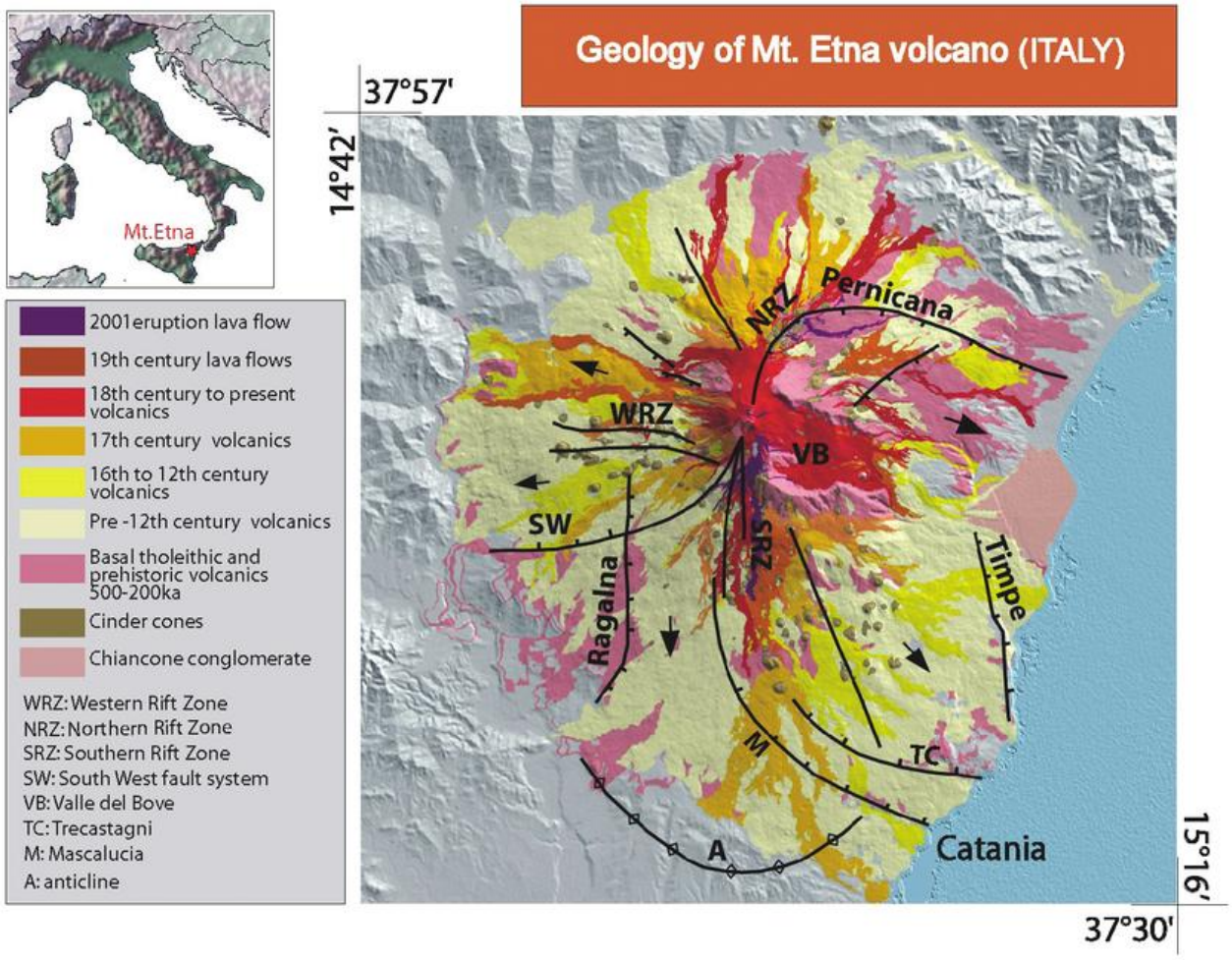

Fig. 5 Schematic map of Etna volcano main features (Branca & Del Carlo, 2005).

Mount Etna, located on the eastern coast of Sicily, is the largest and most active volcano in Europe and one of the most studied stratovolcanoes in the world. Rising to an elevation of approximately 3,324 meters above sea level (subject to variations due to eruptive activity), Etna is characterized by persistent eruptive behaviour, complex internal dynamics, and a long geological history that spans several hundred thousand years (Behncke & Neri, 2003; Branca & Del Carlo, 2005; De Beni et al., 2011). Etna's activity's products are primarily mafic in composition (i.e., basalts, hawaiites and K-trachybasalts), though more evolved magmas (mugearites, benmoreites and trachytes) have been occasionally erupted in the past. Etna lies at the convergent boundary between the African and Eurasian plates (Serpelloni et al., 2007), within a tectonically

active region representing the transition between the relict of a subduction zone (Ionian basin-Calabrian arc system in the central Mediterranean) and the African paleo-margin (Hyblean foreland) (Dewey et al., 1989; Lentini et al., 1994). Etna's magmatism is not directly related to subduction processes but is rather attributed to complex interactions between Mantle upwelling and the related lithospheric extension with other regional tectonics at the hanging-wall of the Ionian subduction zone (Gvirtzman & Nur, 1999; Faccenna et al., 2007). The volcano sits atop a lithospheric flexure zone and is affected by systems of regional faults (e.g. that facilitate the magma ascent and influence the localization of eruptive fissures (Azzaro et al., 2012). Mount Etna's volcanic edifice is the result of multiple overlapping construction phases, including the remnants of ancient stratovolcanoes such as Trifoglietto and Ellittico (Branca et al., 2011). The modern edifice has developed over the last 57,000 years and comprises summit craters, extensive flank fissure systems, and large pyroclastic and lava flow deposits. Major collapse events, such as the Valle del Bove depression on the eastern flank, are interpreted as gravitational sector failures (Rust & Neri, 1996), with potential implications for future flank instability. Etna is known for both summit and flank eruptions, with eruptive styles ranging from Strombolian and effusive activity to sub-Plinian explosive episodes. Flank eruptions are often fed by dike intrusions propagating from the central conduit and can pose significant hazards to populated areas on the lower slopes. Etna is also notable for its frequent paroxysmal activity at the summit craters, including episodes of lava fountaining, intense gas emission, and ash plumes that often disrupt air traffic (Corsaro et al., 2017; Giuffrida & Viccaro, 2017; Giuffrida et al., 2023). Geophysical monitoring indicates a persistent and dynamic magma storage system at various depths, with connections between deep magma reservoirs (>10 km) and shallow conduits (<3 km) (Bonaccorso et al., 2004; Viccaro et al., 2019). Due to its continuous activity, accessibility, and multidisciplinary monitoring network (e.g., INGV National Institute of Geophysics and Volcanology), Etna serves as a natural laboratory for studying volcanic processes, hazard assessment, and the interplay between tectonics and volcanism. Its well-documented history and ongoing unrest

make it a critical site for advancing models of magma migration, edifice deformation, and eruptive forecasting.

Mount Etna was chosen as a training ground for the method thanks to the well-mapped variegated deposits that goes from clay to pyroclasts, to lava flows, to hydrothermal deposits, the idea is to see which one fits the timeline best. Although the continuous activities create a time series of lava flows that allows to calibrate the method with a high resolution.

Stromboli

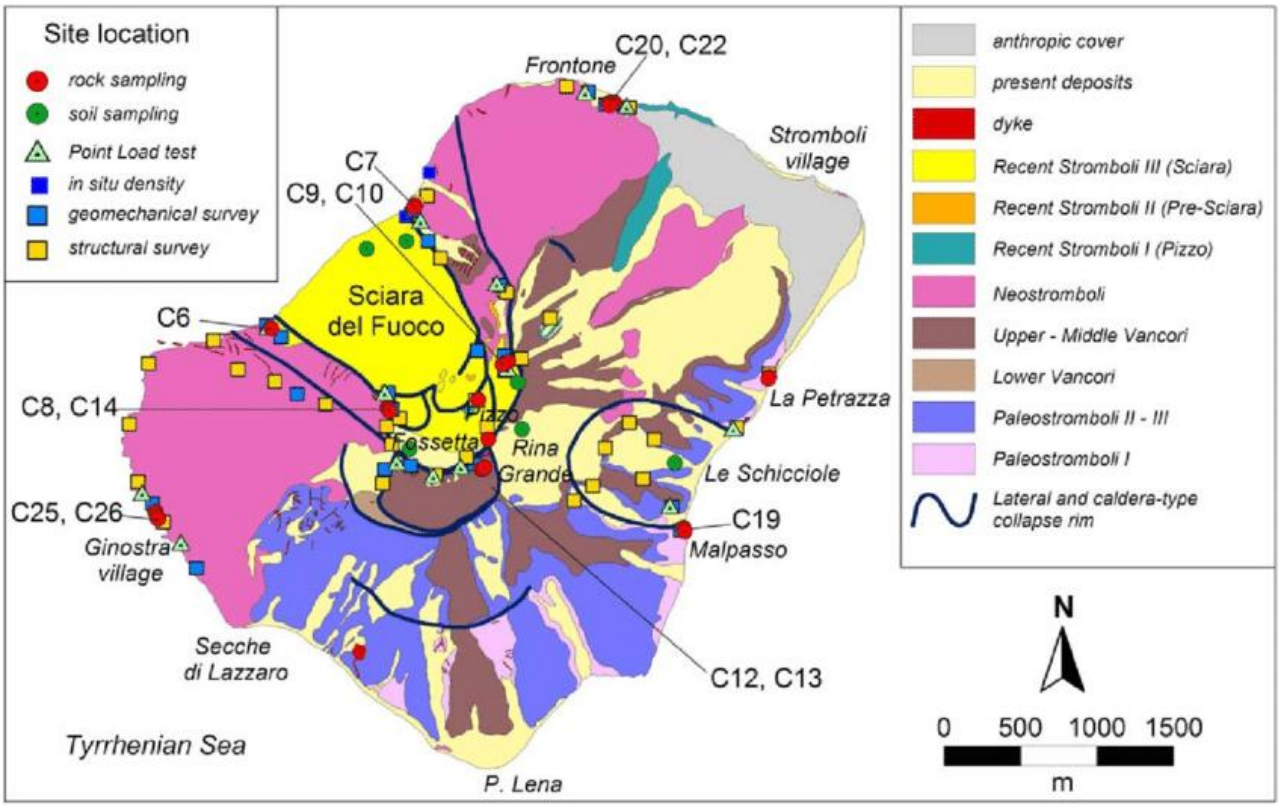

Fig. 6 Schematic map of Stromboli volcano main features (Romagnoli et al., 2009).

Stromboli, located in the Aeolian Islands (southern Tyrrhenian Sea, Italy), is one of the world's most iconic volcanoes due to its persistent activity and well-defined eruptive style. Known as the type locality for "Strombolian" eruptions, Stromboli has been in nearly continuous activity for over 2,000 years, making it a key natural laboratory for volcanological research (Rosi et al., 2000; Francalanci et al., 2013). Located at the northeastern edge of the Aeolian arc, it formed in a complex geodynamic environment

involving the subduction of the Ionian slab beneath the Calabrian arc and local lithospheric back-arc extension. The island represents the emergent portion of a large volcanic edifice, most of which is submerged and rooted on the oceanic crust of the Tyrrhenian Basin (Barberi et al., 1974; Calanchi et al., 1993). The volcano sits atop a NNW–SSE trending fault system and displays a prominent summit crater complex and a large horseshoe-shaped depression known as the “Sciara del Fuoco”, formed by multiple sector collapses over the past 13,000 years (Tibaldi, 2001). Stromboli's magmas are primarily calc-alkaline basaltic to basaltic andesite, typically rich in phenocrysts of plagioclase, clinopyroxene, and olivine. Magmatic differentiation is controlled by magma recharge, crustal contamination, and degassing in a vertically zoned plumbing system (Pichavant et al., 2013). Geochemical and petrological data suggest the presence of multiple magma reservoirs, with shallow-level storage (~2–4 km) feeding the persistent explosive activity (Métrich et al., 2005). Stromboli’s eruptions are dominated by mild explosive activity short-lived bursts of gas-rich magma occurring every few minutes from the summit craters. These Strombolian explosions eject scoria, lapilli, and volcanic bombs, resulting typically low in VEI (Volcanic Explosivity Index) (Harris & Ripepe, 2007). The explosions are driven by the ascent and bursting of large gas slugs, as evidenced by both visual and infrasonic monitoring. In addition to its persistent activity, Stromboli occasionally undergoes paroxysmal events, characterized by higher explosivity, lava fountaining, and ballistic ejection (Rosi et al., 2006). These events, such as those of July 2019 and October 2022, pose significant hazards to residents and tourists, especially due to their sudden onset. Paroxysms are potential triggers for flank collapses and consequent tsunami generation (Viccaro et al., 2021; Romagnoli et al., 2022). Effusive eruptions also occur. They typically fed lava flows that canalize and rapidly descend towards the sea along the very steep Sciara del Fuoco. Also, these flows can trigger partial landslides of the pyroclastic deposits of the steep volcanic flank, generating small to moderate tsunamis. Monitoring of the Sciara del Fuoco has revealed gradual flank instability and gravitational spreading, raising concerns over large-scale sector collapse scenarios (Chiocci et al., 2008; Di Traglia et al., 2014). Stromboli is one of the most heavily

instrumented volcanoes in Europe, monitored by INGV (National Institute of Geophysics and Volcanology) with a network of seismic, thermal, infrasonic, and geodetic sensors. The integration of remote sensing, drone imagery, and real-time data allows for effective short-term forecasting of changes in eruptive activity. Nevertheless, the high tourism density and the potential for sudden hazardous events make Stromboli a challenging environment for risk mitigation and civil protection strategies (Calvari et al., 2020).

Stromboli volcano has a large quantity of pyroclastic rocks compared to lava flows, this is useful to understand if the pyroclasts have different reflectance values. Stromboli island has a smaller area compared to the other three volcanoes and the moisture of the sea can have an important role in the reflectance analysis.

Grindavík Region

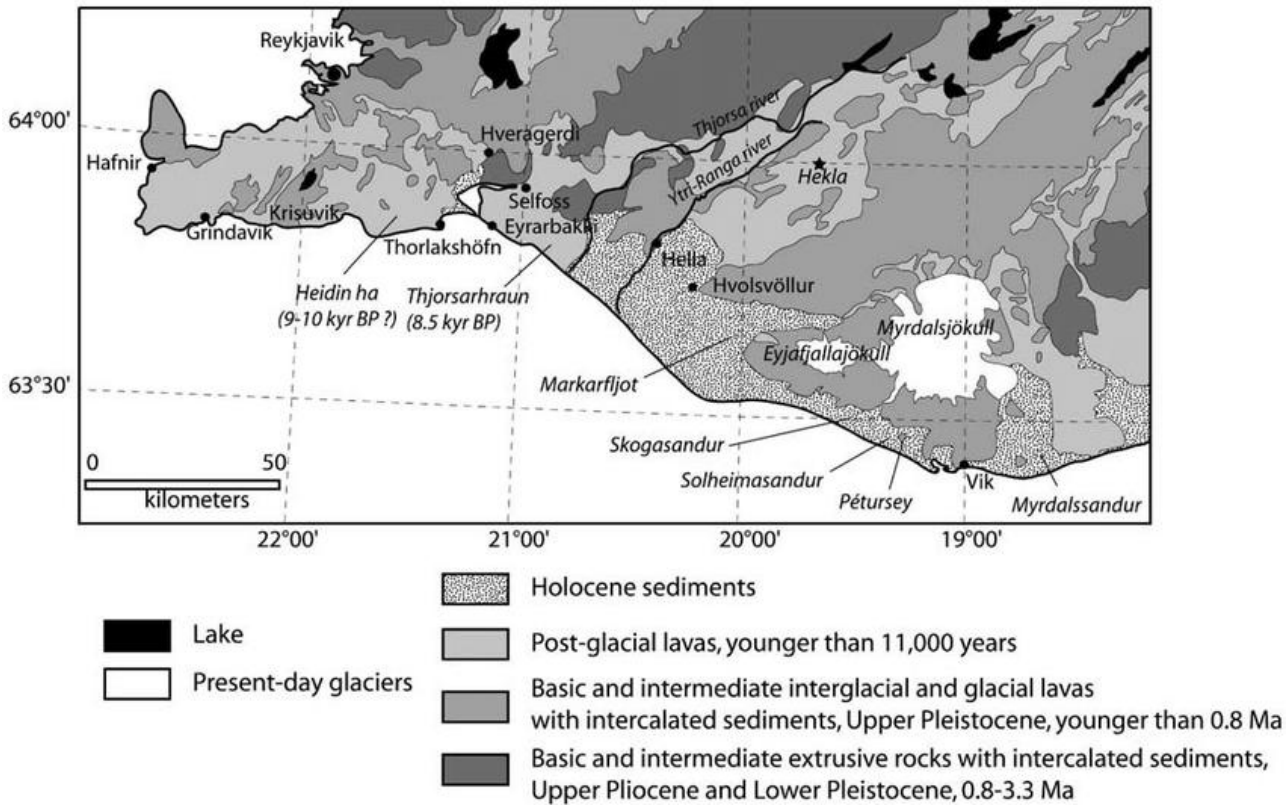

Fig. 7 Schematic map of Reykjanes Peninsula main features (Biessyet al., 2008)

The Grindavík area, located on the Reykjanes Peninsula in southwest Iceland, lies within the Reykjanes Volcanic Zone (RVZ) a seismically and volcanically active

region that represents the landward continuation of the Mid-Atlantic Ridge. This tectonic domain is governed by the divergent boundary between the North American and Eurasian plates, resulting in high levels of crustal extension, associated with frequent earthquakes and diffuse basaltic volcanism (Saemundsson, 1979; Einarsson, 2008). The Reykjanes Peninsula comprises a set of en-echelon volcanic features, oriented NE–SW, including the Reykjanes, Svartsengi, Krýsuvík, Fragadalsfjall, Brennisteinsfjöll, and Hengill systems. Grindavík is located near the Krýsuvík–Trölladyngja fissure swarm, one of the most active volcanic segments in southwestern Iceland (Sæmundsson et al., 2020). The tectonic regime is characterized by rift-parallel normal faults, fissure swarms, and frequent dyke intrusions, as well as high-temperature geothermal systems. Volcanic activity in this area is typically basaltic and fissure-fed, producing lava flows, spatter cones, and shield volcanoes with minimal explosive activity (Thordarson & Larsen, 2007). Lavas from the Reykjanes Peninsula are typically tholeiitic basalts derived from shallow mantle sources, showing minor heterogeneities related to melting depth and lithospheric contamination (Jakobsson et al., 1978; Peate et al., 2010). Recent eruptive products from nearby systems, including the Fagradalsfjall eruption (2021–2023), have provided new insights into magma recharge, mixing, and ascent pathways in the RVZ (Bagnardi et al., 2023). Petrological studies show evidence of rapid magma transport from depth (~15–20 km) to the surface, and the lack of significant storage suggests that short-lived intrusions are responsible for triggering surface eruptions (Gurenko et al., 2022). The Grindavík region has experienced heightened unrest since 2021, with a series of seismic swarms, ground deformation, and volcanic eruptions, especially around Fagradalsfjall and the Sundhnúkur crater row (Gíslason et al., 2024). The dyke intrusions and subsequent eruptions have followed pre-existing structural lineaments and have had significant implications for geohazards and urban planning, as the town of Grindavík is located near active fissure systems. The November 2023 dyke intrusion beneath Grindavík led to substantial subsidence and ground cracking, forcing evacuations. This event was part of a broader volcanic reactivation cycle on the peninsula, interpreted as a response to long-term stress accumulation and episodic mantle melt supply (Sigmundsson et al.,

2022). The area surrounding Grindavík hosts several high-temperature geothermal fields, including Svartsengi, which powers the Blue Lagoon spa. These systems are fed by hydrothermally altered basaltic rocks, high heat flow, and fractured permeability structures associated with active faults and fissures (Arnórsson et al., 2007). Surface features include recent lava fields, rootless cones and tectonic grabens, all characteristic of a rifted volcanic terrain. The geology is accessible and well-preserved due to Iceland's young lithosphere and minimal vegetation cover, making it an ideal site for structural and volcanological field studies.

Grindavik is the northernmost of the studied areas, this consent to calibrate the method to different latitudes and to verify the impact of colder environments. Although the recent activity products overlap volcanic rocks older than a thousand years.

Hawai'i Island

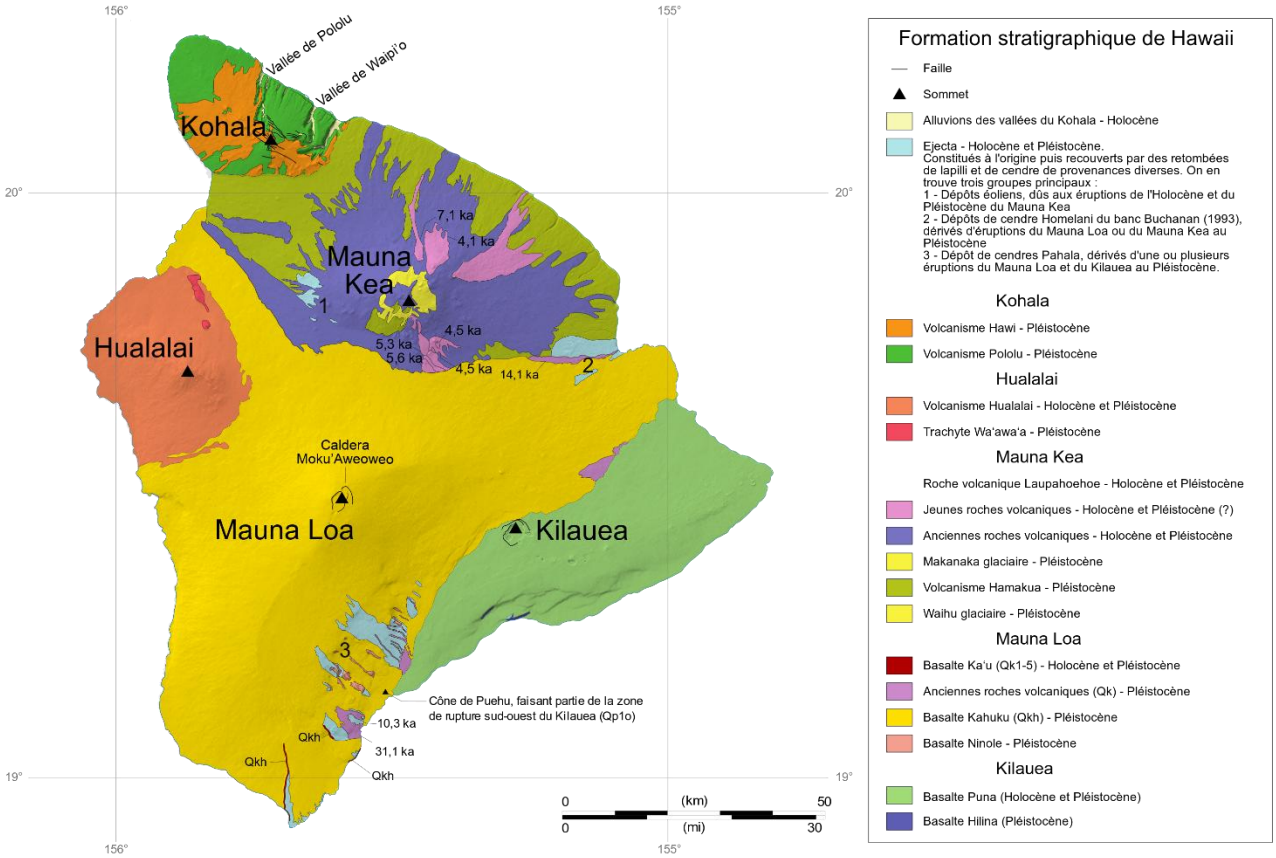

Fig. 8 Schematic map of Hawai'i Island main features

Hawai‘i Island, the southeasternmost and geologically youngest island in the Hawaiian archipelago, is a classic example of intraplate volcanism associated with a stationary mantle plume commonly referred to as the Hawaiian hotspot (Wilson, 1963; Garcia et al., 2007). The island is constructed by the coalescence of five basaltic shield volcanoes: Kohala, Mauna Kea, Hualalai, Mauna Loa, and Kilauea, each representing a different stage of the Hawaiian volcanic lifecycle (Clague & Dalrymple, 1987). These volcanoes exhibit the tholeiitic basaltic composition typical of ocean island basalts (OIB) and are predominantly shaped by effusive eruptions that produce voluminous pahoehoe and ‘a‘a lava flows (Macdonald et al., 1983). Over time, successive lava flow sequences have formed the island’s extensive volcanic terrains, with some flows extending tens of kilometres from summit vents to the coastline.

- Mauna Loa is the largest volcano on Earth by volume, reaching over 10,000 meters in height when measured from its submarine base. It remains an active shield volcano, with a well-documented eruptive history including 34 eruptions since 1843 (USGS, 2022). Its eruptions typically involve high-volume, low-viscosity basaltic lava and can rapidly affect extensive areas due to steep upper slopes and well-developed rift zones (Lockwood & Lipman, 1987).

- Kilauea, located to the southeast of Mauna Loa, is one of the most active volcanoes on the planet, with near-continuous activity throughout the late 20th and early 21st centuries. The 2018 lower East Rift Zone eruption resulted in major summit collapse, extensive lava flows, and significant geochemical and seismic changes (Neal et al., 2019). Kilauea is notable for its active caldera processes, summit deflation-inflation cycles, and sustained SO_2 emissions (USGS, 2024).

- Mauna Kea, the tallest mountain in Hawai‘i (4,207 m above sea level), is considered dormant and represents a more evolved stage of volcanic development. It features post-shield stage volcanism, including alkalic lava

flows and cinder cones, as well as evidence of glaciation during the Pleistocene (Porter, 1979; Wolfe et al., 1997).

- Hualalai, though last erupted in 1801, remains potentially active, as indicated by recent seismic activity and CO_2 degassing (USGS, 2023). Its lavas are more alkalic than those of Kilauea and Mauna Loa and it presents a hazard to densely populated areas such as the Kona coast (Moore & Clague, 1991).

- Kohala, the oldest and only extinct volcano on the island, last erupted approximately 120,000 years ago and is characterized by deeply eroded flanks and well-preserved paleo-soils and colluvial deposits that provide insights into long-term island weathering processes (McDougall & Swanson, 1972; Chadwick et al., 2008).

In addition, the submarine volcano Kamaʻehuakanaloa (formerly Loʻihi), lying to the southeast of the island, is currently in the pre-shield stage of development. Although its summit is still ~970 meters below sea level, repeated seismic swarms and hydrothermal activity confirm its growth as an emerging volcanic edifice, potentially the next island in the Hawaiian chain (Davis & Clague, 1990; Garcia et al., 2006). In sum, Hawaiʻi Island presents a complete and accessible stratigraphic and morphological record of hotspot volcanism, from submarine volcanic initiation through post-shield erosion. The island's volcanoes are key to understanding mantle plume dynamics, magma differentiation, rift zone propagation, and the geomorphic evolution of volcanic islands. Their ongoing activity continues to provide critical data for volcanological research, hazard assessment, and geodynamic modelling (Clague & Sherrod, 2014).

Hawai'i island is the southernmost as well as the biggest area of this study, the continuous craters activity creates a timeseries of lava flows perfect to test the methodology resolution.

1.4 The Copernicus Program and Sentinel-2 satellites

The Copernicus Program is established and managed by the European Commission in partnership with the European Space Agency (ESA). Its core mission is to deliver free, accessible, and continuous environmental monitoring data to support climate research, disaster management, land and ocean monitoring, atmospheric composition analysis, and emergency response (European Commission, 2015). Copernicus is built upon a constellation of Sentinel satellites (Fig. 9), each designed with specialized sensors to observe various components of the Earth system. These include optical and radar imaging satellites (Sentinel-1, 2, and 3), as well as atmospheric chemistry monitoring missions (Sentinel-5P). The program follows a full, open data policy, which makes high-quality satellite products freely available to researchers, policymakers, and the public (Aschbacher & Milagro-Pérez, 2012).

Fig. 9 Copernicus programme.

The Sentinel-2 mission, launched in two phases in 2015 (Sentinel-2A) and 2017 (Sentinel-2B), is particularly relevant for land surface monitoring, including applications in agriculture, forestry, urban planning, and geology. Although images from Sentinel-2C, launched in September 2024, are now available, this work was based on images from Sentinel 2A and 2B. Sentinel-2B is the twin of Sentinel-2A and

operates in the same Sun-synchronous orbit, phased 180° apart to ensure a revisit time of 5 days at the equator when combined. The satellites are equipped with the MultiSpectral Instrument (MSI), which captures imagery in 13 spectral bands (Fig. 10) from the visible to the shortwave infrared (SWIR) region (Drusch et al., 2012). The bands include:

4 bands at 10 m resolution: Blue (B2), Green (B3), Red (B4), and NIR (B8)

6 bands at 20 m: Red Edge (B5, B6, B7), Narrow NIR (B8A), SWIR (B11, B12)

3 bands at 60 m: for atmospheric correction (B1, B9, B10)

Bands Sentinel-2	Sentinel-2A		Sentinel-2B		
	Central wavelenght (nm)	Bandwidth (nm)	Central wavelenght (nm)	Bandwidth (nm)	Spatial resolution (m)
Band 1 - Coastal aerosol	442.7	21	442.2	21	60
Band 2 - Blue	492.4	66	492.1	66	10
Band 3 - Green	559.8	36	559.0	36	10
Band 4 - Red	664.6	31	664.9	31	10
Band 5 - Vegetation "red edge"	704.1	15	703.8	16	20
Band 6 - Vegetation "red edge"	740.5	15	739.1	15	20
Band 7 - Vegetation "red edge"	782.8	20	779.7	20	20
Band 8 - NIR	832.8	106	832.9	106	10
Band 8A - Narrow NIR	864.7	21	864.0	22	20
Band 9 - Water vapor	945.1	20	943.2	21	60
Band 10 - SWIR - Cirrus	1373.5	31	1376.9	30	60
Band 11 - SWIR	1613.7	91	1610.4	94	20
Band 12 - SWIR	2202.4	175	2185.7	185	20

Fig. 10 Bands table of Sentinel-2 satellite (ESA).

This configuration is optimized for vegetation health monitoring, land cover classification, and surface reflectance analysis, which are essential in geological and environmental applications. Particularly, bands 4, 8, 11, and 12, allowing assessment of lava flow albedo and thermal degradation features over time, are relevant to this thesis. The wide swath (290 km), high radiometric sensitivity, and systematic coverage allow Sentinel-2 to generate time series of spectral reflectance, enabling temporal studies of surface changes, such as those occurring on volcanic terrain after eruptive episodes (Gómez et al., 2016). In this thesis, Sentinel-2 imagery serves as the primary data source for developing and applying spectral indices aimed at estimating the relative ages of lava flows. Its high spectral fidelity, combined with free and open access to data, makes Sentinel-2 an indispensable tool for advancing remote sensing methodologies in volcanology and supporting broader geoscientific research.

2. Methodology

Understanding the temporal evolution of volcanic terrains is essential for both scientific inquiry and hazard mitigation. Lava flows, as surface expressions of volcanic activity, preserve valuable chronological and geochemical information. However, estimating their age across large or inaccessible areas poses significant challenges. While radiometric dating methods offer high accuracy (e.g., McDougall & Swanson, 1972), they are often constrained by high costs, logistical complexity, and spatial limitations. To address these challenges, this study proposes an integrated approach that combines satellite-based remote sensing with Geographic Information Systems (GIS) to estimate the relative age of lava flows over extensive and geologically complex landscapes. The methodology features a structured workflow incorporating custom geospatial tools, spectral analysis techniques, and validation protocols to ensure accuracy and reproducibility. Central to this approach is the use of Sentinel-2 multispectral imagery (Drusch et al., 2012) combined with the use of an original ArcGIS Pro toolbox named “PolyGrid”, appropriately designed to provide automatic extraction of rock outcrops, excluding areas rich in vegetation and moisture. In addition, the method has developed applications to investigate targeted spectral band ratios. Similar remote sensing techniques have been employed in other studies to monitor volcanic features and processes (Pieri & Abrams, 2004; Ramsey & Flynn, 2004), highlighting the potential of multispectral analysis in volcanic terrain assessment. A set of spectral indicators was selected and tested as a complement to the index of iron oxidation states, obtained using the Fe^{3+}/Fe^{2+} ratio. In developing the methodology, this index has represented the primary reference proxy for surface weathering and, by extension, for the relative age of lava flows (Gillespie et al., 1986; Chevrel et al., 2021), to use for comparison and validation of the other indexes.

2.1 PolyGrid Toolbox in ArcGIS Pro

A cornerstone of this methodology is the creation of a custom toolbox named *PolyGrid* within the ArcGIS Pro environment “ModelBuilder”. PolyGrid is specifically designed to preprocess high-resolution satellite images by isolating exposed rock surfaces, which are critical for accurate spectral analysis. The workflow (Fig. 11) starts by importing Sentinel-2 bands 04 (Red) and 08 (Near Infrared, NIR), which are useful for computing the Normalized Difference Vegetation Index (NDVI), in order to identify the signature of the vegetated areas, specifically green vegetation as it reacts to photosynthetic activity of plants, and moisture content, that must be excluded from further analysis. To spatially structure this information, a polygonal grid is generated using the "Create Fishnet" tool. This grid divides the NDVI image into rectangular polygons that match the resolution of the input raster (typically 10-20 or 60 meters for the bands used). At the centre of each polygon, a point is created using the "Feature to Point" tool, representing the centroid of the pixel. These points are then populated with the corresponding NDVI value using the "Extract Multi Values to Points" tool, which transfers raster values to the vector points. Next, these values are spatially joined back to their original polygons, associating each grid cell with a specific NDVI reflectance. This is achieved through the "Field to Polygon" function, linking the NDVI value from each point to its corresponding polygon. The result is a vector-based representation of the NDVI raster, where each polygon now contains the exact NDVI value of the underlying satellite pixel. PolyGrid then applies user-defined thresholds to exclude polygons whose NDVI values indicate the presence of vegetation (typically NDVI > 0.3) or high surface moisture (typically NDVI < 0). The remaining polygons, representing bare rock outcrops, are retained for subsequent analysis. This cleaned polygon layer is then used as a spatial mask to clip and constrain the analysis of spectral band ratios. By filtering out non-geological features (vegetation, clouds, water and shadows) at this early stage, PolyGrid ensures that all subsequent analyses are focused solely on exposed volcanic rocks, improving the reliability and consistency of the subsequent spectral-based age estimations. This step is essential to prevent

contamination of the spectral data by non-geological features. The resulting polygon grid represents a refined and clean dataset of exposed volcanic rock outcrops. Crucially, this polygonal mask is subsequently used to clip and spatially constrain the band ratio images, ensuring that subsequent spectral analyses focus solely on relevant surfaces, maintaining consistency and precision across different processing stages.

For clarity, several images (Fig. 12, Fig. 13 and Fig. 14)are presented to illustrate the difference between the non-processed imagery and the same scenes after clipping with the mask generated by the PolyGrid toolbox. In all four study areas, the application of the toolbox effectively removed most of the background ‘noise,’ yielding cleaner and more interpretable images.

Fig. 11 Polygrid flow chart.

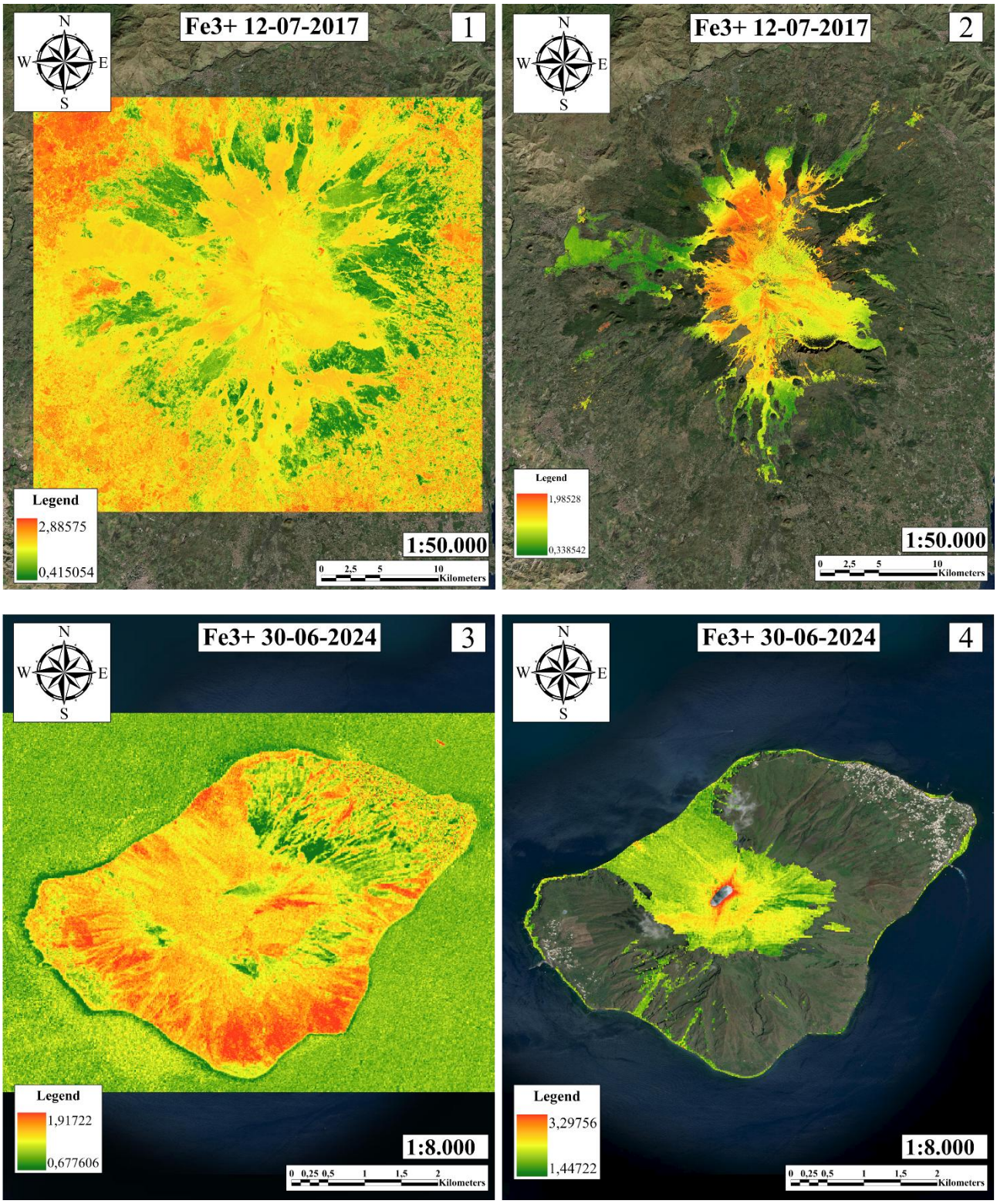

Fig. 12 Comparison between non-processing images (1-3) and the Polygrid processed ones (2-4), Etna and Stromboli volcanoes.

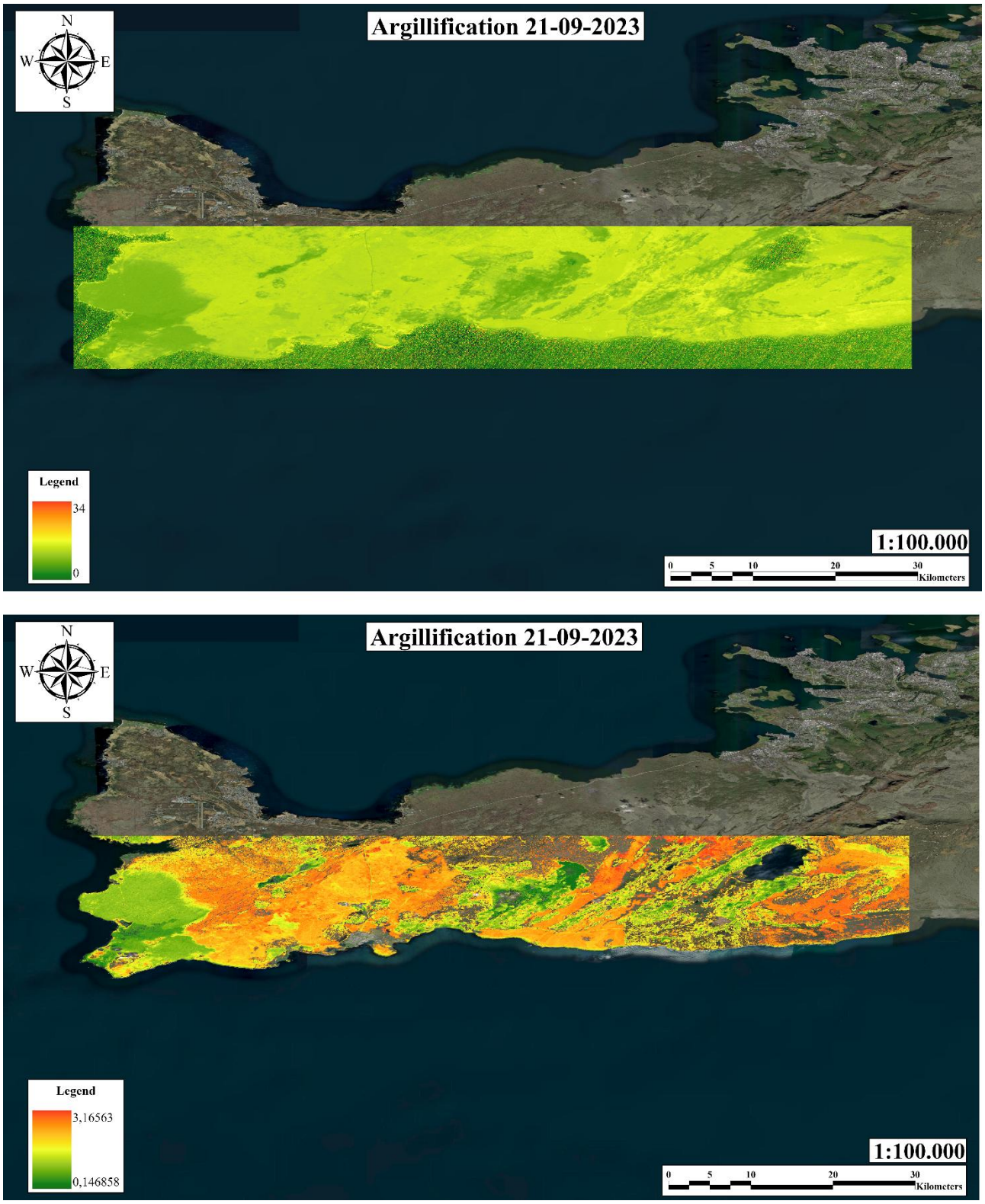

Fig. 13 Comparison between non-processing image and the Polygrid processed ones, Reykjanes Peninsula.

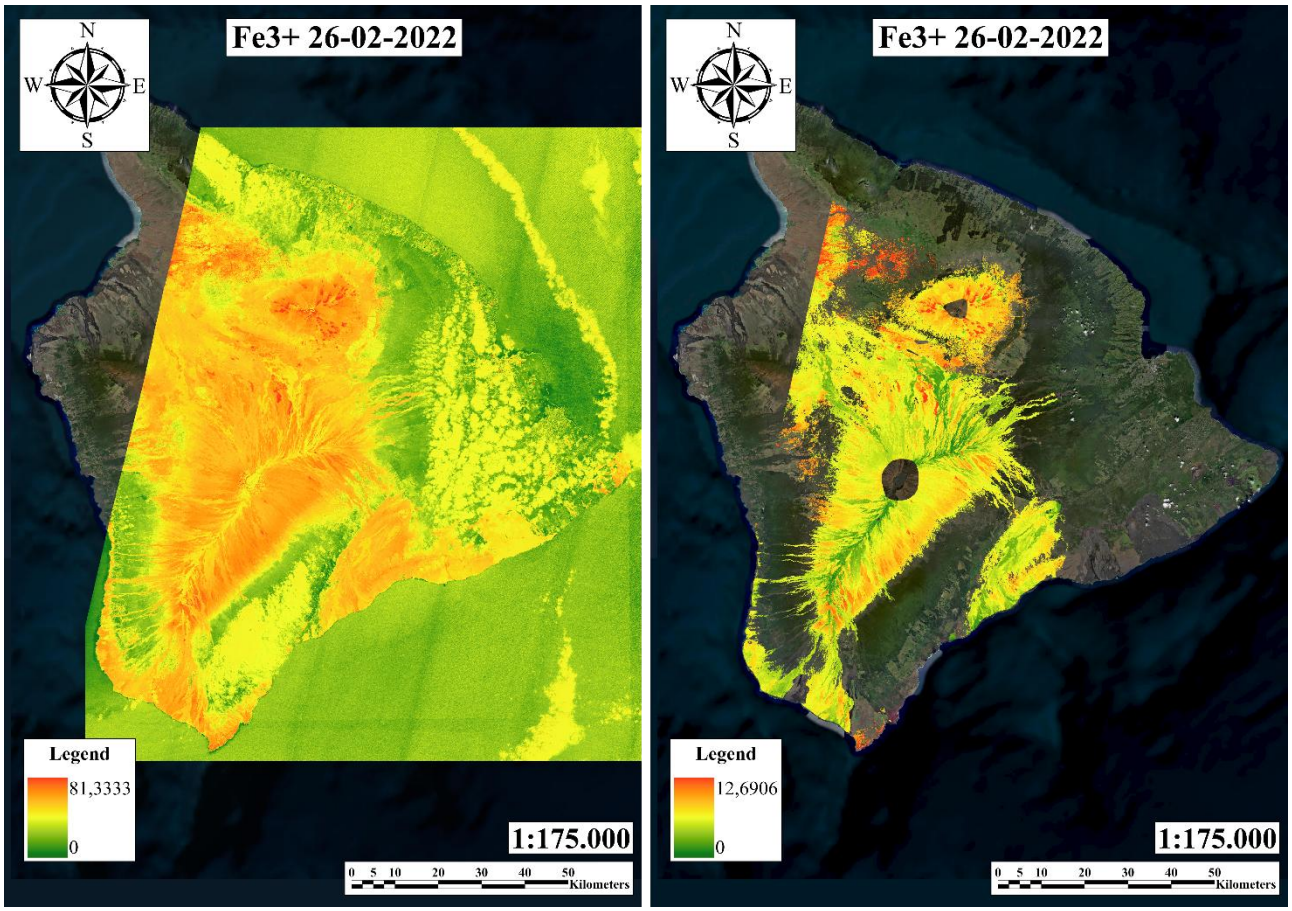

Fig. 14 Comparison between non-processing image and the Polygrid processed ones at Hawai'i Island.

2.2 Spectral Indicators

The first test to select spectral indicators was performed, focusing on the Mount Etna Volcano region. It was based on Sentinel-2 imagery from four distinct acquisition dates: 12 July 2017, 16 July 2023, 15 July 2024, and 13 October 2024. These dates were selected to provide temporal diversity and capture seasonal variability, ensuring robustness in the spectral response of altered volcanic surfaces. Each scene was pre-processed and normalized to reduce the influence of environmental factors such as humidity and atmospheric conditions (Drusch et al., 2012; Kervyn et al., 2010). As a targeted case study, the Etna volcano was selected for the application and evaluation of additional spectral indexes aimed at refining the assessment of lava flow ageing. In this phase of the research, multiple band ratios beyond the Fe^{3+}/Fe^{2+} indicator were explored to test their effectiveness in distinguishing lava flows of different ages. These indexes were selected on the base of their sensitivity to specific mineralogical and geochemical changes associated with post-eruptive surface alteration (Chevrel et al., 2021; Gillespie et al., 1986). Each band ratio analysed in this study was initially derived from the USGS spectral library. The spectral signatures of target minerals served as a basis for selecting and testing various combinations, from which the most effective indices were ultimately chosen.

Referring to the bands table of Fig. 10, the selected and analysed spectral indices include the following targets:

- Argillification: B11 / B12
- Iron oxide concentration: B11 / B08
- Sulphur content detection: B05 / B01
- Silica-rich content: B12 / B02
- Pyroxene alteration: B11 / B02
- Iron-bearing minerals: (B06 + B07) / B8A

- Coarse-grained iron features: (B03 + B11) / (B04 / B08)

Each of these indices was computed as a separate raster and clipped using the PolyGrid-generated rock outcrop mask. This ensured consistency in spatial analysis and limited the influence of vegetation and soil moisture on the spectral signal (Pieri & Abrams, 2004; Ramsey & Flynn, 2004). The resulting layers were visually inspected and statistically evaluated to determine their correlation with lava flow ages reported in the 1:50.000 scale Geological map of Mount Etna (Branca et al., 2011). This map provided a reliable reference dataset, with lava flows categorized by their relative and absolute ages, deriving from the most updated chronostratigraphy of the volcano (De Beni et al., 2011). The goal was to identify which, among all the considered indexes, showed the most consistent and interpretable trends in relation to the aging of the lava surface. Preliminary findings indicated that certain indices, particularly the B11/B08 (iron oxides) and (B06+B07)/B8A (iron-bearing minerals), showed promising results in delineating flows of different oxidation states and relative weathering degrees. Other indices such as B11/B02 (pyroxene alteration) and B12/B02 (silica-rich content) offered complementary information on silicate and pyroxene transformation with age. Although these two variables showed age-dependent behaviour, the relationship was weaker and did not follow a clear linear pattern. This multivariate spectral approach allowed for a broader understanding of the mineralogical evolution of lava flows and provided additional tools for relative dating in complex volcanic environments like Etna. The findings from this case study informed the selection of spectral features for more generalized applications and helped refine the overall methodology.

2.3 Band Ratios for Iron Detection

The next step of the adopted methodology involves the design of two specific band ratios to detect and quantify the presence of ferrous (Fe^{2+}) and ferric (Fe^{3+}) iron ions. These ratios were derived from a thorough review of the spectral characteristics of iron-bearing minerals, with a particular focus on reflectance patterns in the near-infrared (NIR) and shortwave infrared (SWIR) regions (Gillespie et al., 1986; Kervyn et al., 2010). The Fe^{2+} band ratio is calibrated to enhance the spectral response of reduced iron, typically found in fresher, less weathered lava flows. Conversely, the Fe^{3+} band ratio is designed to emphasize the oxidized iron content, which increases with prolonged exposure of rocks to the atmospheric conditions (Chevrel et al., 2021; Ramsey & Flynn, 2004). The Fe^{2+} ratio was calculated using Sentinel-2 bands B12 (SWIR 2), B08 (NIR), B04 (Red), and B03 (Green)(Fig. 10), which correspond to wavelengths sensitive to the absorption features of ferrous iron. Fresher lava flows typically contain higher proportions of Fe^{2+}, characterized by distinct spectral responses in these bands (Drusch et al., 2012). In contrast, the Fe^{3+} ratio was constructed using bands B04 (Red) and B02 (Blue)(Fig. 10), capturing the reflectance peak associated with oxidized iron-bearing minerals. Both ratios were derived empirically based on literature studies and calibrated against known reference spectra from the USGS spectral library where in situ measurements were available (Pieri & Abrams, 2004; Gillespie et al., 1986). The logic behind the use of these ratios lies in their differential sensitivity to mineralogical transformations that occur during post-eruptive surface alteration. By emphasizing these chemical transitions, the ratios provide a consistent and transferable metric for comparing lava flow ages across diverse geological contexts. The Fe^{3+} and Fe^{2+} ratio images are individually processed and subsequently combined into a single composite image representing the Fe^{3+}/Fe^{2+} ratio. This index is calculated on a pixel-by-pixel basis across the clipped extent defined by the PolyGrid mask. The resulting ratio image (Fig. 15) is interpreted as a proxy for the oxidative state of the lava surface, with higher values indicating older, more weathered flows, and lower values corresponding to fresher, less altered material.

The resulting product is a detailed spatial representation of oxidation gradients, providing insight into the relative ageing of volcanic surfaces. The Fe^{3+}/Fe^{2+} ratio image thus becomes a central product of the analysis, offering both qualitative insight into spatial ageing trends and quantitative metrics for subsequent statistical validation.

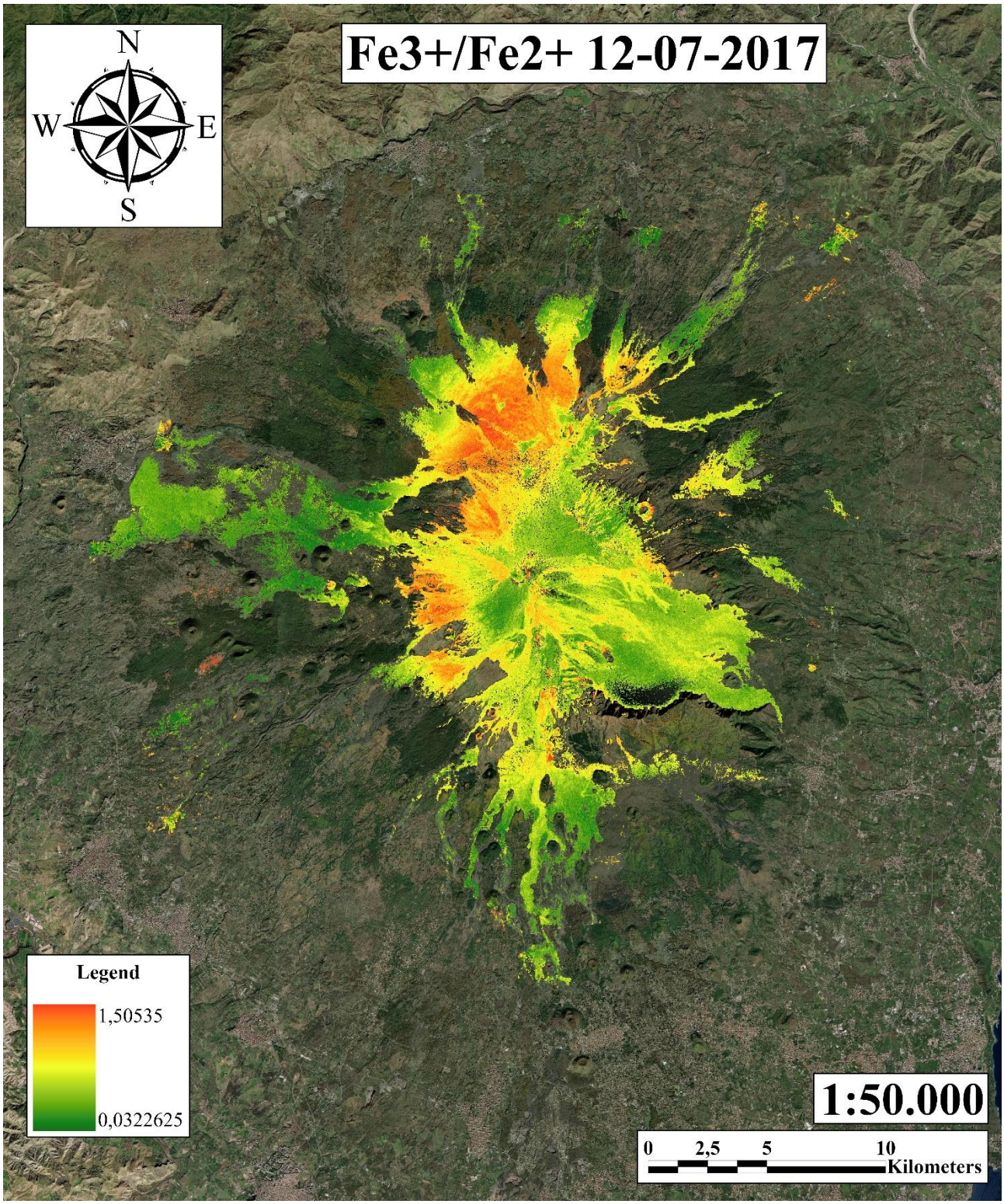

Fig. 15 Example of resulting ratio Fe2+/Fe3+ image at Mount Etna.

2.4 Moisture-Based Normalization

Given the influence of surface moisture on spectral reflectance particularly in the shortwave infrared (SWIR) region an additional step was introduced to normalize the spectral data based on moisture conditions. This correction was necessary to reduce the impact of residual surface moisture on the spectral signatures of outcropping rocks, as their reflectance values are generally reduced by ground humidity. The normalization process involved the creation of a moisture index by calculating the moisture index with two bands from Sentinel-2: B11 (SWIR) and B8A (NIR narrow)(Fig. 10). These bands are sensitive to water content in the soil and rock surface and provide a first-order approximation of surface moisture variability. A moisture raster, representing the relative degree of humidity across the scene, was thus generated. This moisture raster was then used to normalize the spectral signature in the band ratio images. Each ratio raster was summed by the corresponding moisture layer on a pixel-by-pixel basis, yielding moisture-normalized rasters. These corrected rasters were subsequently used to recompute the final images. This normalization step helps minimize the confounding effects of water absorption on the spectral signature detection, particularly in areas where recent precipitation or soil saturation might otherwise bias the spectral signal. The incorporation of this moisture-based correction enhances the consistency and reliability of the spectral analysis across different volcanic environments and acquisition dates. It also improves the comparability between images acquired under varying atmospheric and seasonal conditions, increasing the robustness of the method for large-scale or multi-temporal studies.

For clarity, several images (Fig. 16, Fig. 17 and Fig. 18)are presented to illustrate the differences before and after the moisture normalization process. In the case of Kīlauea, infrared values were used for normalization instead of moisture indices. The comparison clearly highlights the importance of the normalization step, as the final results appear significantly clearer and more reliable.

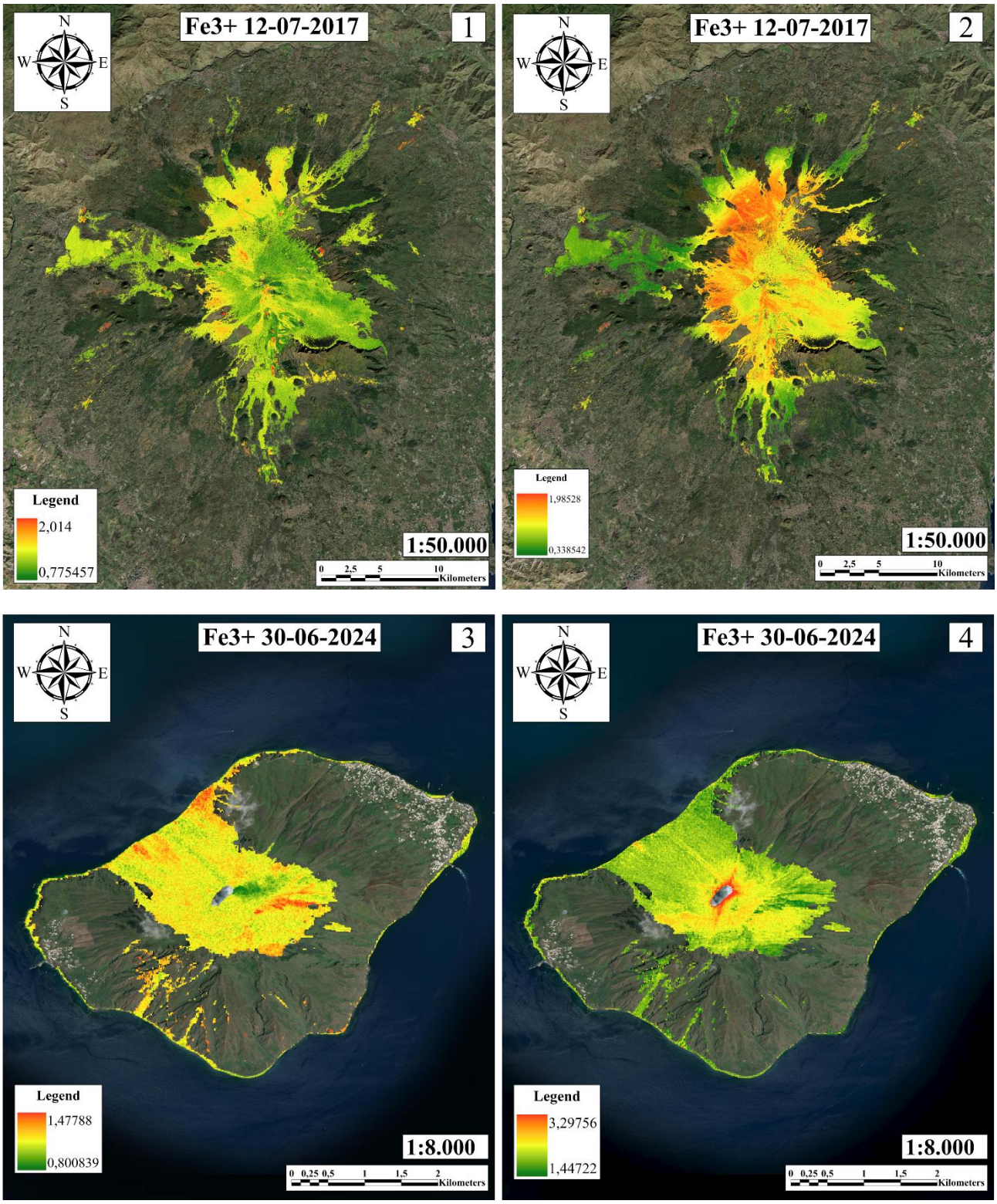

Fig. 16 Effect of moisture normalization: images prior to correction (1-3) and after correction (2-4).

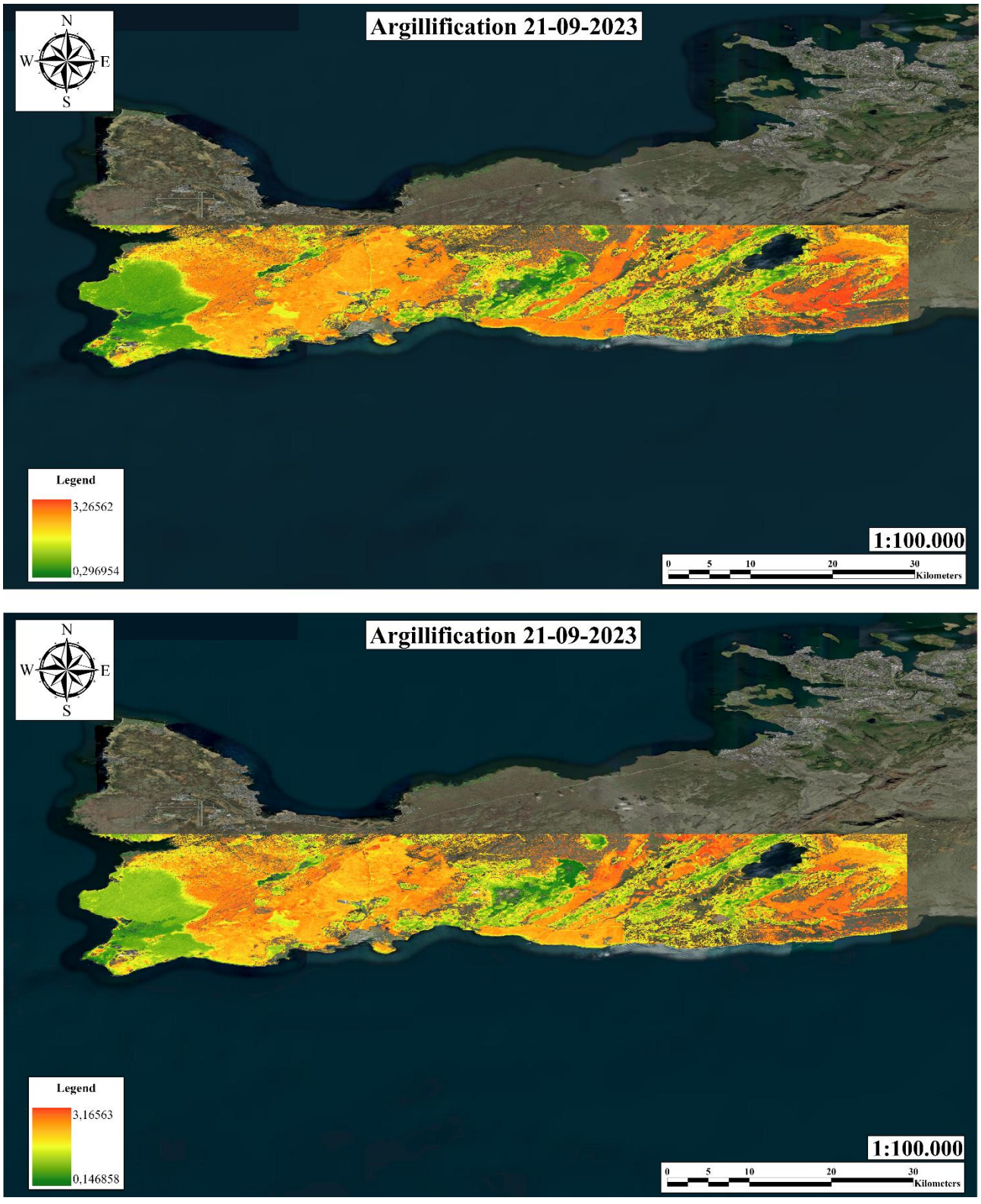

Fig. 17 Effect of moisture normalization: image prior to correction (Top) and after correction (Bottom).

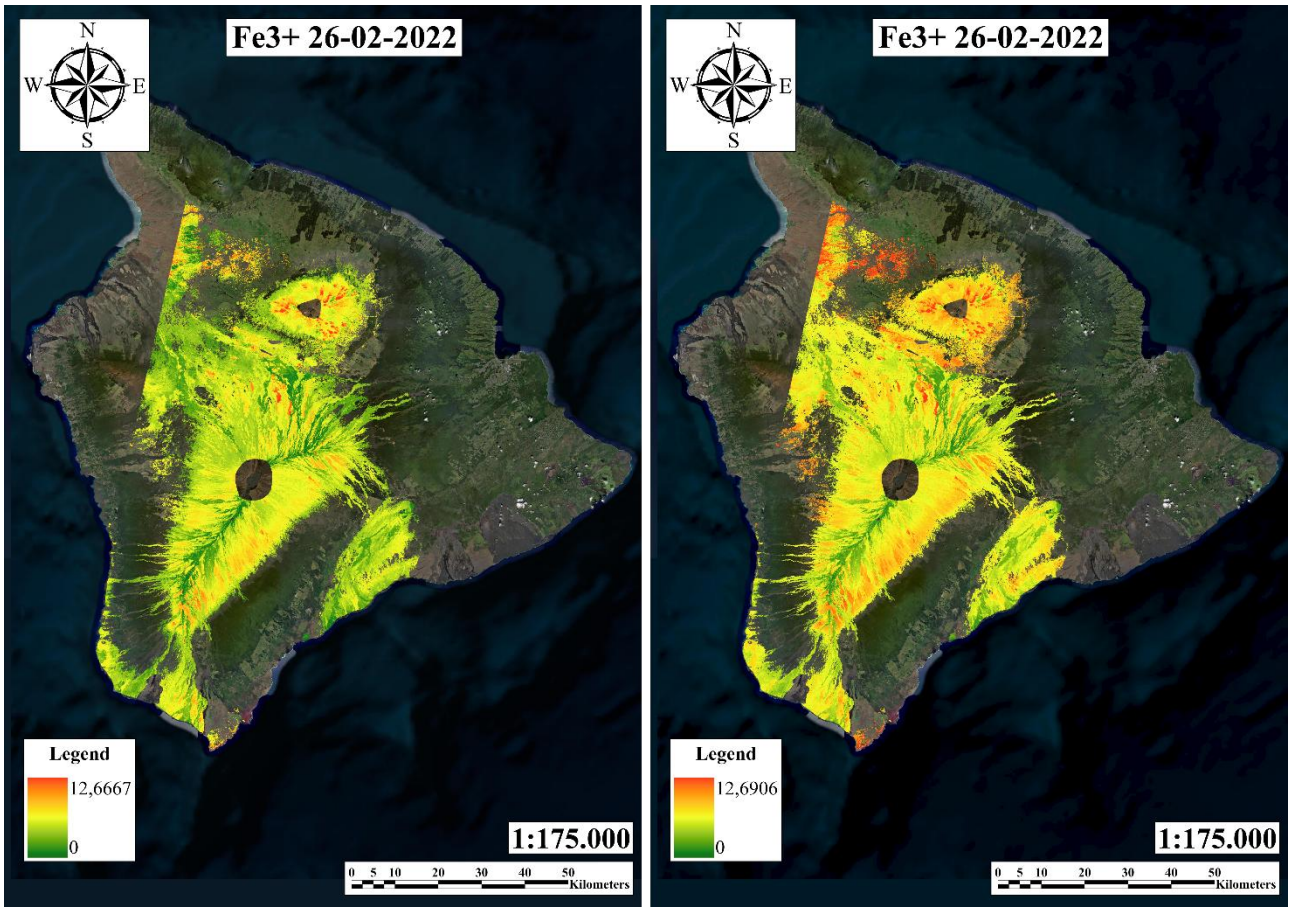

Fig. 18 Effect of IR normalization: image prior to correction (Left) and after correction (Right).

2.5 Comparison with Chronological Data

The accuracy and reliability of the proposed method were evaluated through a comprehensive validation process that integrated both spatial and numerical assessments. Specifically, the reflectance-derived band ratio maps were compared against independently dated lava flows, using reference datasets provided by authoritative geological institutions, including the National Institute of Geophysics and Volcanology (INGV) of Italy, the Italian Institute for Environmental Protection and Research and the United States Geological Survey (USGS). These institutions have produced high-resolution geological maps and chronologies of lava fields based on detailed stratigraphic studies, radiometric dating, and field observations, offering a robust benchmark for remote sensing-based comparisons. Spatial validation was conducted by overlying the reflectance-based ratio images onto geological vector layers of lava flow boundaries. This comparison enabled a direct visual assessment of whether spectral variations in the band ratio images aligned with contours of known flow units, structural discontinuities, or contacts between products from different eruptive periods. These validation steps demonstrate that the spectral indices particularly the Fe^{3+}/Fe^{2+} ratio not only correlate with chronological information but also reproduce the spatial geometry of volcanic surfaces with geologically meaningful accuracy. This strengthens the interpretability of the results and suggests that the method is transferable across different volcanic environments with minimal recalibration, supporting its broader applicability in planetary and terrestrial lava flow studies.

3 Data discussion

3.1 Etna

Etna volcano was selected for the first application and evaluation of spectral indices aimed at experimenting the assessment of lava flow ageing for the constantly updated geological map. In this phase of the research, multiple band ratios were explored to test their effectiveness in distinguishing lava flows of different ages. These indices were selected based on their sensitivity to specific mineralogical and geochemical changes associated with post-eruptive surface alteration.

The spectral indices analysed include:

- **NDVI: (B08-B04)/(B08+B04)**

  A Normalised Difference Vegetation Index was employed as a proxy to effectively mask pixels dominated by vegetation/moisture cover, ensuring that the PolyGrid toolbox operated exclusively on bare rock surfaces for more accurate spectral analysis.

- **Argillification: B11 / B12**

  This band was chosen as a proxy to desume the age of lava flow emplacement from the degree of alteration of the lava flow. As basaltic minerals through weathering turn into clay minerals, the degree of argillification could be directly connected to the duration of the exposure of basalts to the atmospheric conditions.

- **Iron oxide concentration: B11 / B08**

  This band was chosen as a proxy to desume the age of lava flow emplacement from the degree of oxidation of Fe-bearing basaltic minerals. This increases with the time-duration of the exposure of lavas at surface

- **Sulphur content detection: B05 / B01**

  This band was chosen as an indirect measure of age of lava flows by assessing the deposition time of the sulphur, formed by the fumaroles or the hydrothermal process, on them.

- **Silica-rich content: B12 / B02**

This band was chosen as proxy to measure the time-duration of weathering of lavas, by assessing the degree of silica-enrichment, which increases over the time, due to the differential sensitivity of basaltic minerals to the alteration.

- **Pyroxenes alteration: B11 / B02**

  This band was chosen to measure the degree of alteration of the lavas, considering the minerals more sensitive to the chemical weathering. This band, suitable to detect the earlier stages of alteration, has been tested for age-discrimination among recent lavas.

- **Coarse-grained iron features: (B03 + B11) / (B04 / B08)**

  This band was chosen to detect the quantity of coarse-grained iron features, as a measure of timing of the iron oxide crystals grow, increasing over the time. The higher reflectance values indicate longer time-duration of the process.

- **Bivalent iron: (B12/B08)+(B03/B04)**

  This band was chosen as the iron, in the Fe-bearing basalt minerals, naturally turn from bivalent to trivalent, with the increase (time-duration) of the alteration processes. High reflectance values thus indicate low time-duration of alteration.

- **Trivalent iron: B04/B02**
- This band was chosen as a complement of the previous. In this case, high reflectance values thus indicate long time-duration of alteration, favouring the Fe^{3+} enrichment.

Each of these indices was computed as a separate raster and clipped using the PolyGrid-generated rock outcrop mask. This ensured consistency in spatial analysis and limited the influence of vegetation and moisture on the spectral signal. The resulting layers were visually inspected and statistically evaluated to determine their correlation with lava flow ages reported in the 1:50.000 scale Geological map of Mount Etna (Branca et al., 2011)(Fig. 19). This map provided a categorization of lavas based on absolute and relative ages, deriving from application of the most updated chronostratigraphic scheme of the volcano (De Beni et al., 2011). This map provided a reliable reference dataset, with lava flows categorized by their absolute and relative ages (Fig. 20). The comparison between the spatialized spectral indices and the geological map aims to identify any correlation between them in order to select the indices that best record the

variability in the age of the lava surface To ensure the reliability of the method, for each index, four distinct satellite images, referring to the 12/07/2017, 16/07/2023, 15/07/2024 and 13/10/2024 were analysed. These images have been numbered in the order in the following figures illustrating the distribution of the different considered indexes.

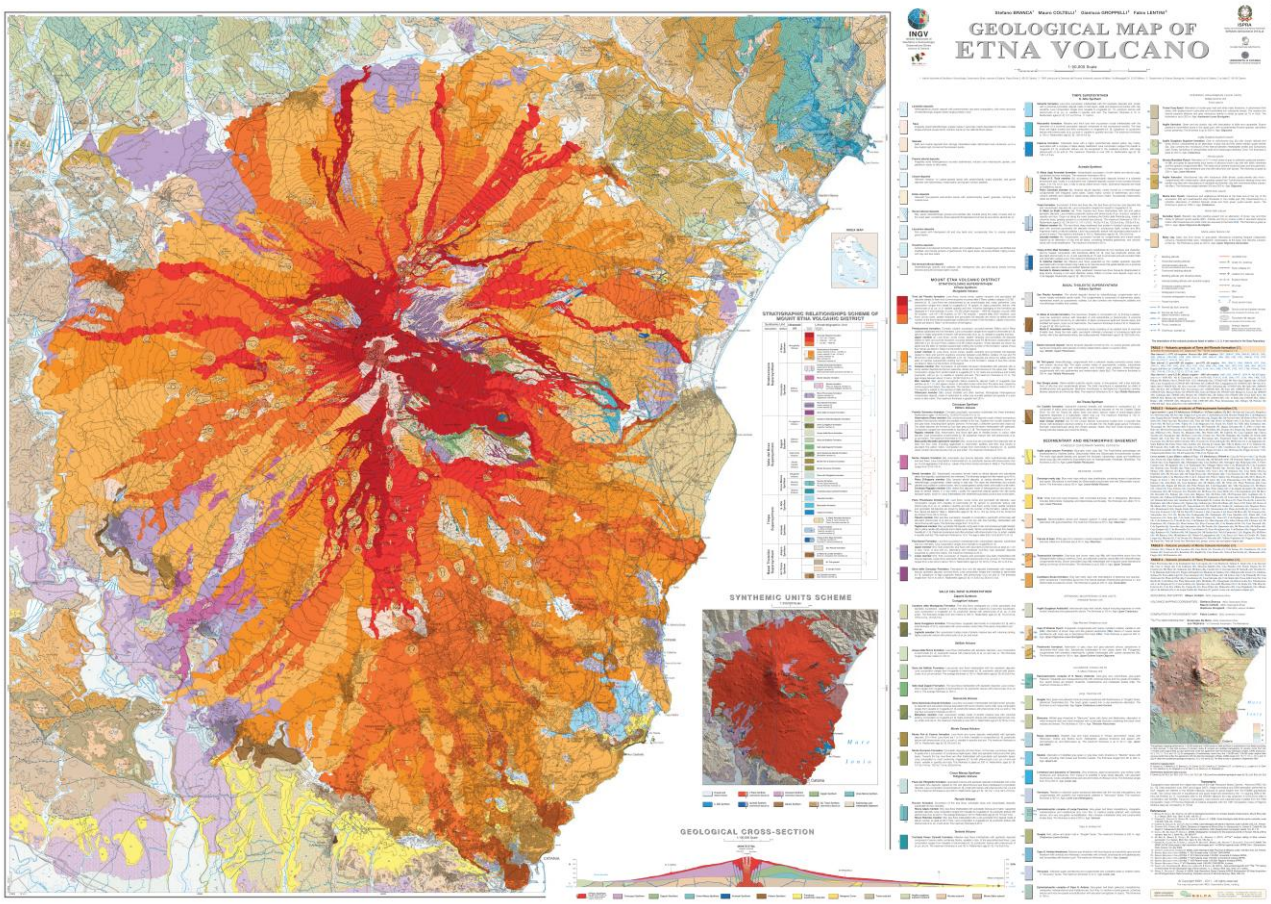

Fig. 19 Geological map of Mount Etna (Branca et al., 2011)

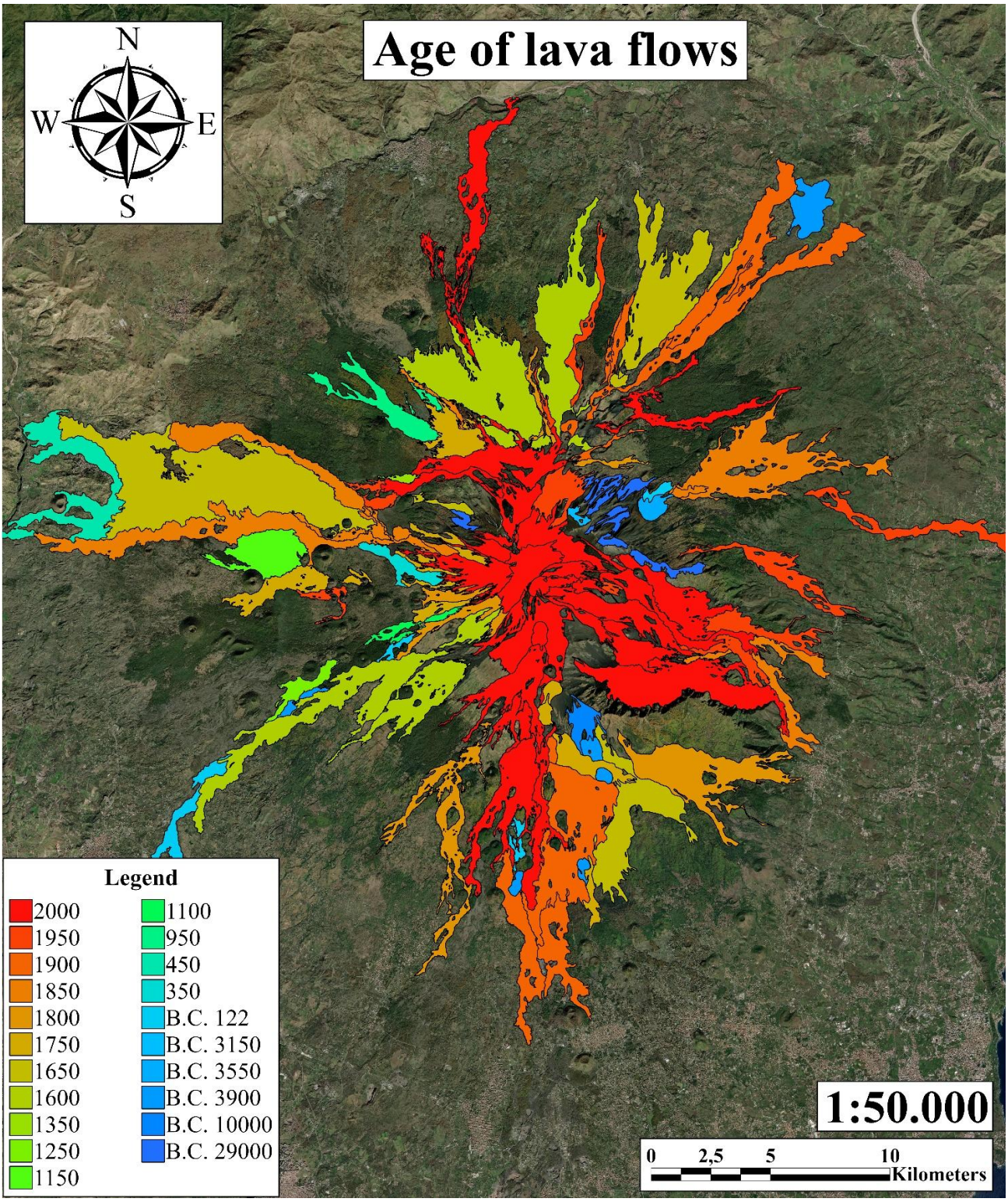

Fig. 20 Dated lava flows with their absolute age, extrapolated from the Geological Map of Mount Etna (Branca et al., 2011). In the map are exclusively reported the exposed outcrops of the lava fields, referring to the Polygrid clean dataset.

1. The **Argillification** index (Fig. 21) showed initially good correlation with lava ages results, as result of the progressive increase of the alteration of the lava flows, producing clay minerals. However, more accurate analyses evidenced a systematic bias in this correlation that is clearly governed by the local topographic gradient. The degree of argillification tends to be higher in flat areas than on steeper slopes, regardless of the age of the outcropping lava. This distortion probably reflects local remobilizations of the clay minerals, due to the erosion of the altered clay horizon from the steepest slopes and the successive accumulation of the transported clays on the adjacent flat areas. Another bias could derive from the presence of vegetation like mosses and lichens, both difficult to spot by using the NDVI (Normalized Difference Vegetation Index). Their presence in the areas where the altered clays formed or deposited may locally change the spectral signature, causing artifacts in the final band ratio raster that can be misinterpreted. The time series of images taken in four different dates analysis confirm that this band ratio is easily influenced by the weathering process and the health of the vegetation, with maximum value of reflectance during winter times, characterised by more healthy mosses and lichens. It is also noticeable that the moisture absorbed by the clay may influence the reflectance values in the final raster.

In conclusion, the Argillification index is a very good for a preliminary analysis, aiming at contouring the different lava flows but it is not reliable to determine their relative age, since it is easily influenced by many factors that heavily impact on the very variable final results so do not provide a constant result.

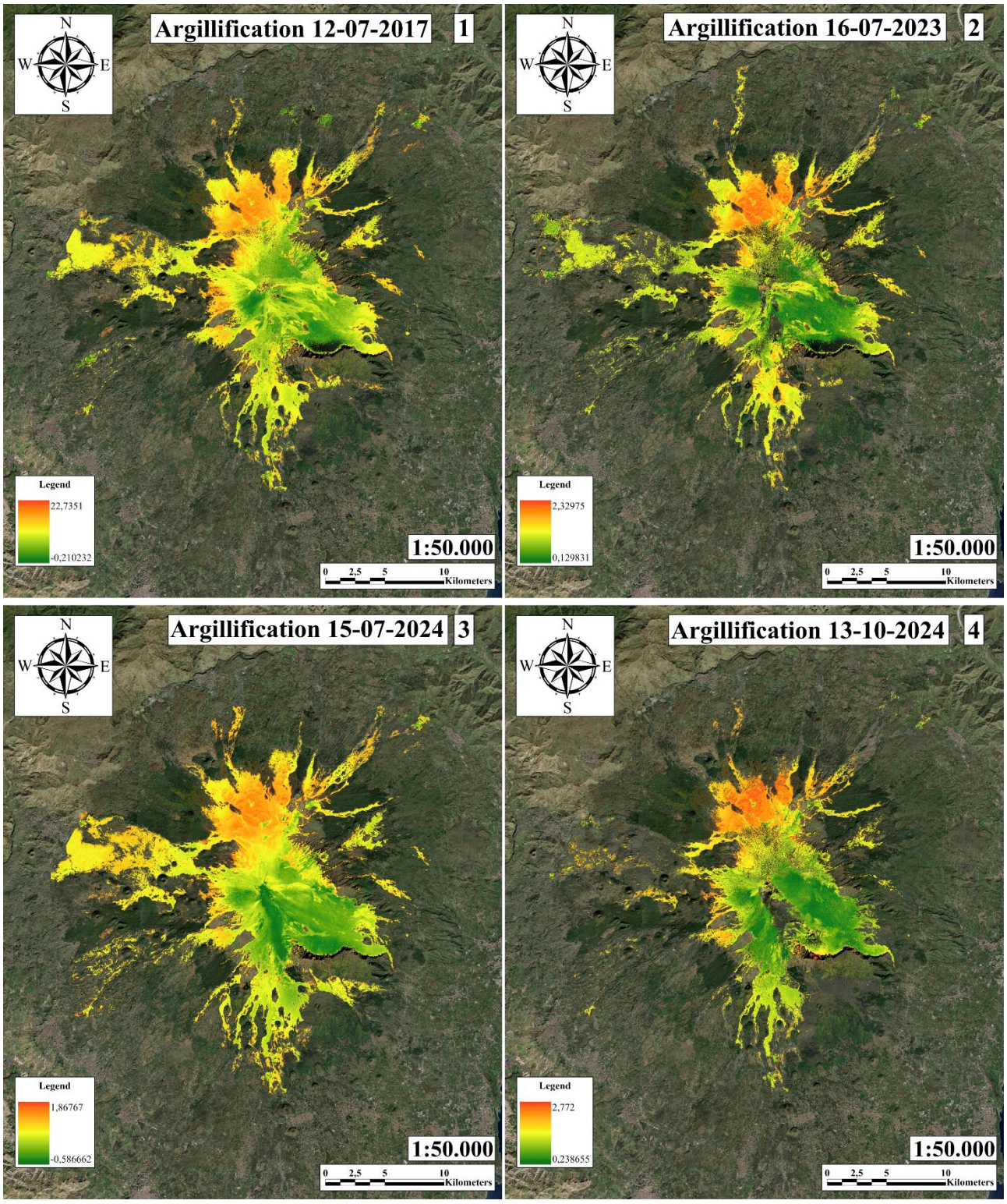

Fig. 21 Argillification index spectral signature images at the Mt. Etna volcano.

2. The **Iron oxide** index (Fig. 23) was developed to verify a correlation between time and the content of iron oxide created by alteration of the iron-rich minerals. Comparing the four different dates images pixel by pixel, the reflectance values approximately remain constant. As for the previous index, evident differences in the images refer to bias due to the presence of moisture or lichens and mosses. A prominent artifact is the annular distribution of different reflectance values, higher at lower altitude, this behaviour is likely due to the mosses and lichens which are denser at the base of the volcano than above a certain altitude, where are sparser because of the colder weather and the snow in winter times. This is also confirmed by examining the NDVI normalised images (Fig. 22) where this change is well shown instead of the moisture normalised images where there is no difference at all.

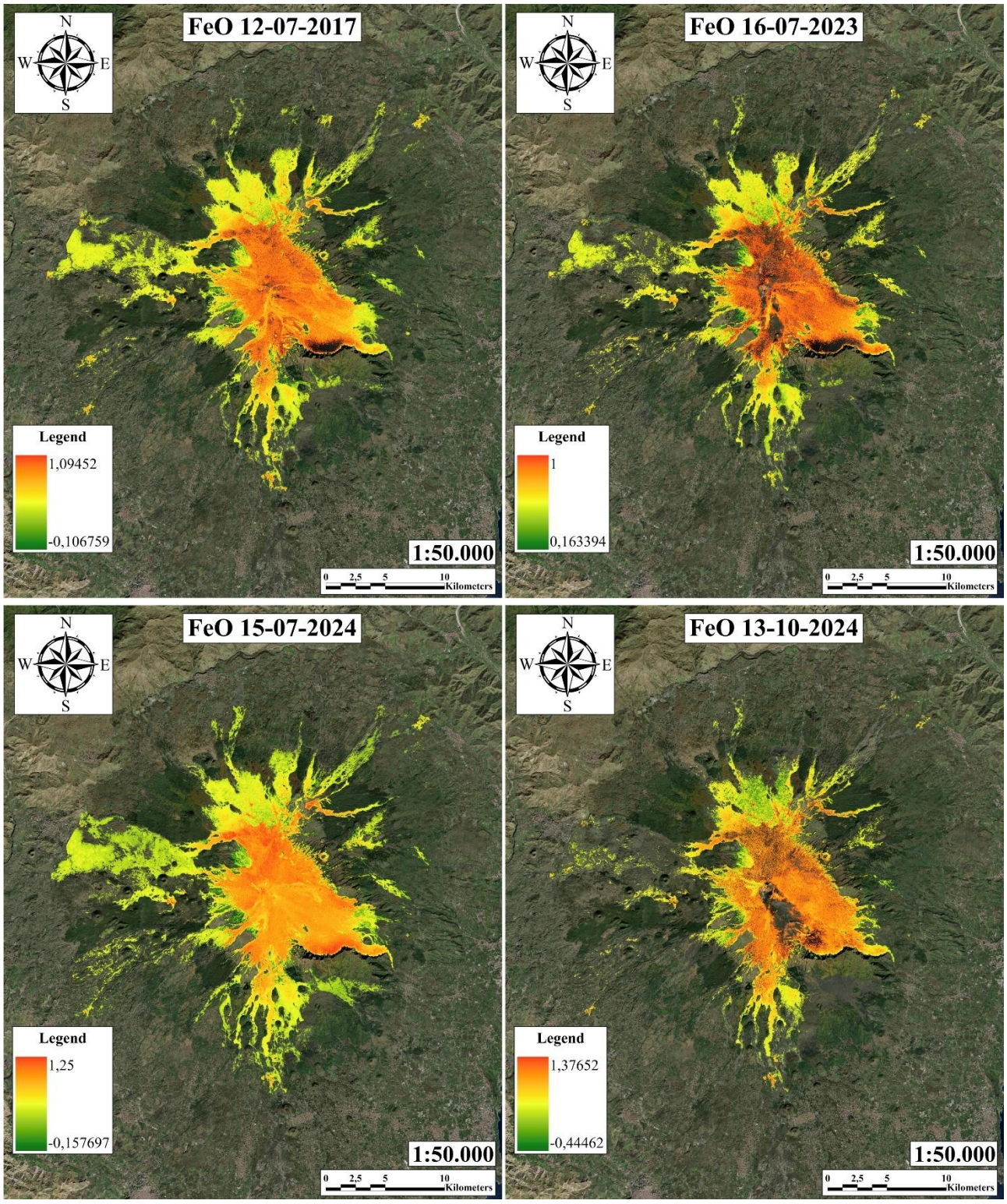

Fig. 22 Iron oxide index spectral signature images, NDVI normalized at the Mt. Etna volcano

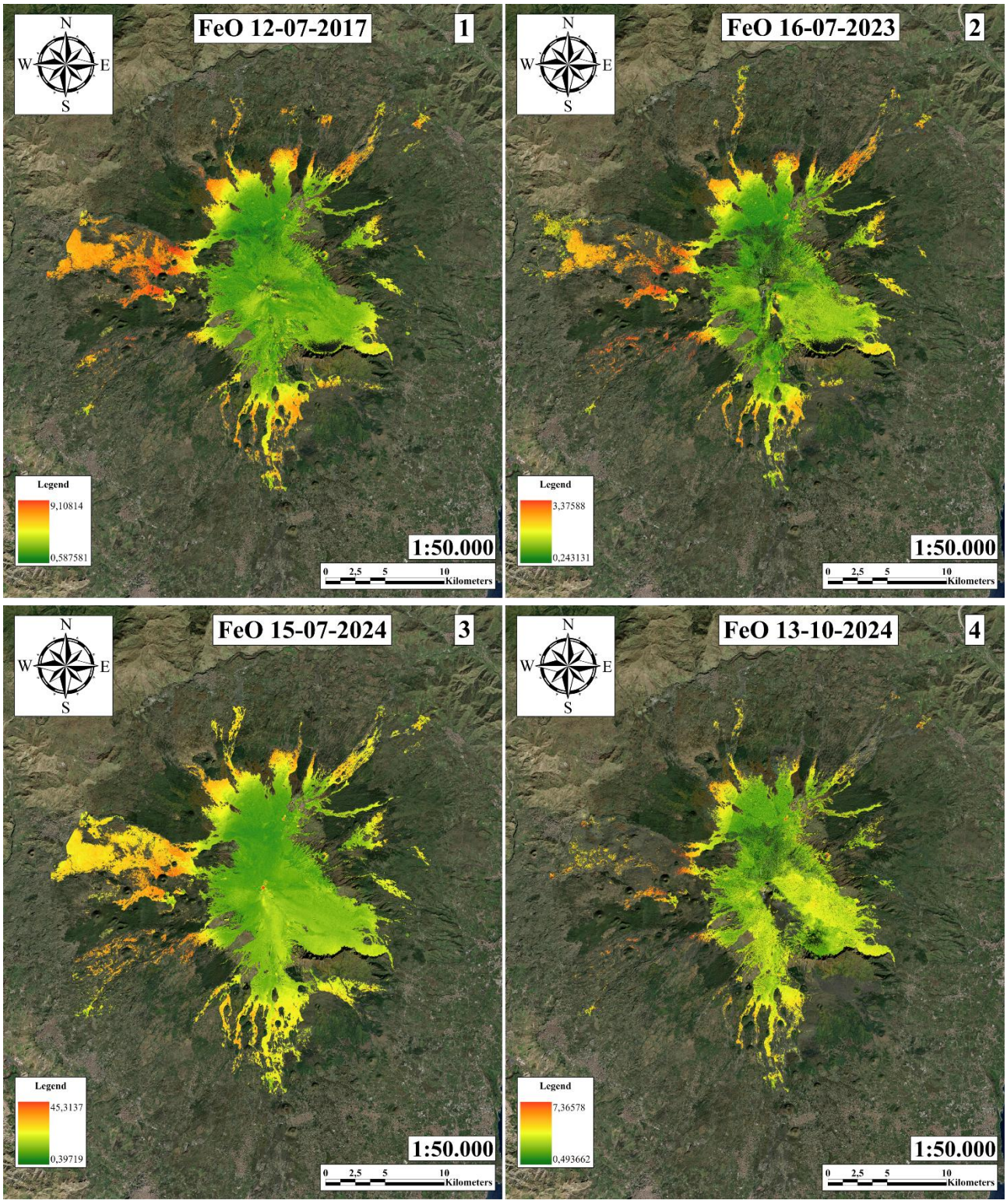

Fig. 23 Iron oxide index spectral signature images at the Mt. Etna volcano.

3. The **Sulphur content detection** index (Fig. 24) was designed to analyse the fumaroles activity since Mount Etna emit a lot of fluid including sulphur ones mainly near the craters where the hydrothermal activity can generate sulphuric deposits. The images show clearly a high reflectance values near the crater with known hydrothermal activity. The areas with high reflectance values are not constant in the time series since they correlate with the intensity of the volcanic activity and gas emission, the higher the volcanic activity the largest are the areas of high values. The Fig. 24-3, for instance, refers to a period of low volcanic activity, with very low reflectance value on the entire top of the edifice. On the contrary, the Fig. 24-1 image show larger areas with high reflectance values, which recorded a period of high volcanic activity. During period of intense active gas emission, the images can record also the effects of the volcanic plume, containing sulphuric acid that is detectable from this index but is invisible in the true colours images, this may cause many artifacts in the reflectance values. In addition, the sulphur is soluble in water. This implies that heavy rain or snow melting can dissolve most of the existing sulphur deposits, this means that even different season can change the result of this index analysis. This is evident in the time series where there are no images that have the high reflectance values in the same place. Considering its dependence on volcanic activity and seasonal variations, this index could be very effective in detecting and recording time series of discrete periods of intense gas emissions.

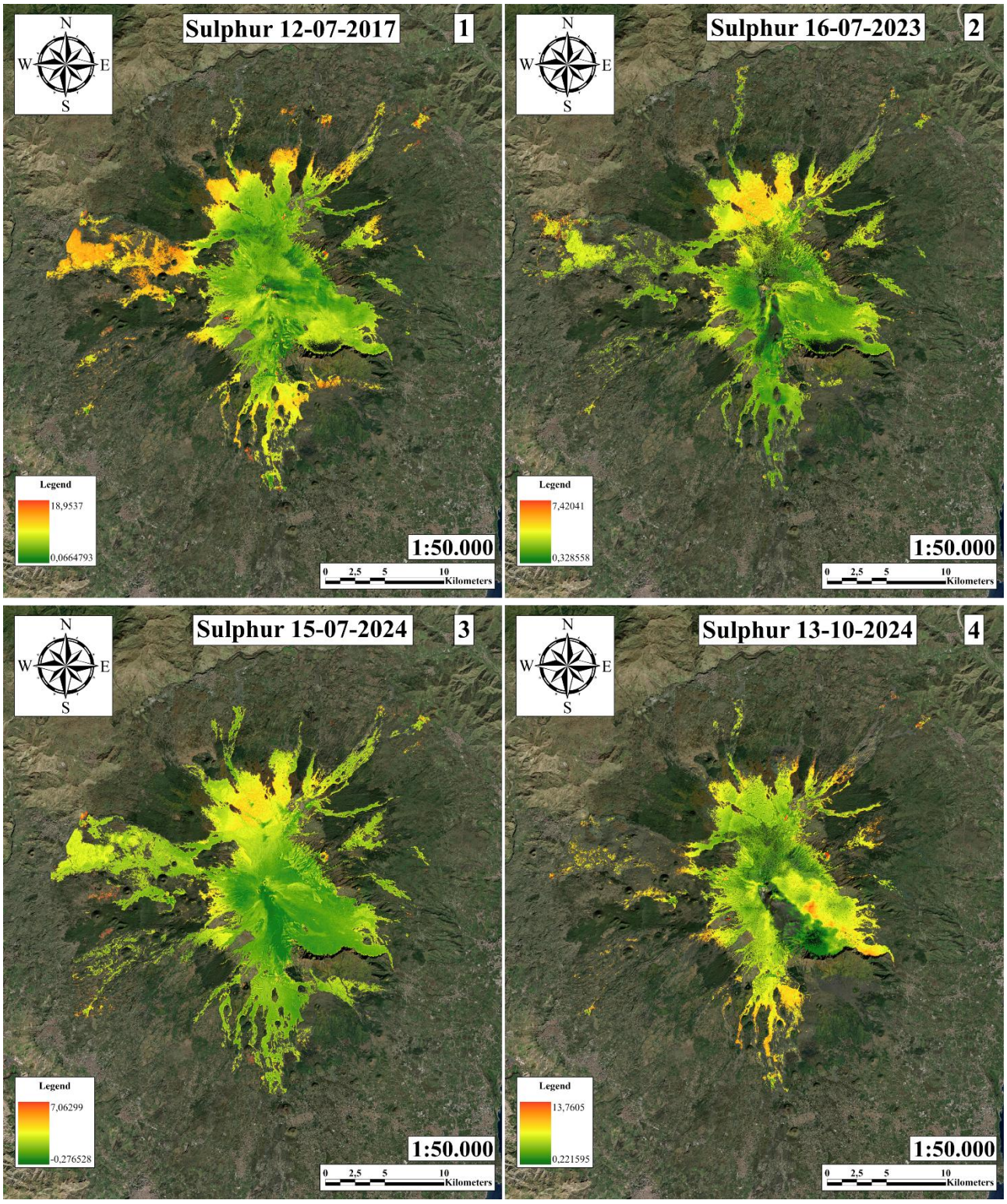

Fig. 24 Sulphur content index spectral signature images at the Mt. Etna volcano.

4. The **Silica-rich content** index (Fig. 25) was devised starting from the Bowen series, predicting the quartz as the last mineral to crystallize from cooling magma and to be weathered. The possible connection with lava ageing is that oldest lava flows should have a higher rate of silica than the younger ones. So higher values in this index means older lava flows. Unfortunately, this index exhibits unreliable behaviour, since the time series show very different results. The same areas have different reflectance values in the four images. Probably the results are buffered from vegetation or moisture, moreover this index is highly sensitive to the presence of plumes emitted from the central craters that is very clear in the Fig. 25-2 and 4 images where the contrast of the lower reflectance values of the plume with the higher values of the rocks is very evident. Analysing the time series is obvious that this index is not sensible at the lava flows age since not one edge is highlighted in the images. These results justify the exclusion of this index from the remaining analytical workflow.

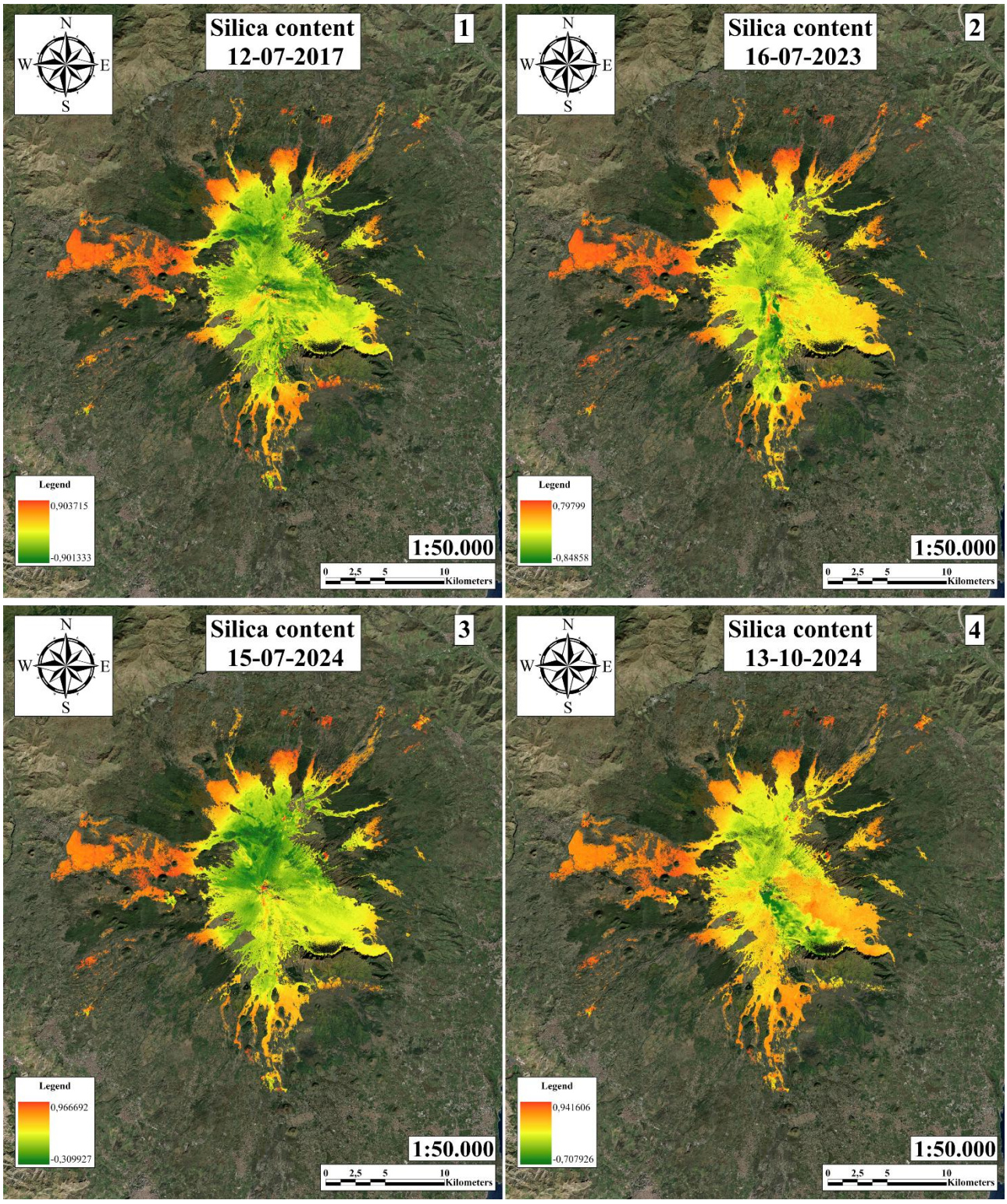

Fig. 25 Silica-rich content index spectral signature images at the Mt. Etna volcano.

5. The **Pyroxenes alteration** index (Fig. 26) was conceived, based on the Bowen series, to use minerals sensitive to weathering processes, to record the earlier stages of mineral alteration. Higher values of Pyroxene alteration would characterize older lava flows, while lower values should be typical of younger lava flows. In the analysed time series, each area shows different reflectance values from an image to the other, never matching the contours of mapped lava units. The Fig. 26-1 image it is the only one that presents some resemble of lava flows edge but if compared with the geological map only a few are similar to the real ones. Furthermore, this index is too sensible to distortions due to the Mount Etna plume. Tentative cleaning of most of these effects did not result in better images. The overall above-mentioned bias affecting the time series of the analysed images suggested to exclude this index from further analysis.

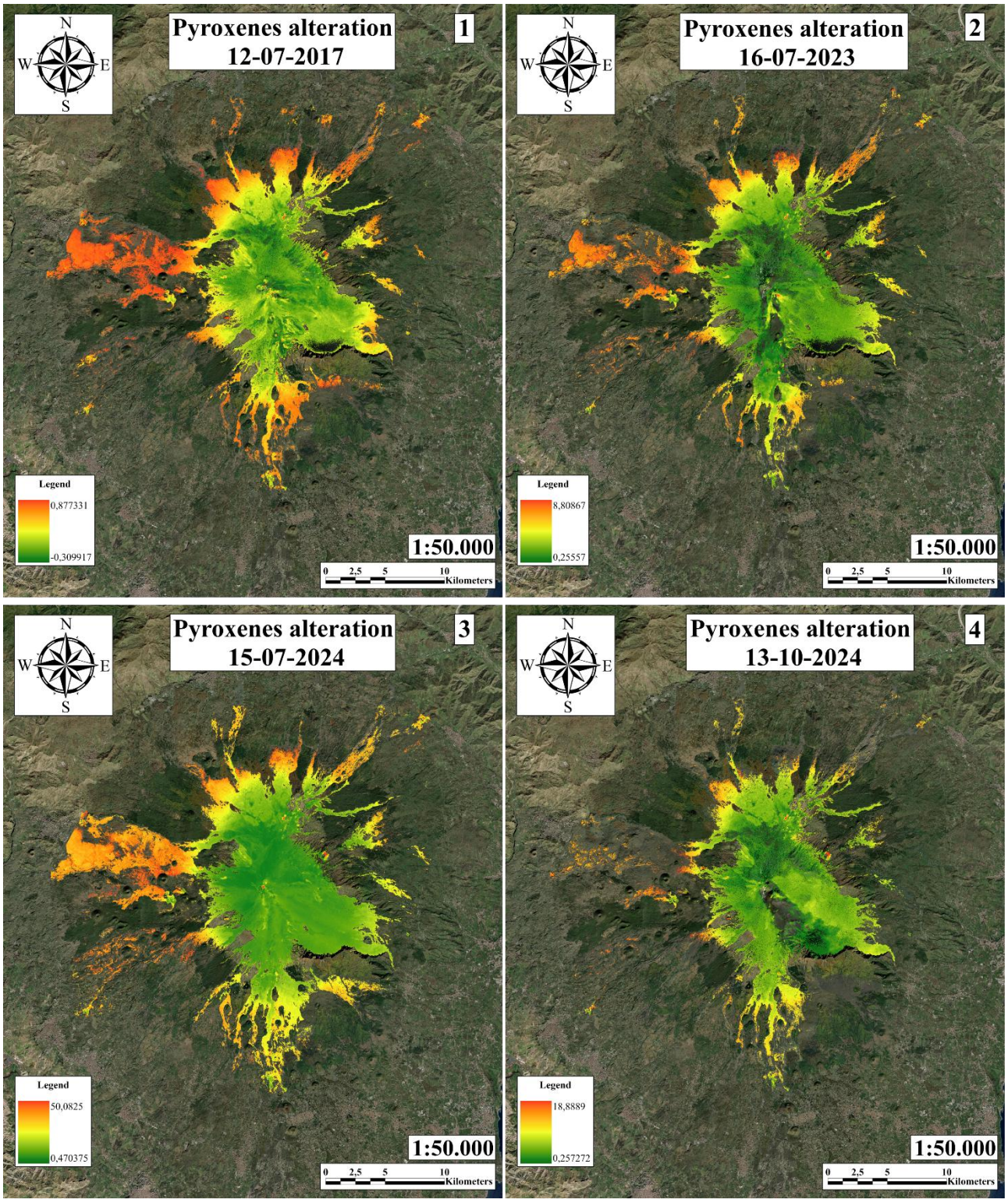

Fig. 26 Pyroxenes alteration index spectral signature images at the Mt. Etna volcano.

6. The **Coarse-grained iron features** index (Fig. 27) like the iron oxide index demonstrate that the iron alteration process can be a good time indicator since in the time series there is almost no difference of values for the same areas at all. This index yields better results since it is possible to distinguish macro-zones like “Valle del Bove” that have less reflectance compared to the surrounding. This is because there is at least a millennium of difference from Valle del Bove lava flows and the surroundings, there is also a very young lava flow that appear with very low reflectance value since it did not have still experienced the iron alteration. The problem of this index is the high sensitivity to the facies of the rocks. The pyroclasts have lower values than the lava flows. This could generate fake-values where the lava flows locally show scoriaceous levels or are covered by successive fall deposits. The ring that was very visible in the images of the iron oxide index (Fig. 23) is less highlighted but since there are no possibilities to use this index to estimate the lava flows age, it is useless to proceed to further refinements and analysis.

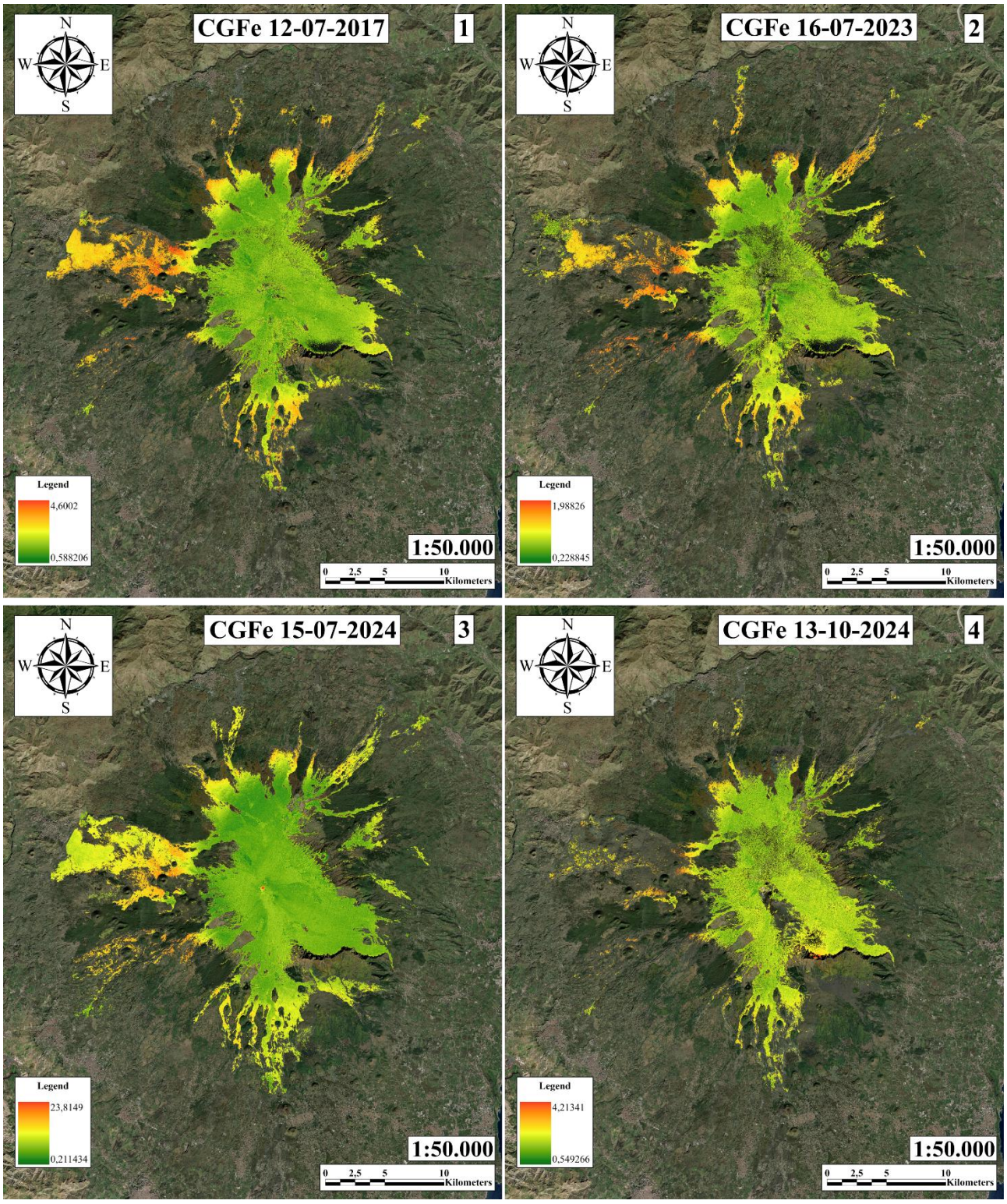

Fig. 27 Coarse-grained Iron index spectral signature images at the Mt. Etna volcano.

7. The **Bivalent and trivalent iron** indexes (Fig. 28 and Fig. 29) were developed taking into account the previous results related to iron oxide and coarse-grained iron indexes. The idea to combine bivalent and trivalent iron indexes starts from the assumption of the inverse correlation between the content of bivalent iron, decreasing with time, and of the trivalent iron amount, which increases in time with the duration of weathering. The comparison of the two index images clearly evidences the complementarity of the results, confirming the inverse correlation of the two reflectance values. In the time series this inverse correlation is still valid in all the four dates images meaning a low sensitivity of the indexes at the seasonality. Stable values in time are also assured by evidence that the bivalent iron needs more time than the 6 years analysed to transform in trivalent iron in a detectable amount. In both the indexes the lava flows boundaries are well displayed especially where the youngest lava flows cover older ones, so the reflectance contrast is high. The ring caused by mosses and lichens growing on the rocks is not even represented in these images meaning that these indexes have a very low detection of the presence of this kind of flora.

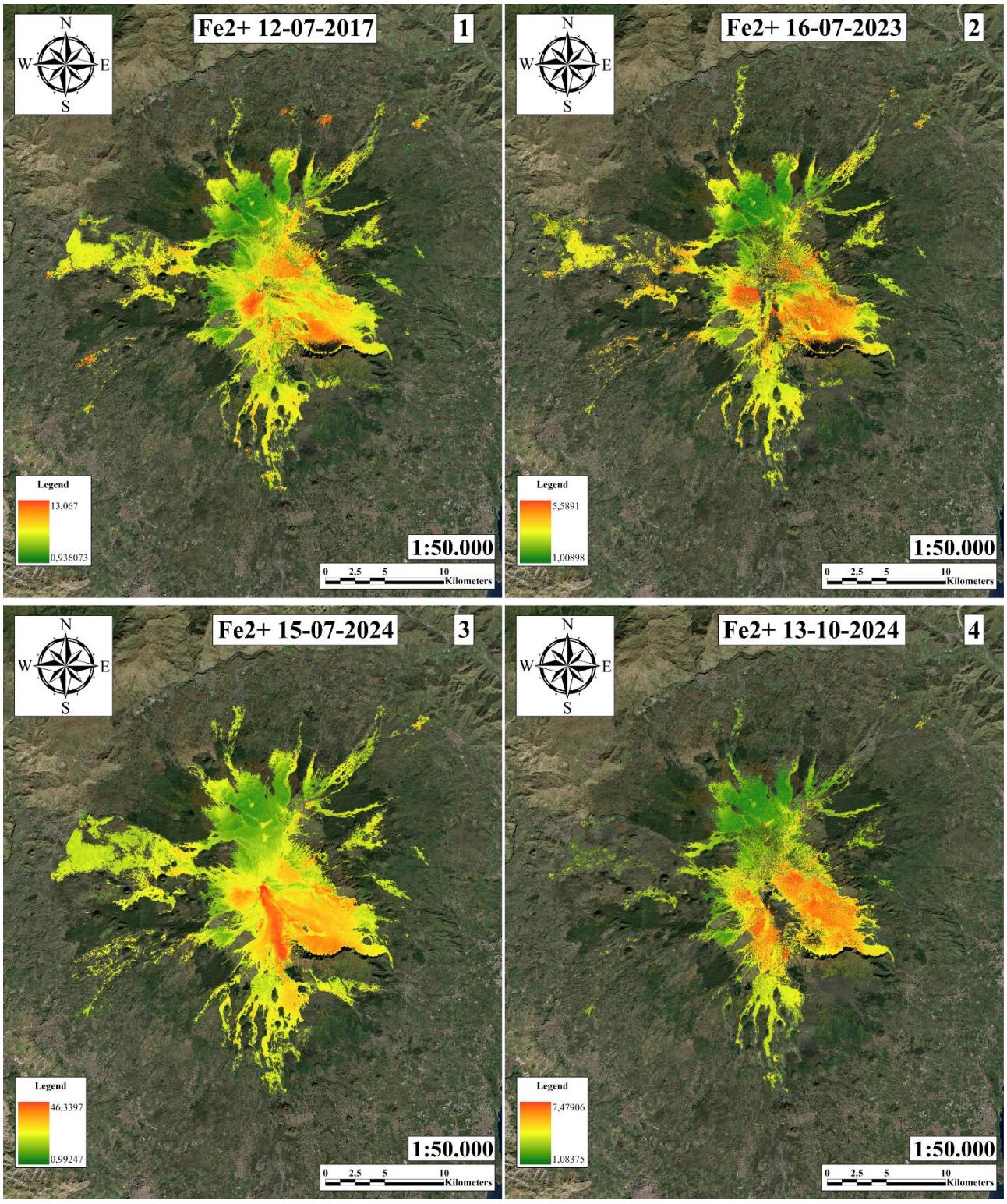

Fig. 28 Fe2+ index spectral signature images at the Mt. Etna volcano.

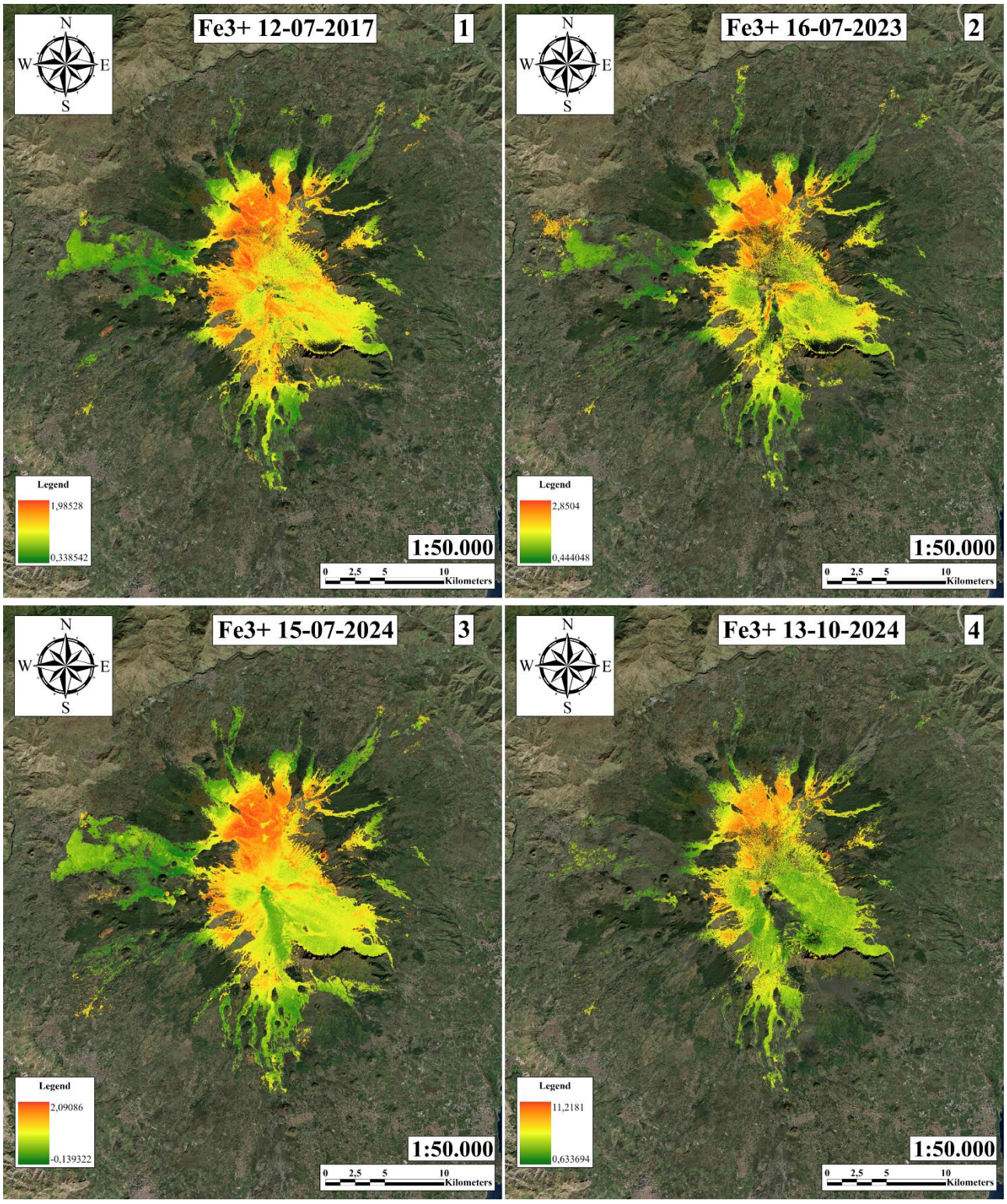

Fig. 29 Fe3+ index spectral signature images at the Mt. Etna volcano.

For a better comparison, the two indices were combined in a band ratio (Fe^{3+}/Fe^{2+}) (Fig. 30), where the higher the reflectance values the older are the lava flows. The analysis with the geological maps allowed to compare the rocks facies (massive lava, pyroclasts, ash, …) with the reflectance values, this permitted to exclude any role of the different facies in the final reflectance results. This new band ratio demonstrates the accuracy of the method since overlapping the geological map it is clear that the lava flows rim highlighted in the band ratio images represent the real ones. The time resolution of this method was calibrated by comparison of reflectance images with the geological map. The comparative analysis evidenced that reflectance variations can provide a time-resolution of about a century in discriminating the lava age. This means that this index is the proxy best fitting the lava age, combining the more accuracy and time resolution of all the others, also having the lowest sensitivity at the noise caused by natural factors.

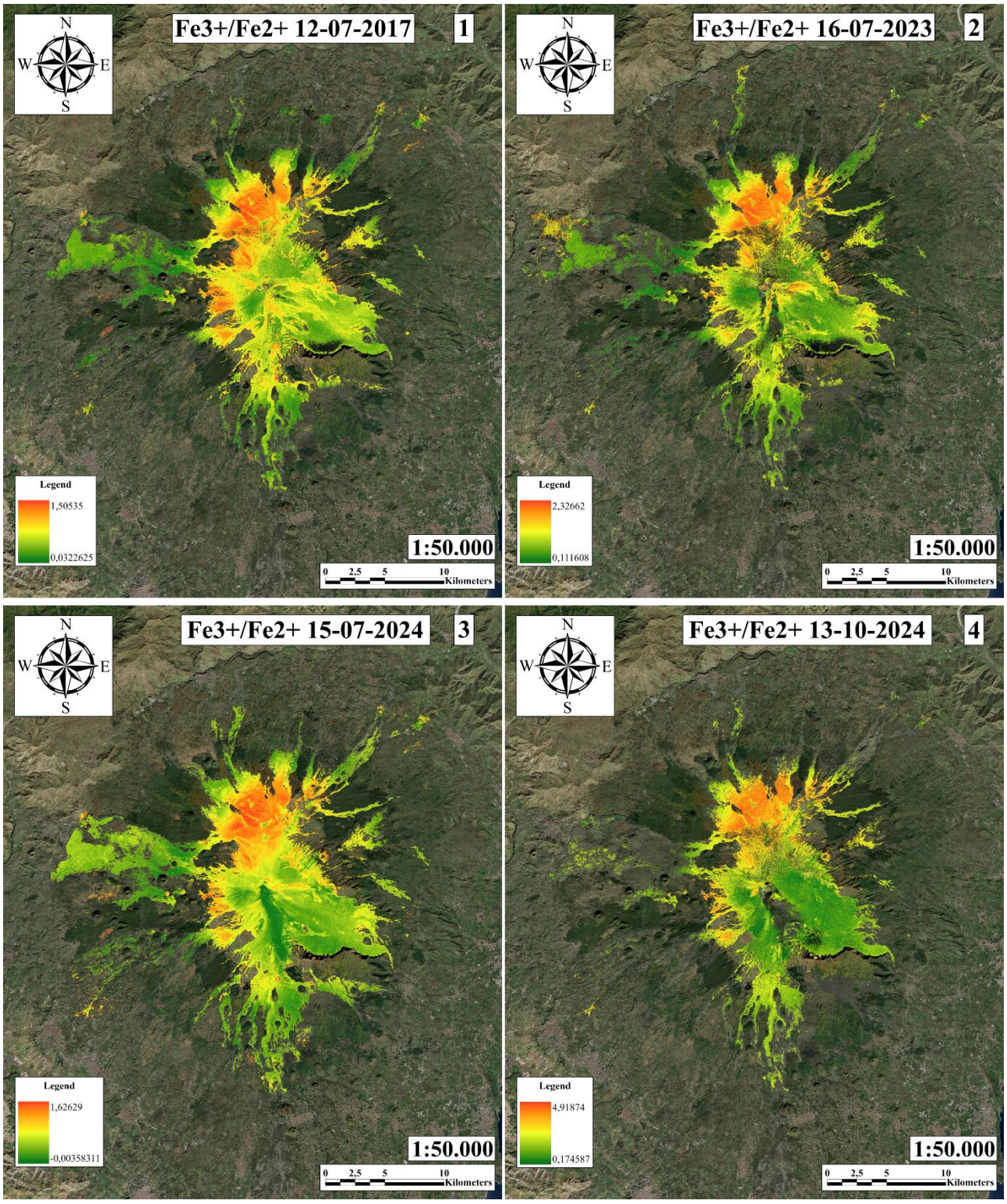

Fig. 30 Fe3+/Fe2+ ratio spectral signature images at the Mt. Etna volcano.

3.2 STROMBOLI

Stromboli volcano from the beginning was a challenge since its area is about a hundred times smaller than Etna volcano, so the analysis, after deleting all vegetated area, was performed in a very small area compared to the Etna one. The satellite imagery used for Mount Etna covers an area of 2500 × 2310 pixels at a spatial resolution of approximately 12 m, whereas the corresponding imagery for Stromboli is more spatially limited, measuring 2500 × 1131 pixels with a finer resolution of about 7 m. The proximity to the sea, since it is an island, could create some artifacts caused by the marine spray that must be considered as they can alter the moisture content near the coast. Stromboli is one of the most active volcanoes in the world, this causes an issue in the top crater where it can be registered reflectance values so high in the infrared wavelength, that a flare appears covering some of the surrounding areas. To avoiding a flattening of all the values in the images where infrared wavelength is involved caused by the flare's too high reflectance values, the top crater area was clipped, even after this some extensions of the flare is still visible in the final images. The age of the outcropping volcanic rocks where derived from the geological map published by the University of Fribourg (Keller et al., 1993)(Fig. 31). Only two dates were analysed (1) 12/07/2017 and (2) 30/06/2024 because, since it is an active volcano, it is easily covered by a plume of gas, while the interaction with the sea can produce clouds that cover the volcano. The Stromboli volcano was analysed utilizing 6 band ratios. 5 of them have been chosen from the Etna case-history, while an additional ratio was developed in this analysis.

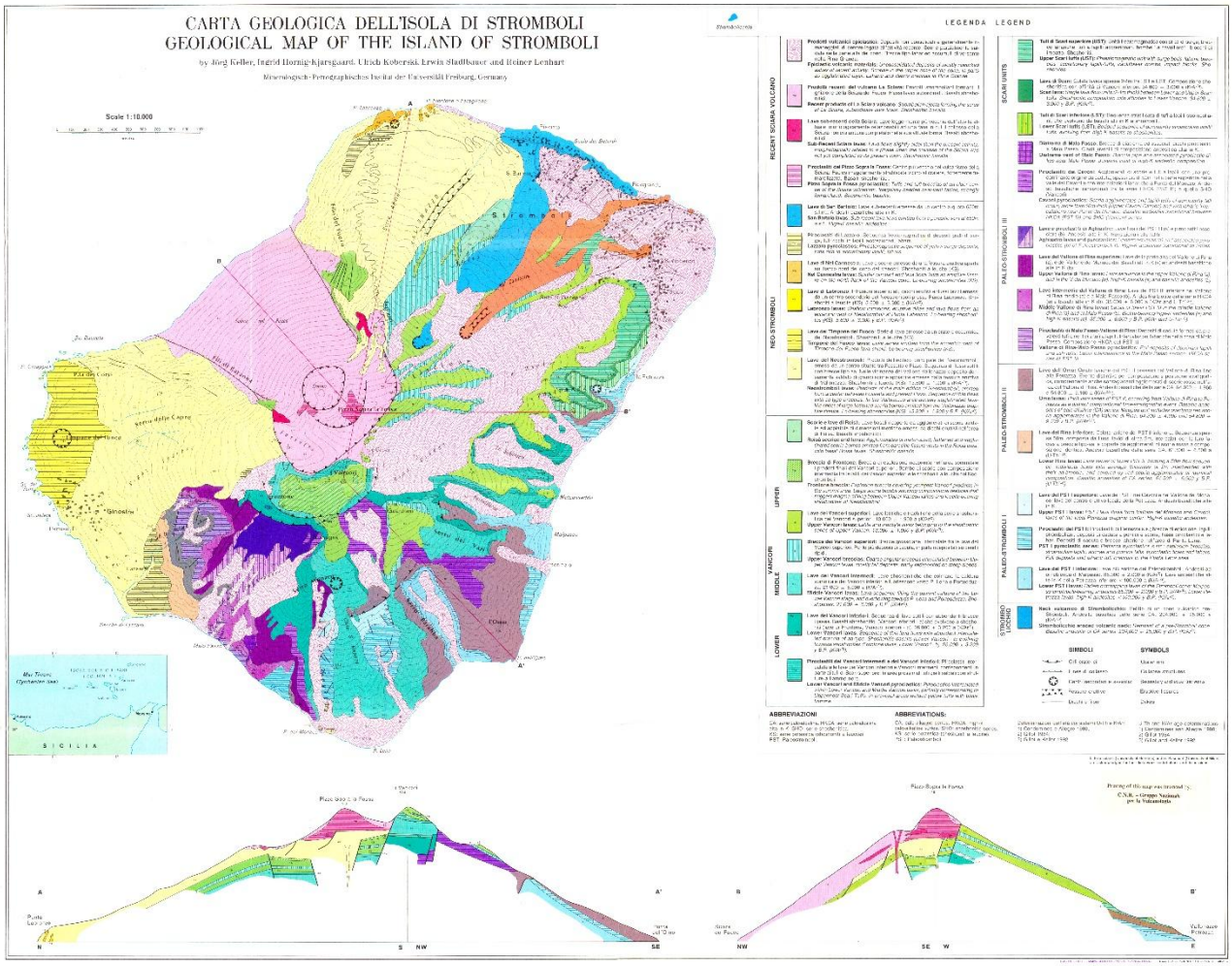

Fig. 31 Geological map of Stromboli volcano (Keller et al., 1993).

1. The **Argillification** index (Fig. 32) showed better results than in the Etna case-study. This is probably due to the higher slope gradient of the Stromboli volcano that favoured a different weathering of the products exposed on the volcano flanks. The images highlight some of the oldest lava flows in the study area, evidencing a correlation between argillification of the lava rocks and time. This correlation is lost in the "sciara del fuoco" region, where some morphological features create natural traps for the clay that was washed away from the top area. The clay traps are evidenced in the images as higher reflectance areas, regardless the age of lava flows. So, in Stromboli there is the same issues found in the Etna analysis, meaning that this index is valid only in absence of erosion, transportation and accumulation areas.

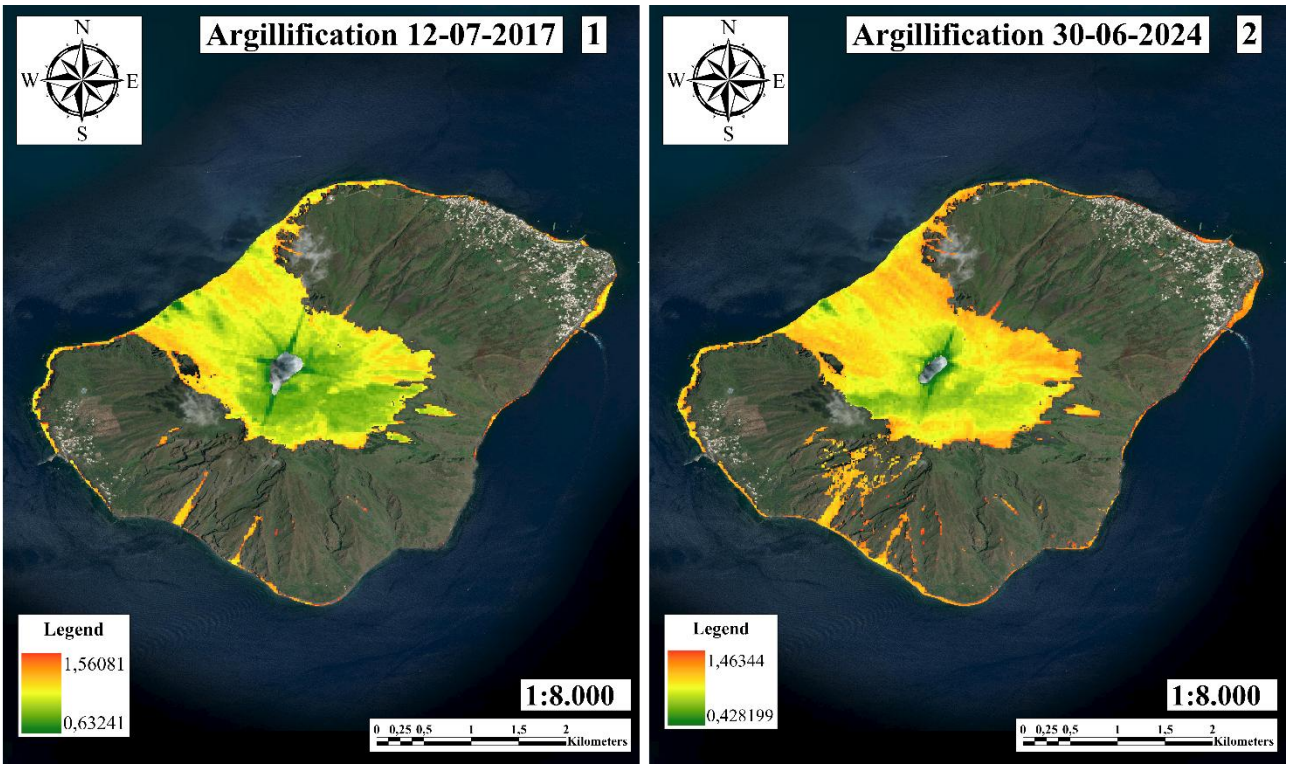

Fig. 32 Argillification index spectral signature images at Stromboli.

2. The **Sulphur content detection** index (Fig. 33) offers valuable results as demonstrated on the Fig. 33-1 where the oldest rock outcrops show higher values than the youngest ones. An artifact is still visible in the Sciara del fuoco area, probably caused by runoff of meteoric water. As shown in Fig. 33-2, reduced image contrast results in a flattened appearance, the oldest rock outcrops are barely distinguishable, likely reflecting a decrease in values associated with lower sulphur content in the rocks. In the Sciara del fuoco, the runoff area is more evident. This means that an abundance of rainwater can easily dissolve the sulphur from the rock surfaces resulting in a lowering of the reflectance values. In conclusion, it is possible only to estimate the abundance of sulphur deposits cumulated on short terms in very dry conditions. As the index is linked to weather conditions, it was excluded from further analysis.

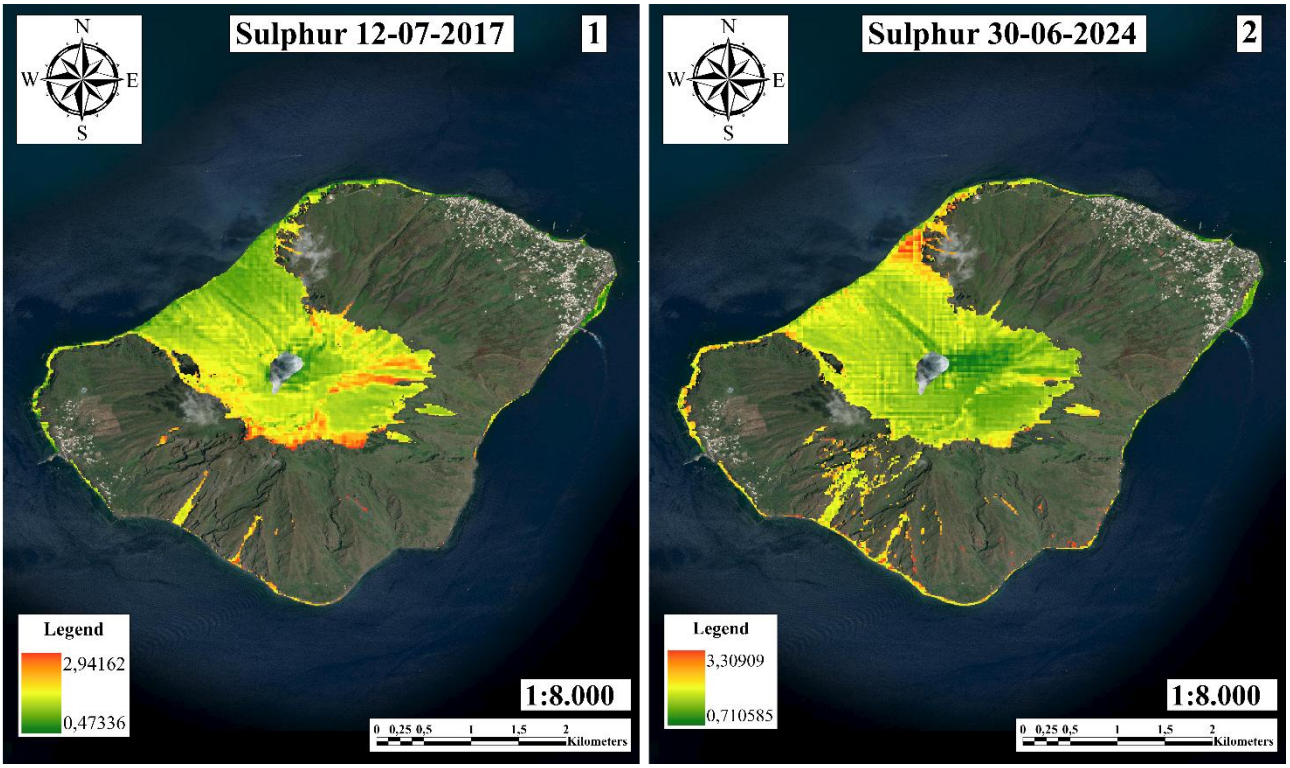

Fig. 33 Sulphur content index spectral signature images at Stromboli.

3. The **Iron oxide** index (Fig. 34) results in similar reflectance values in both the images, the oldest rocks have lower reflectance values than expected, despite their age implying long period for oxidate. In both the images, two “pools” with higher values are highlighted. They refer to trap areas where iron oxide, eroded from the top of the volcano accumulated. Even in these images is visible the relation between slope evolution processes ad reflectance values, as in the case of the channel in the Sciara del Fuoco. There, the re-cycled iron oxides deposited on the sides of the streamflow. This is appreciable from the comparison of the two images where in the Fig. 34-2 is clearly observable the two sides of the channel, while in the Fig. 34-1 there is only the central part perceptible. In summary this index cannot be used to estimate the age of volcanic rocks since is conditioned by the weathering action.

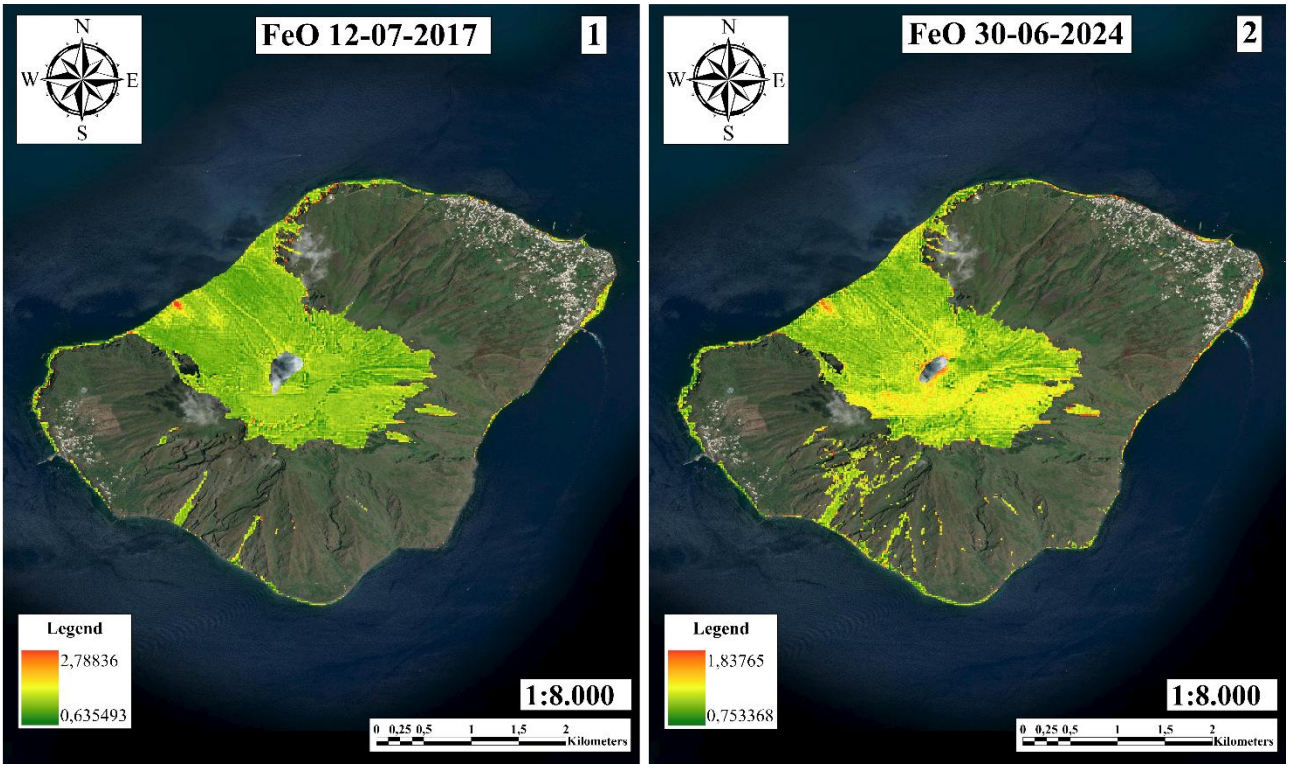

Fig. 34 Iron oxide index spectral signature images at Stromboli.

4. The **Volcanic glass** index (Fig. 35) was conceived to test whether the alteration of the volcanic glass can be a good time indicator. This can be a promising marker particularly suitable for explosive volcanoes, since the pyroclasts and the volcanic ashes are almost totally made of glass too. In the Fig. 35-1 the oldest rocks present a high reflectance values instead of the Sciara del fuoco areas that have low values, with only exception for two areas characterized by very high values. This trend is the opposite of the expected one since older rocks have less glass because of the alteration process, instead the younger ones have fresher glass not yet altered. In the Fig. 35-2 high values of reflectance are confined to two areas of Sciara del fuoco, probably representing local accumulation of pyroclasts and ashes in a trap created by outcropping rocks. To sum up, this index shows very poor results since the trend expected is contrary and the time series have different results.

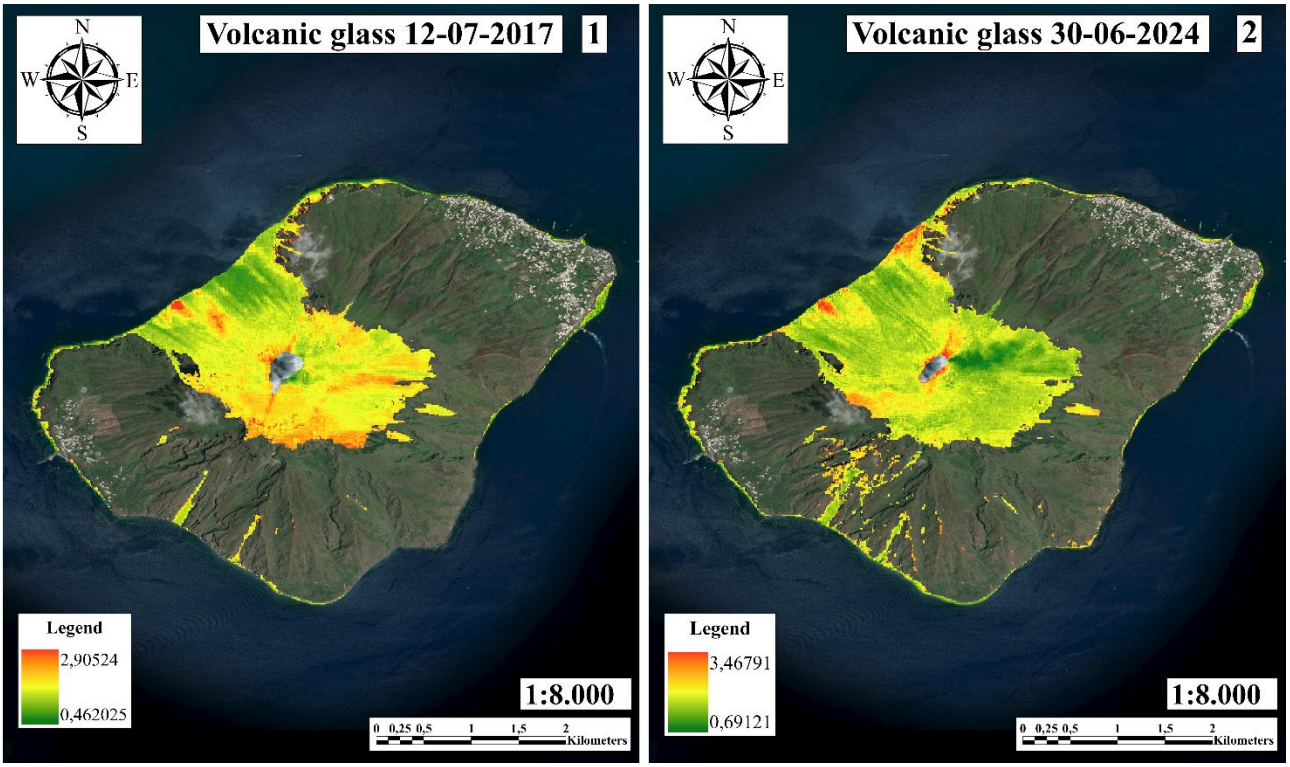

Fig. 35 Volcanic glass index spectral signature images at Stromboli.

5. The **Bivalent and trivalent iron** indexes (Fig. 36, Fig. 37 and Fig. 38) like for the Etna present the better results. In both the dates analysed the oldest rocks outcropping have, as expected, the higher reflectance values than the younger ones canalized in the Sciara del Fuoco and near the top crater. In all the (2) images there is some noise probably caused by moisture in the air, there is even evidence of marine spray in the lowest area of the Sciara del fuoco more visible in the northern part. Like before seen the lithological facies do not affect the result, this is well shown in Stromboli since in a small area there is outcropping rocks near pyroclasts. Once again, this index is capable of the better results in estimating the relative ages of the volcanic rocks, although the low sensitivity at the rocks facies and at the weather conditions confirms the reliability of this analysis in different environments.

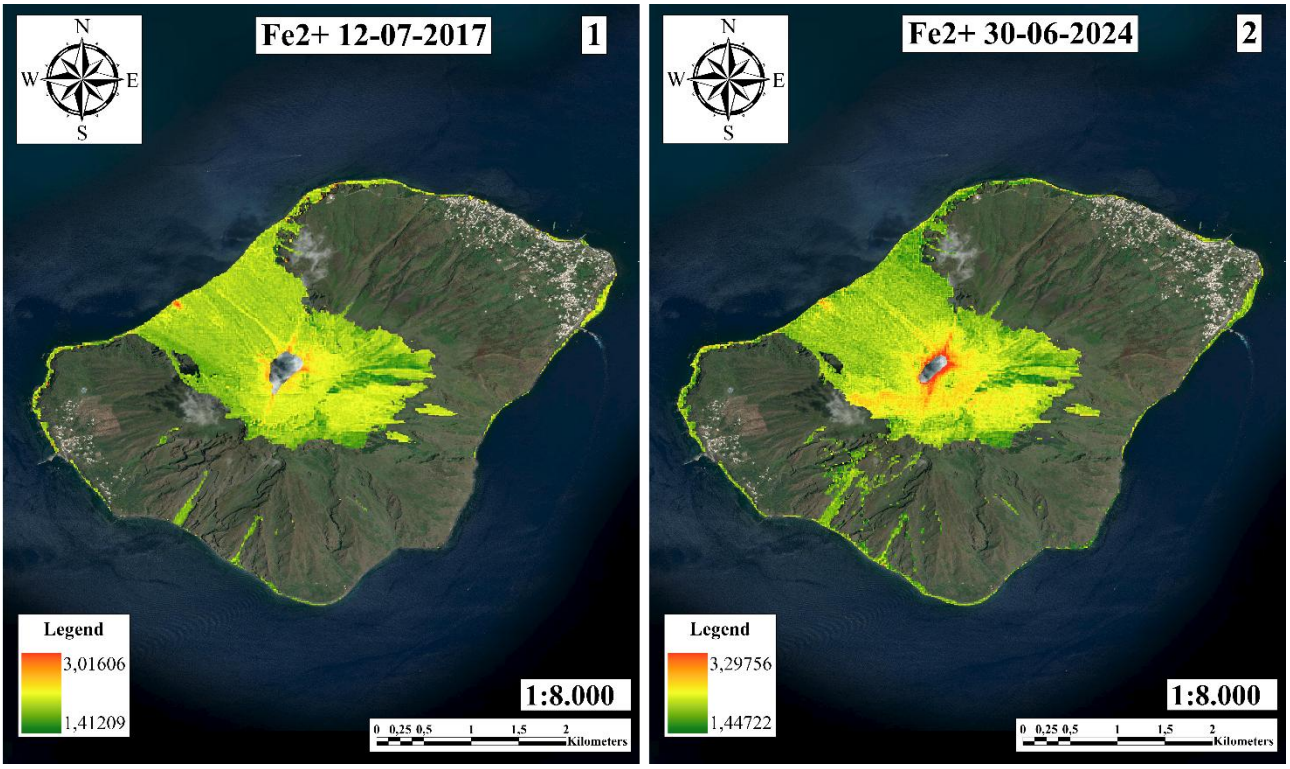

Fig. 36 Fe2+ index spectral signature images at Stromboli.

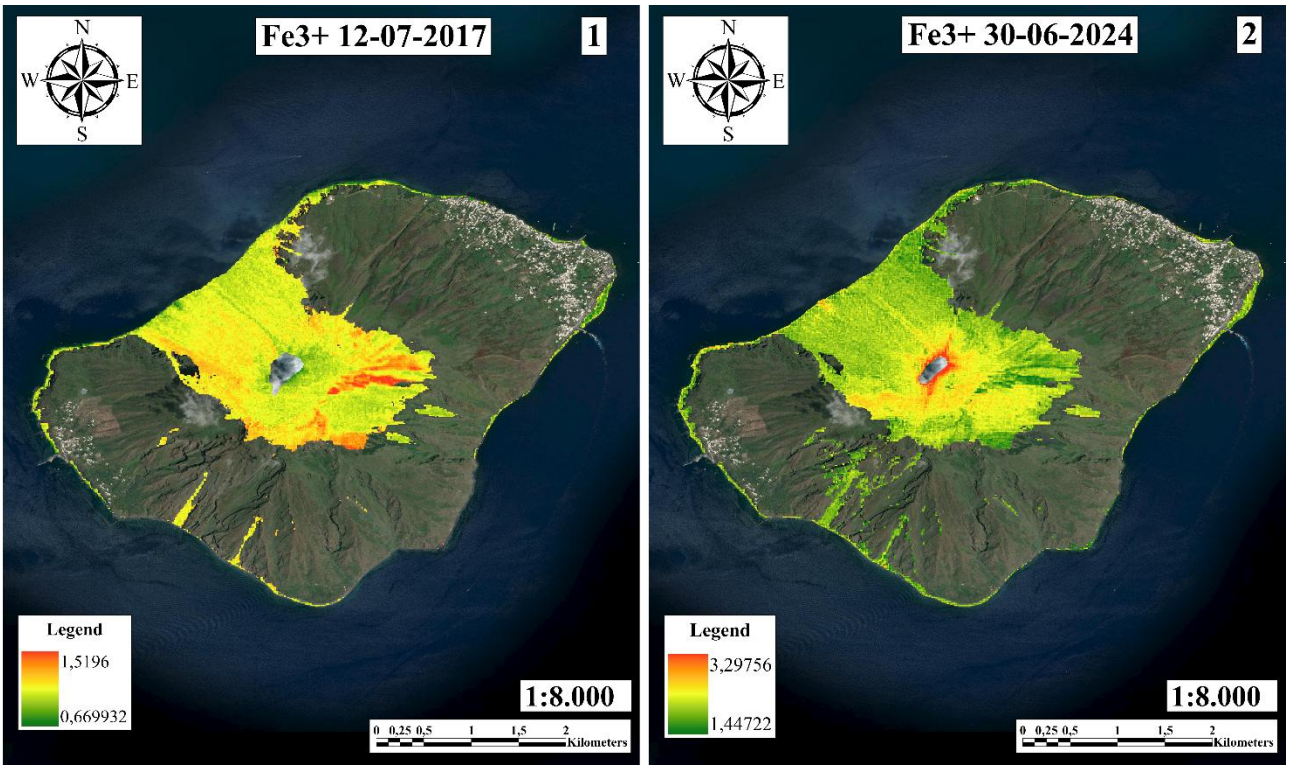

Fig. 37 Fe3+ index spectral signature images at Stromboli.

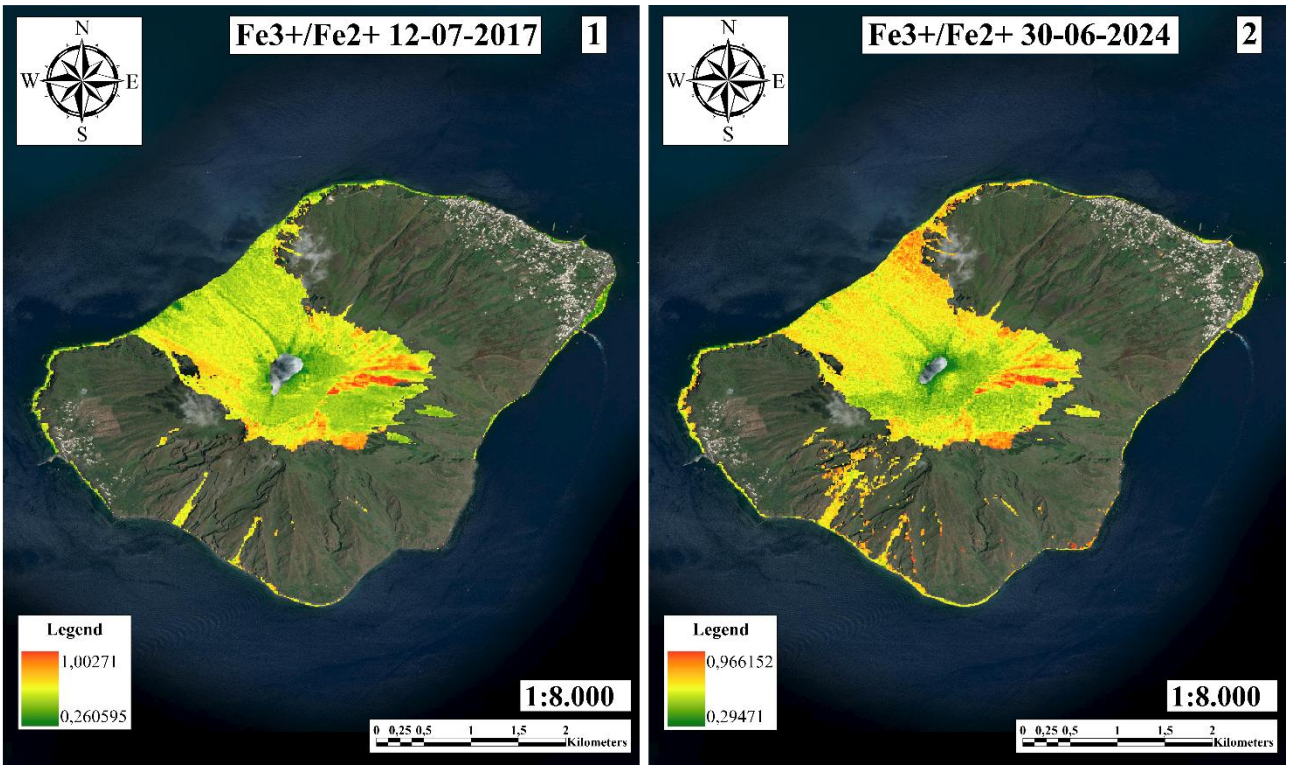

Fig. 38 Fe3+/Fe2+ index spectral signature images at Stromboli.

3.3 GRINDAVIK REGION

The Grindavik region was chosen since the recent emission of lava flows overlaps the ancient ones that have age ranging from A.D. 871 to 0.8 million years ago. This prominent difference in the age of the lava flows provide a very useful case-study to test the reliability of the method on very long period. The age analysis of the outcropping rocks was done through the geological map published by the Icelandic Institute of Natural History (Náttúrufræðistofnun Íslands, 2014) (Fig. 39). In this area only the images of 21/09/2023 was analysed, this because in all other images there is snow or clouds cover the area making impossible the analysis. In the images the area of one of the youngest craters was excluded from the analysis because covered in snow. The little anthropic impact on the region and the shrubs vegetation only in small areas make of this area a perfect environment to apply the method. To analyse this area 6 band ratio was chosen taking in consideration the previous results:

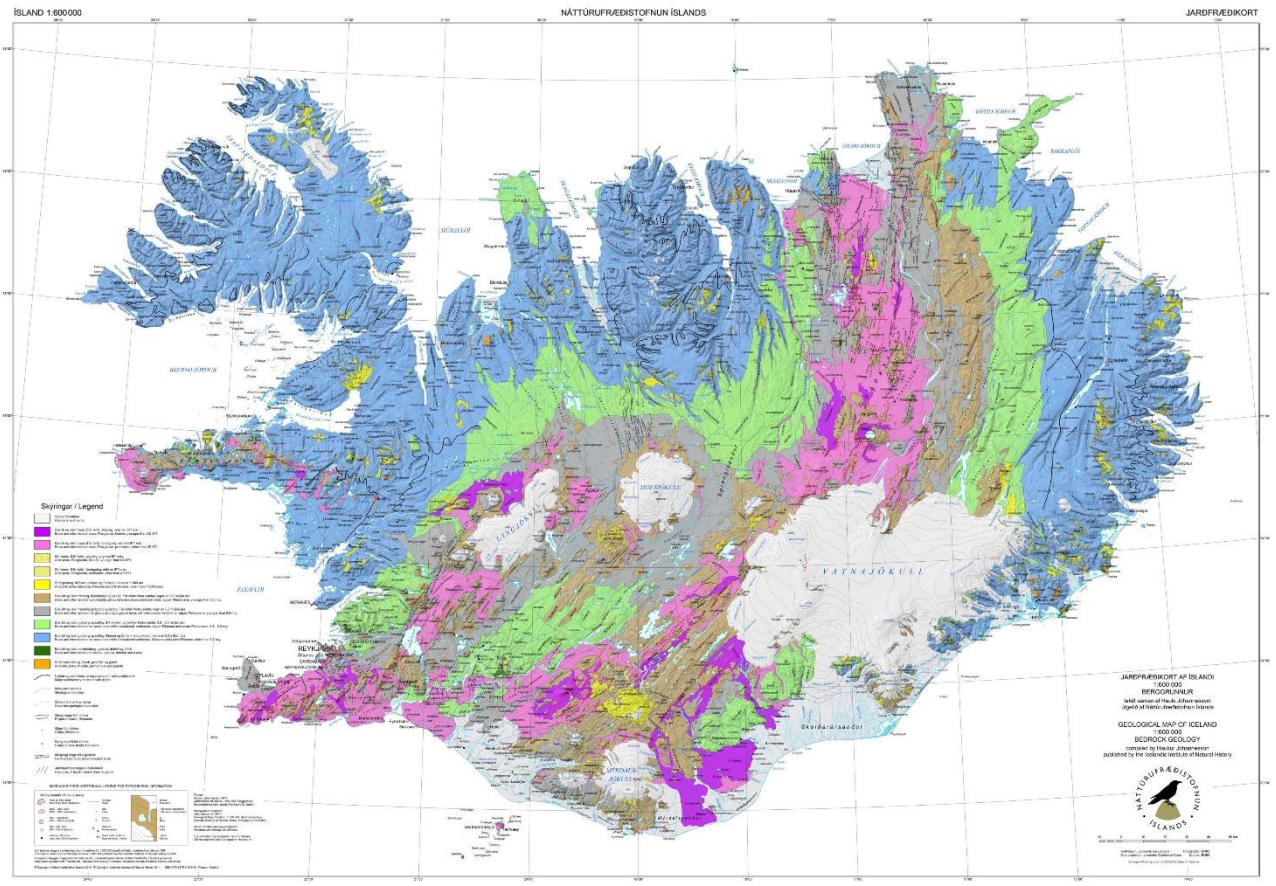

Fig. 39 Geological map of Iceland (Icelandic Institute of Natural History).

1. The **Sulphur content detection** index (Fig. 40) shows a peak of reflectance values in correspondence of the faults system in the eastern part of the image, highlighting the trace of the faults where hydrothermal emissions take places. There is almost no correlation between the lava rocks age and the sulphur reflectance values since the newest lava flows have very low sulphur values like the older ones on the eastern side of the image, the same rocks have higher values in the western part of the formation. Is interesting to denote a correlation between the areas with evidence of faults systems where the sulphur reflectance values have higher values than the areas without faults even if the age of the volcanic rocks is the same. So, this index is easily misleading by hydrothermal activity that can alter the concentration of sulphur in the analysis area.

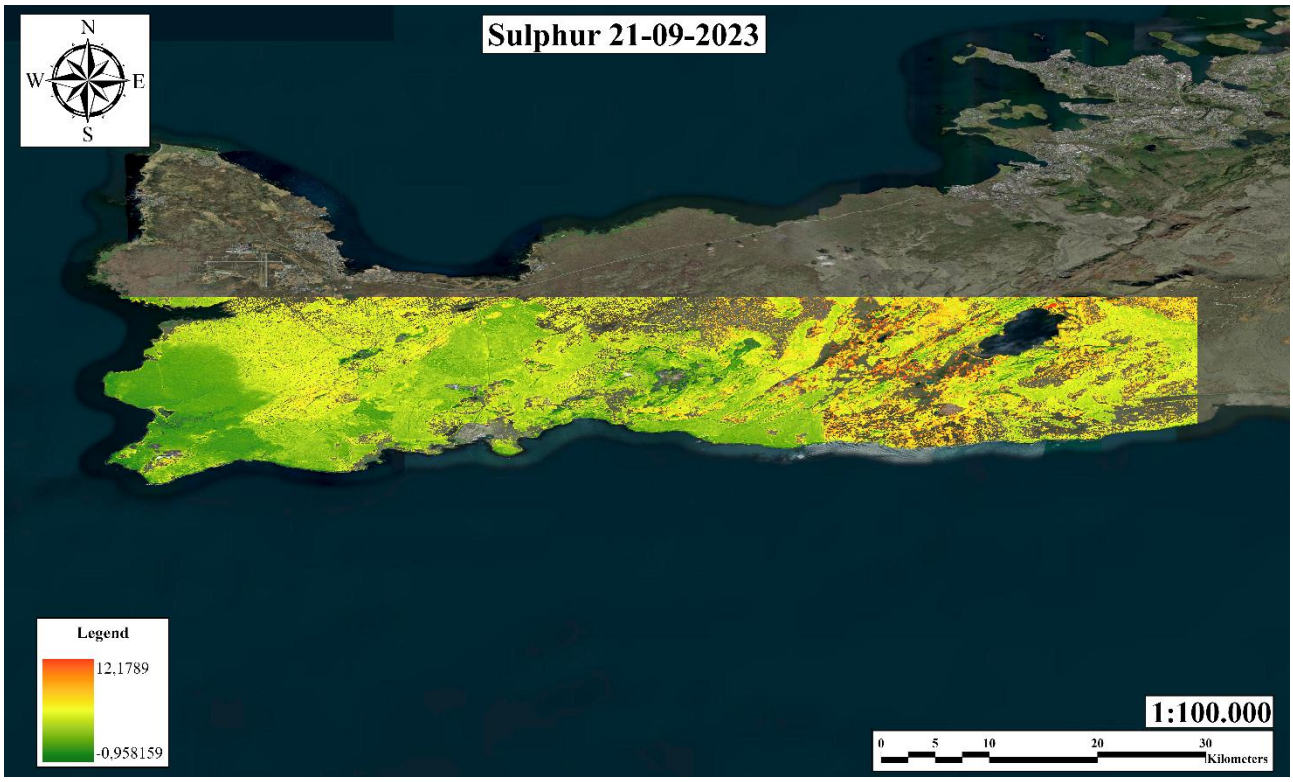

Fig. 40 Sulphur content index spectral signature image.

2. The **Volcanic glass** index (Fig. 41) shows, in two areas near the craters affected by the most recent activity, peaks of reflectance values caused by accumulation of pyroclasts, instead the younger lava flows have lower values than the older ones presenting the opposite of the trend expected. There are very small areas around all the images with high values that can be correlated to pyroclasts and ashes natural traps filled by the eolic deposits, fed by explosive activity during the eruptions. In conclusion this index is more useful to evaluate the deposits of pyroclasts and their alteration and movement around the area but it is not useful at all to dating the lava flows since there is not a direct correlation between this index values and the ages of lava flows.

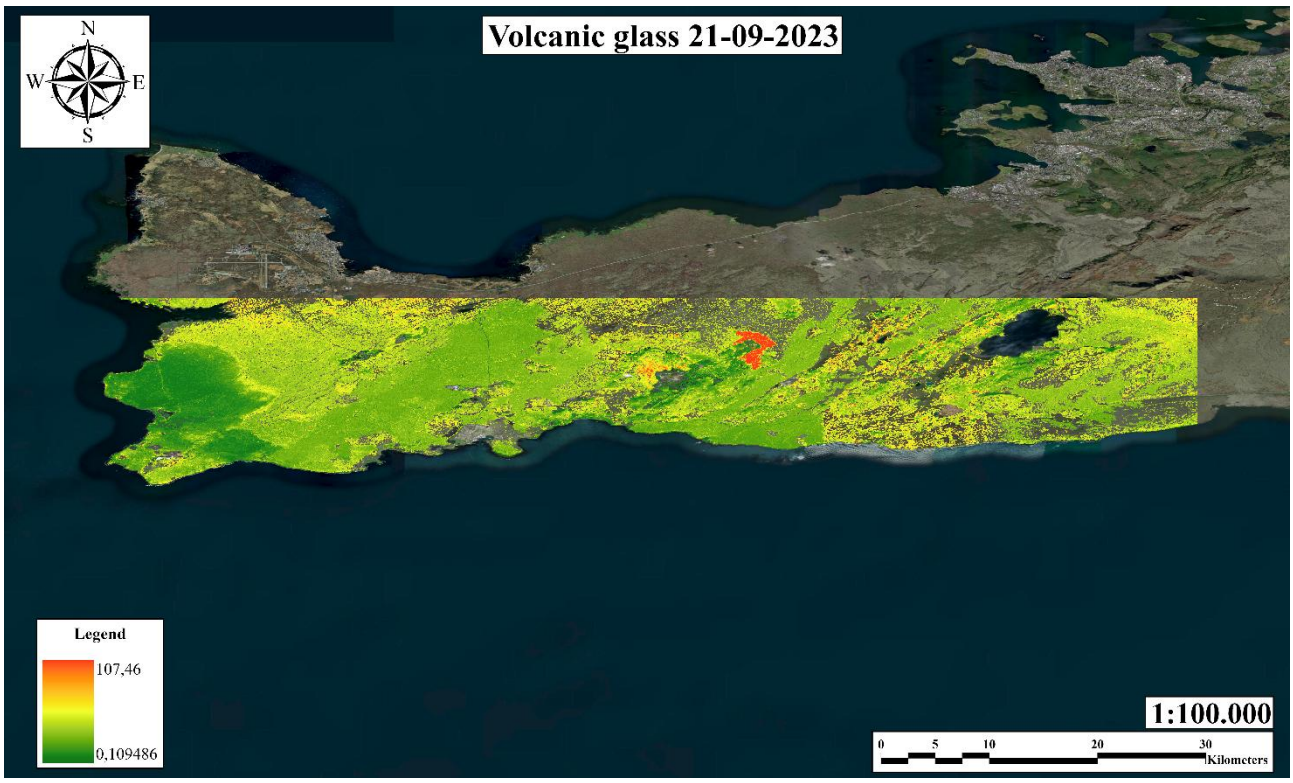

Fig. 41 Volcanic glass index spectral signature image.

3. The **Iron oxide** index (Fig. 42) highlights the same areas evidenced by the volcanic glass index, since the pyroclasts and ashes are easily to alter than the lava flows that, usually, display lower reflectance values. Almost all the lava rocks falling in the image have the same average reflectance values, thus suggesting the absence of a clear correlation between lava flows age and oxidation of the ferrous minerals. Infact the images show an almost mono-colour results meaning that there are no boundaries between the different lava flows. In final analysis this index can be used to estimate the oxidation of very young deposits but after some time the alteration erode the iron oxide levelling all the differences between the different lava flows making impossible to use to evaluate the age of the volcanic rocks.

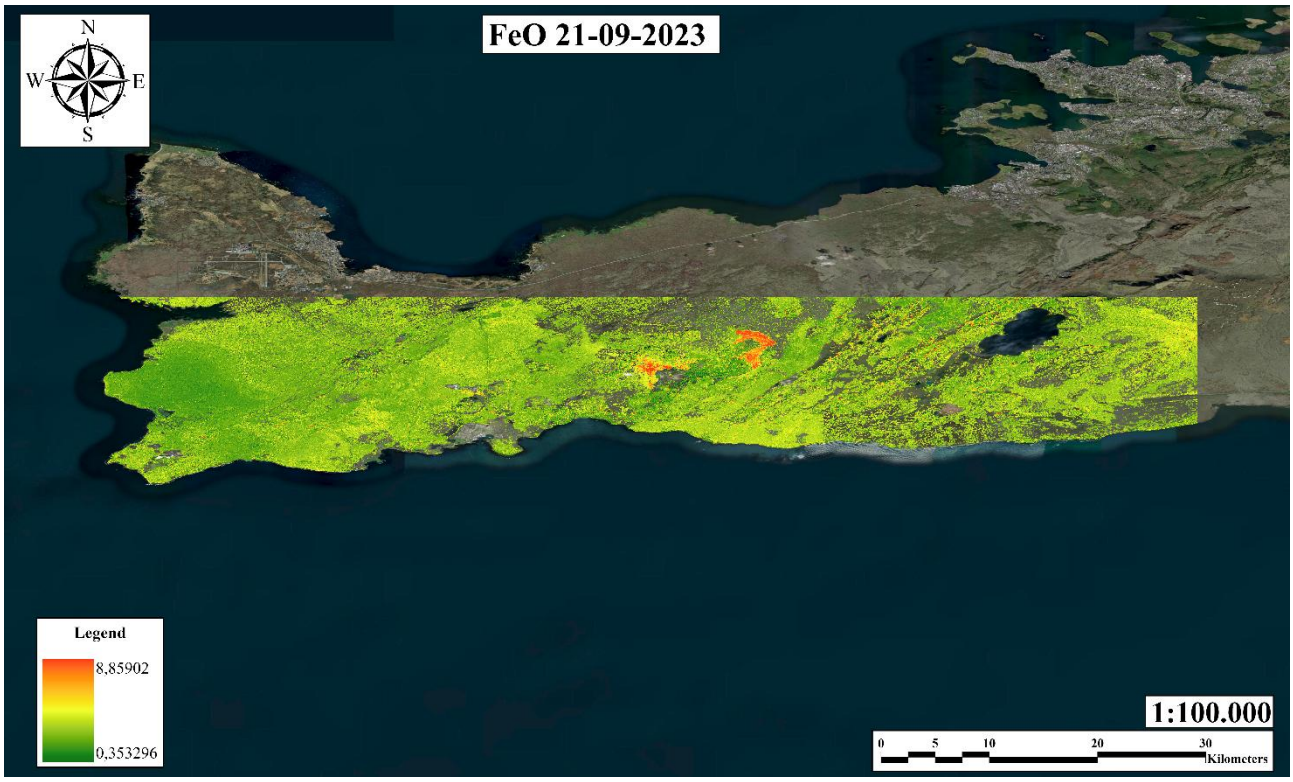

Fig. 42 Iron oxide index spectral signature image.

4. The **Argillification** index (Fig. 43) create, aside the new lava flows that have very low reflectance values, two groups of values. The group characterised by a high reflectance return refers to rocks subject to an advanced state of alteration. The other one, showing low values, more fresher poorly degraded rocks. The trends of the two groups follow the NE-SW of the main fault system in the area, looking more closely can be noticed that the high values of reflectance are matching the valley created by the fault system and consequently the low reflectance return is in proximity of the ridges where the rocks are exposed. We can conclude that it is not possible to correlate the lava rocks alteration with this index because the weathering wash away the clay formed on the surface of the outcrop and create deposits on the natural trap in the valley.

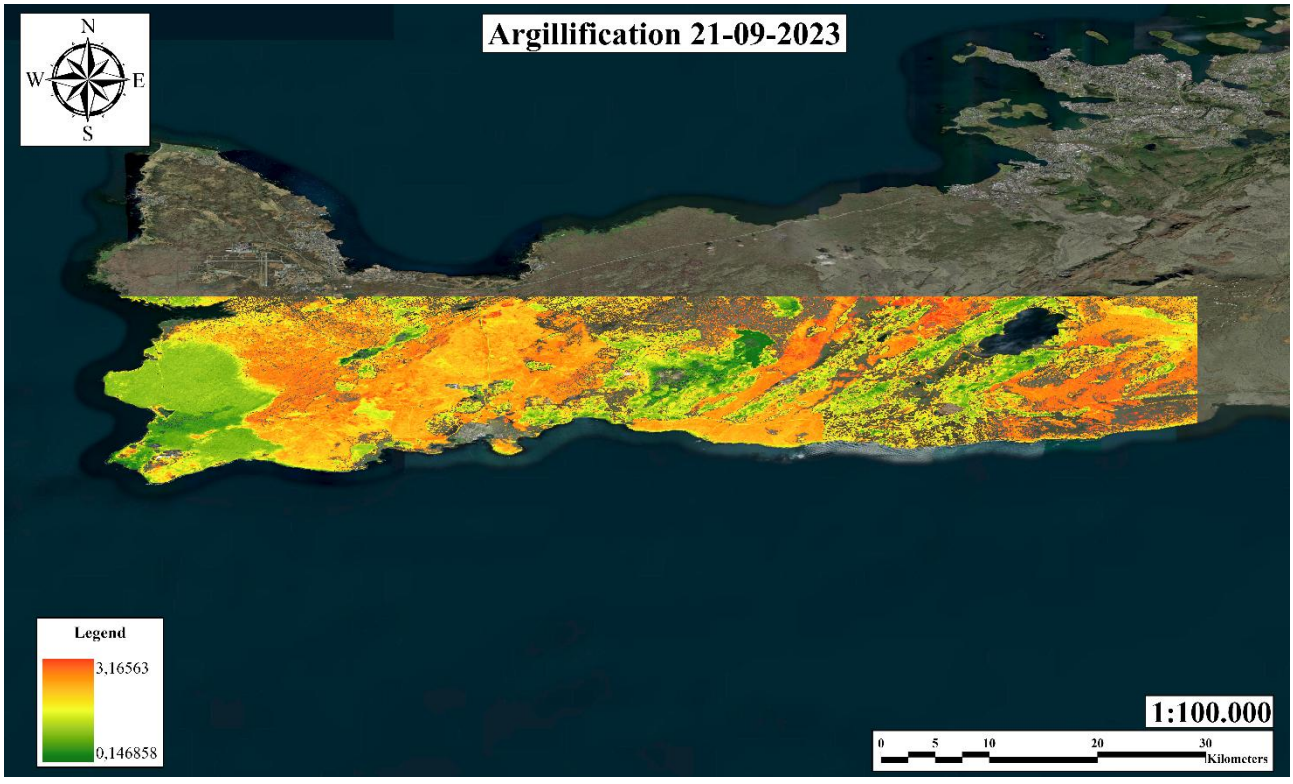

Fig. 43 Argillification index spectral signature image.

5. The **Bivalent and trivalent iron** indexes (Fig. 44, Fig. 45 and Fig. 46) present interesting results since like in all the other cases the younger lava flows have respectively higher and lower reflectance values in Fe2+ and Fe3+. In this case study, the indexes highlight the hydrothermal activity along the main fault system that create some spots of iron accumulation in the same place where the sulphur index shows the same activity. This index has the best correlation with the ageing of the lava flows, excluding the artifacts caused by the hydrothermal spots as demonstrated by the comparison with the geological map, published by the Icelandic Institute of Natural History (Náttúrufræðistofnun Íslands, 2014), well constraining the reliability of the results. The edges of the areas with different values of the indexes almost match the contours of lava flows reported in the geological map, with an appreciable correlation between the reflectance values and the age of the correlative lava units outcropping in the study area.

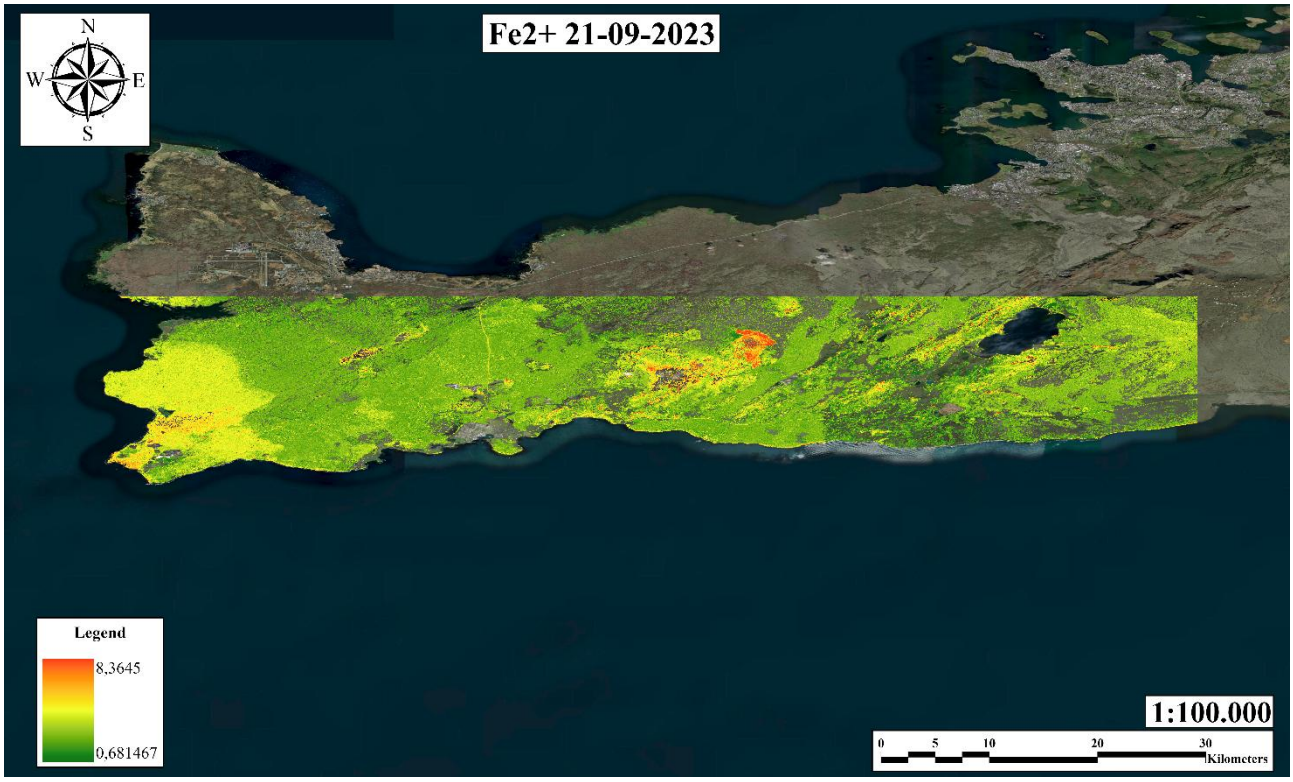

Fig. 44 Fe2+ index spectral signature image.

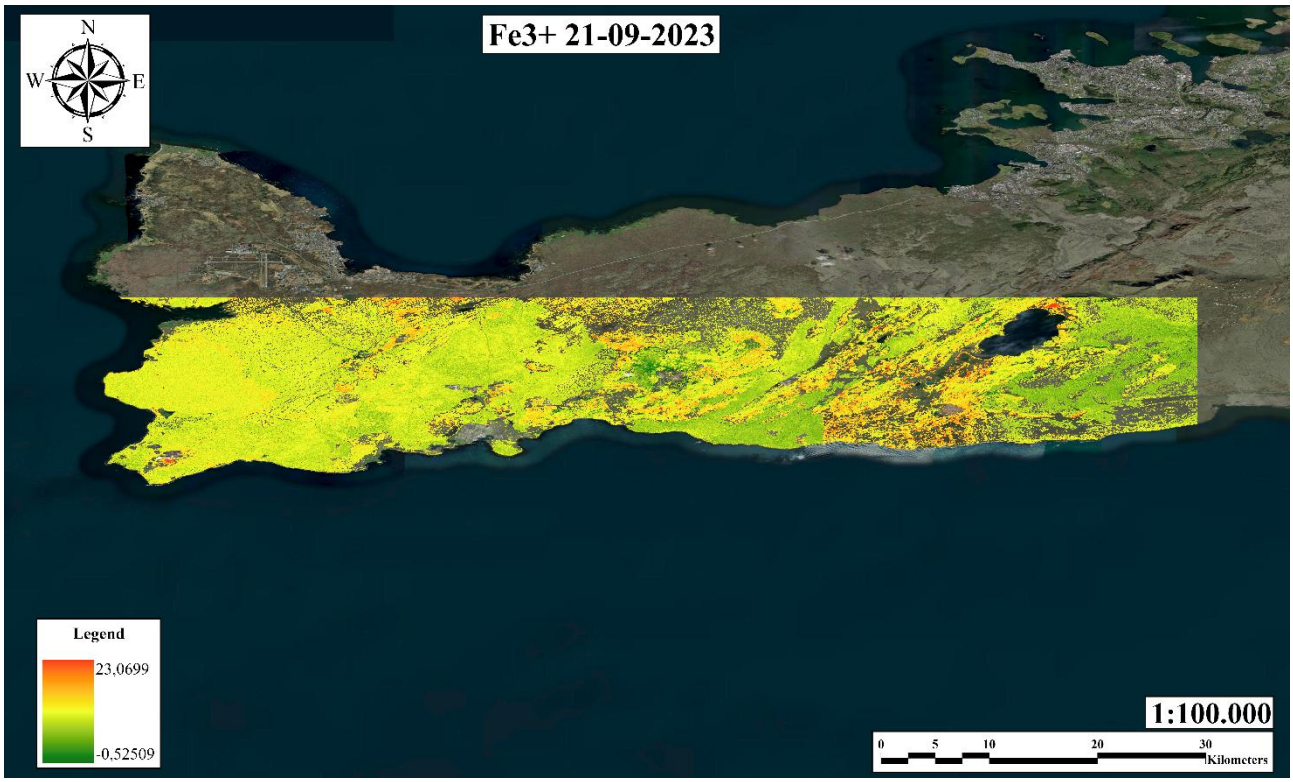

Fig. 45 Fe3+ index spectral signature image.

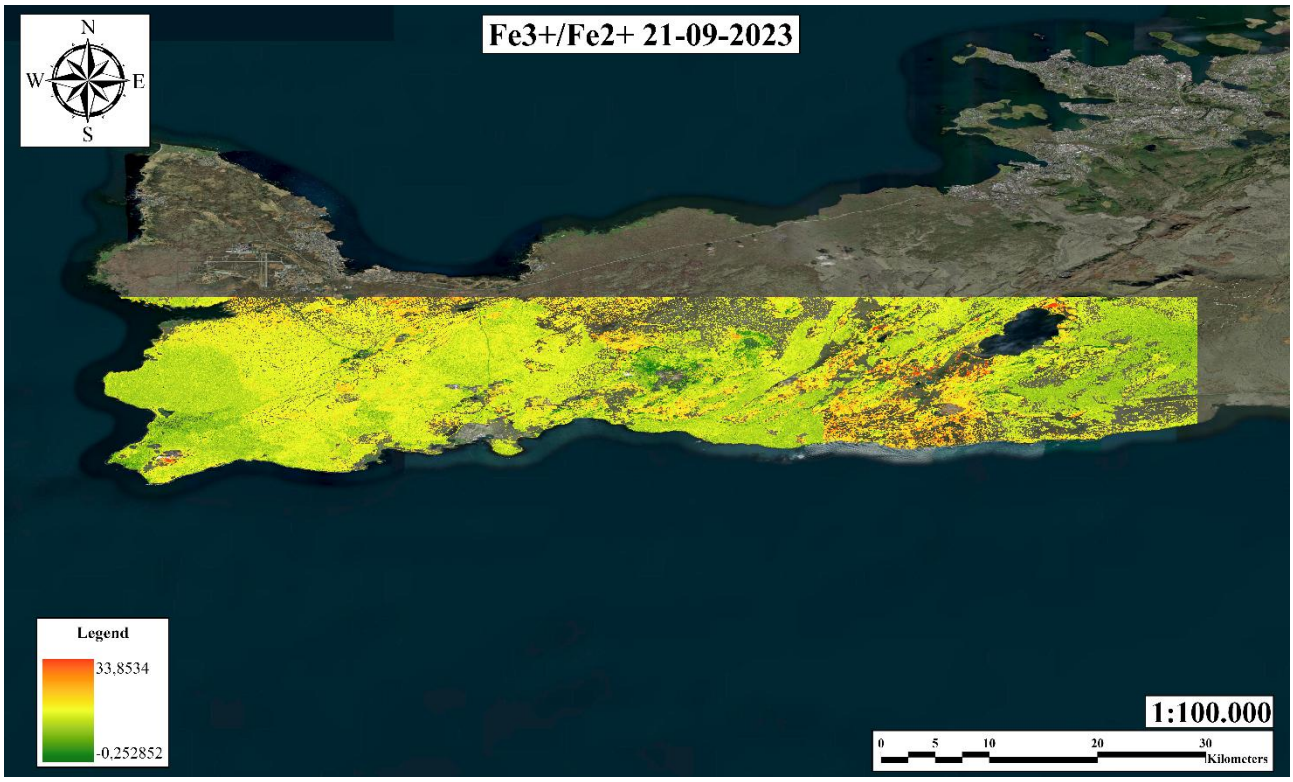

Fig. 46 Fe3+/Fe2+ index spectral signature image.

3.4 ISLAND OF HAWAI'I

The Island of Hawai'i is a perfect training ground for this method since the large area of the volcano allows to collect a lot of data and the almost constant activity produces new lava flows, this make of this study area an excellent test-site for comparison of the reflectance values with lava units ages. The age data were extrapolated from the geological map published by the USGS (United States Geological Survey)(Wolfe et al., 1997)(Fig. 47).The biggest challenge is the constant presence of clouds that cover partially or entirely the volcano, since the Island of Hawai'i receives rain on average between 200 and 300 days per year, making it one of the rainiest volcanoes in the world. In the case of the Island of Hawai'i it was not possible to create a time series since only one satellite image was found with less cloud, so the analysis had to start with cleaning the images from the cloudy areas, because the high reflectance values of the clouds flatten all the other values in the images. Another issue to resolve is the presence of fumaroles in the craters of the volcanoes, due to the impressive hydrothermal activity. The gasses emitted have a very high peak of reflectance values especially in the SWIR region caused by their elevated temperature. To exclude the issues that can cause the flattening of the values due to the craters hydrothermal activity, the top areas of the craters were excluded from the final elaboration. In the Island of Hawai'i area analysis only the bivalent (Fig. 48) and trivalent (Fig. 49) index was involved since is the one that shows best results in the other attempts, although the weather conditions hinder the use of the other methods as very sensitive to all the meteorological conditions. After the creation of the first band ratio images another artifact like a ring was uncovered in the border of the analysis, the moisture normalization can not solve this problem, so it is not the presence of moisture produced by the near vegetation like in the other cases study. The key to untangling the problem was found when we thought that Island of Hawai'i is nearer the equator than the other two analysed, so the solar irradiance is way stronger. This caused a heating of the rocks where there is no vegetation instead of the near vegetation ones where the soil is cooler, so we developed an infrared normalizing method to avoid the generation of this ring

artifact. In the resulting images the contrast between the youngest lava flows covering the older ones is neat, even the youngest lava flows succession is highlighted from change in reflectance values. In the Mauna Kea slopes the monogenic craters shows a elevate hydrothermal activity, that deposits along the slopes of the volcano a grate quantity of oxide among which iron oxide. This oxide oozes on the slope slowly, it can be seen from the comparison of bivalent and trivalent iron images where in the bivalent image is present only the emission points of the fumaroles still in activity. Instead in the trivalent image is visible the flow along the slopes of the older oxides, creating a descent trail from the emission points. In the Mauna Loa volcano the hydrothermal activity in the monogenic craters is appreciable in the bivalent iron image only since it is a recent activity the iron oxide does not had the time necessary to alter in trivalent iron. The succession of recent lava flows on the older rocks outcropping is more clear in the north and south side of the Mauna Loa volcano where the lava flows emitted by the monogenic craters cover the older ones that themselves cover the oldest rocks outcropping in the small areas free of young lava flows. In final analysis the bivalent/trivalent iron method once again resulted in good relatively age detector of volcanics rock, even in difficult to analyse environments like Hawai'i Island where the volcanic activity mixed with the weather conditions create a noisy context for satellite imagery analysis.

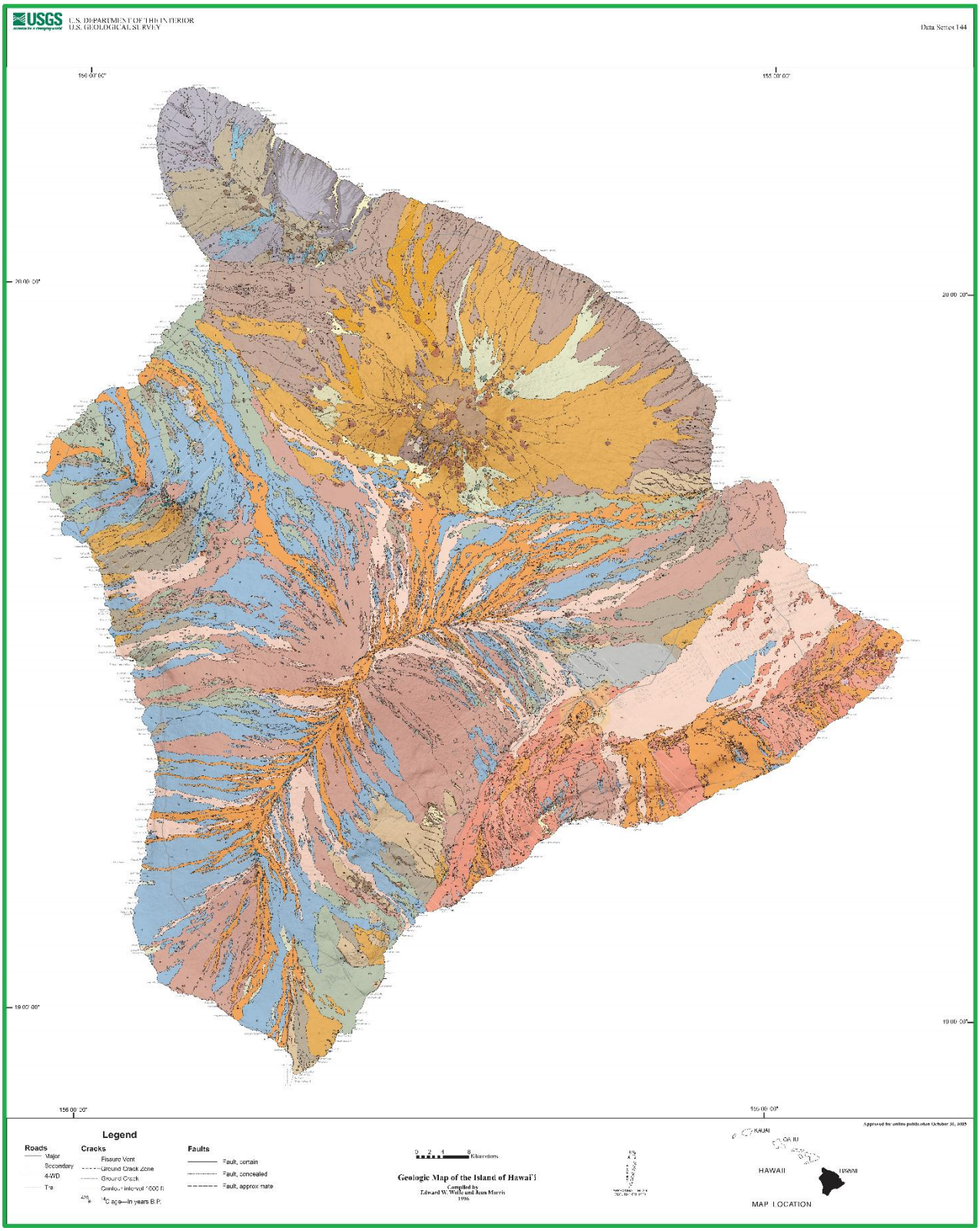

Fig. 47 Geological map of Hawai'i Island (USGS)(Wolfe et al., 1997).

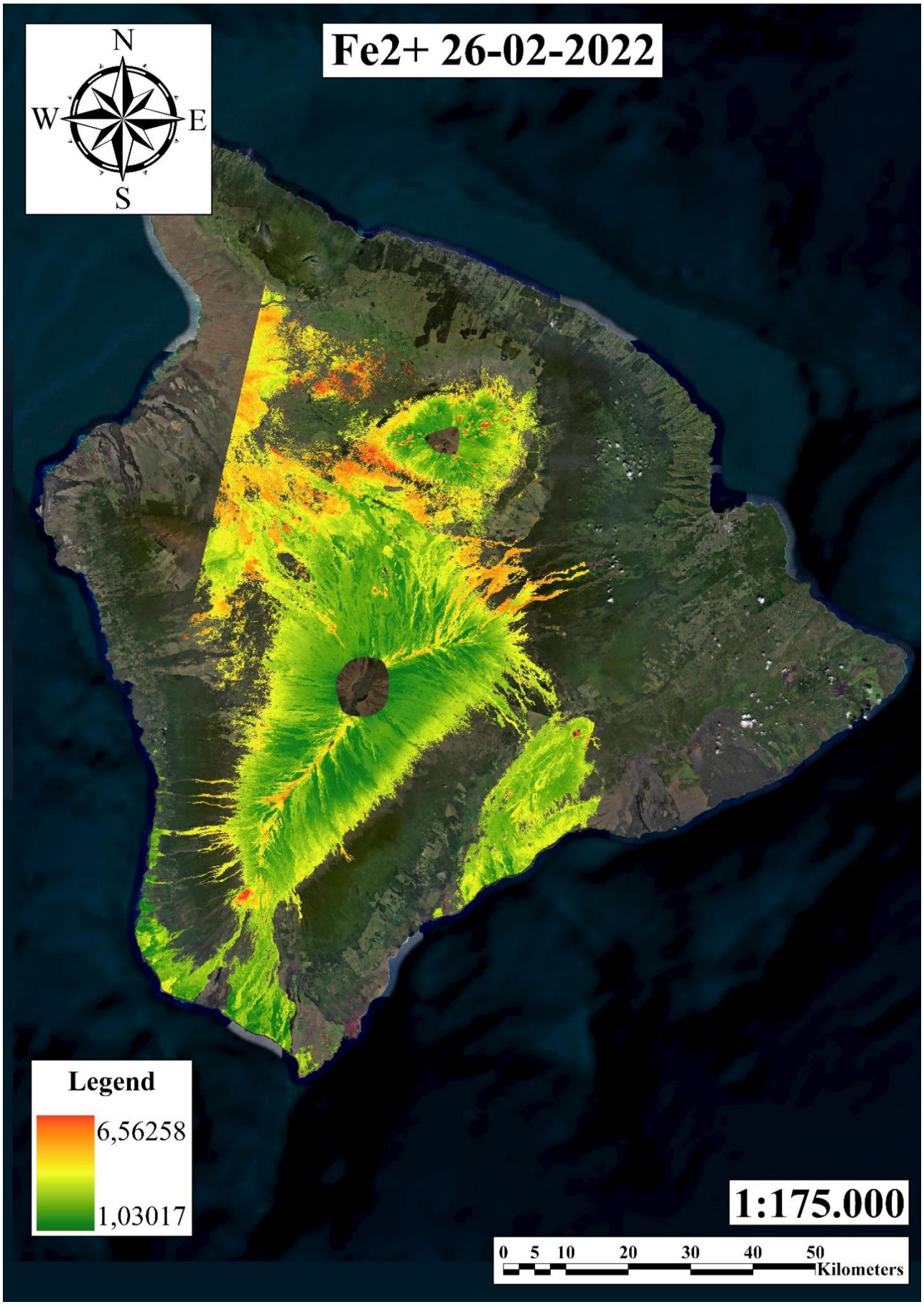

Fig. 48 Fe2+ index spectral signature image.

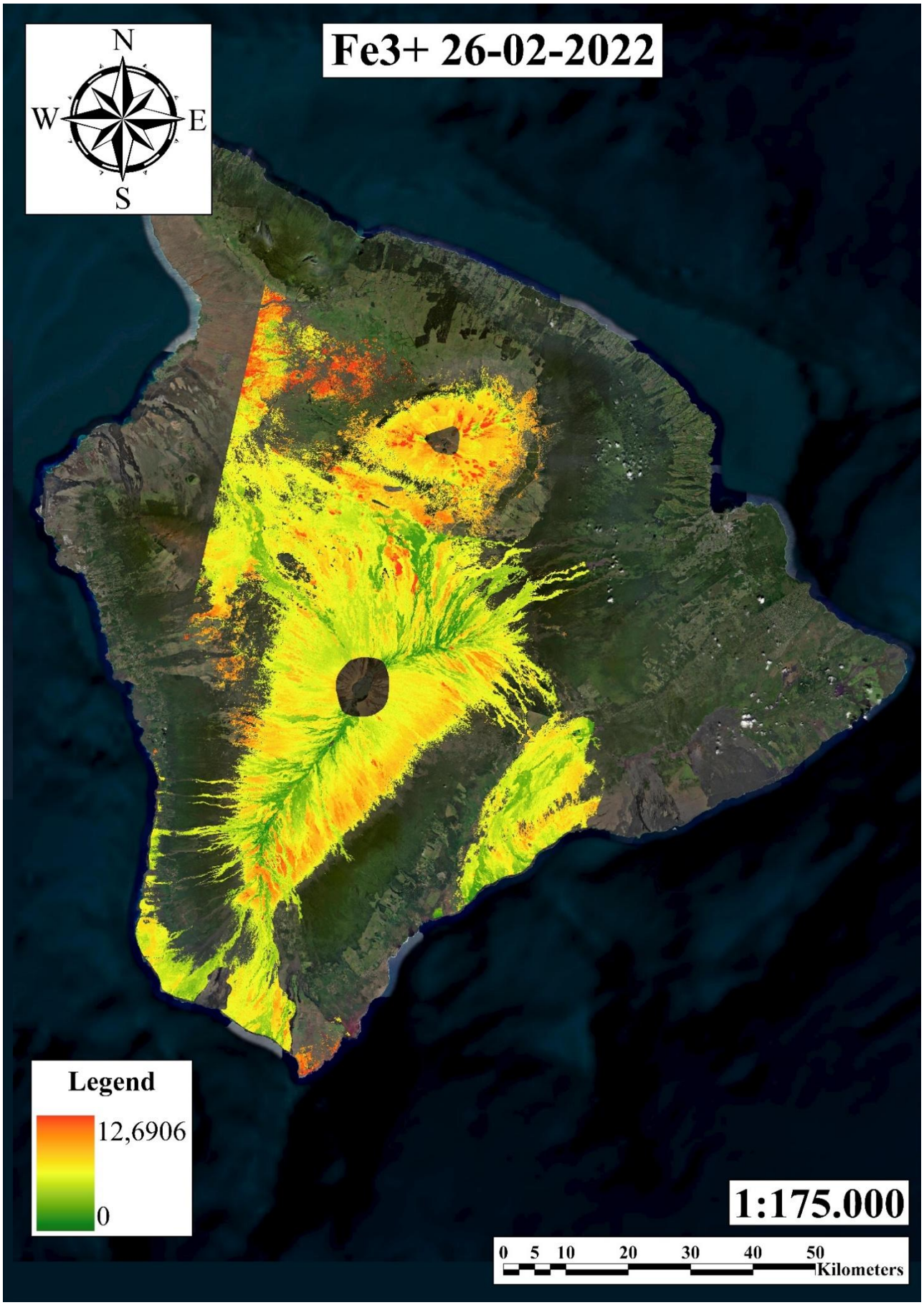

Fig. 49 Fe3+ index spectral signature image.

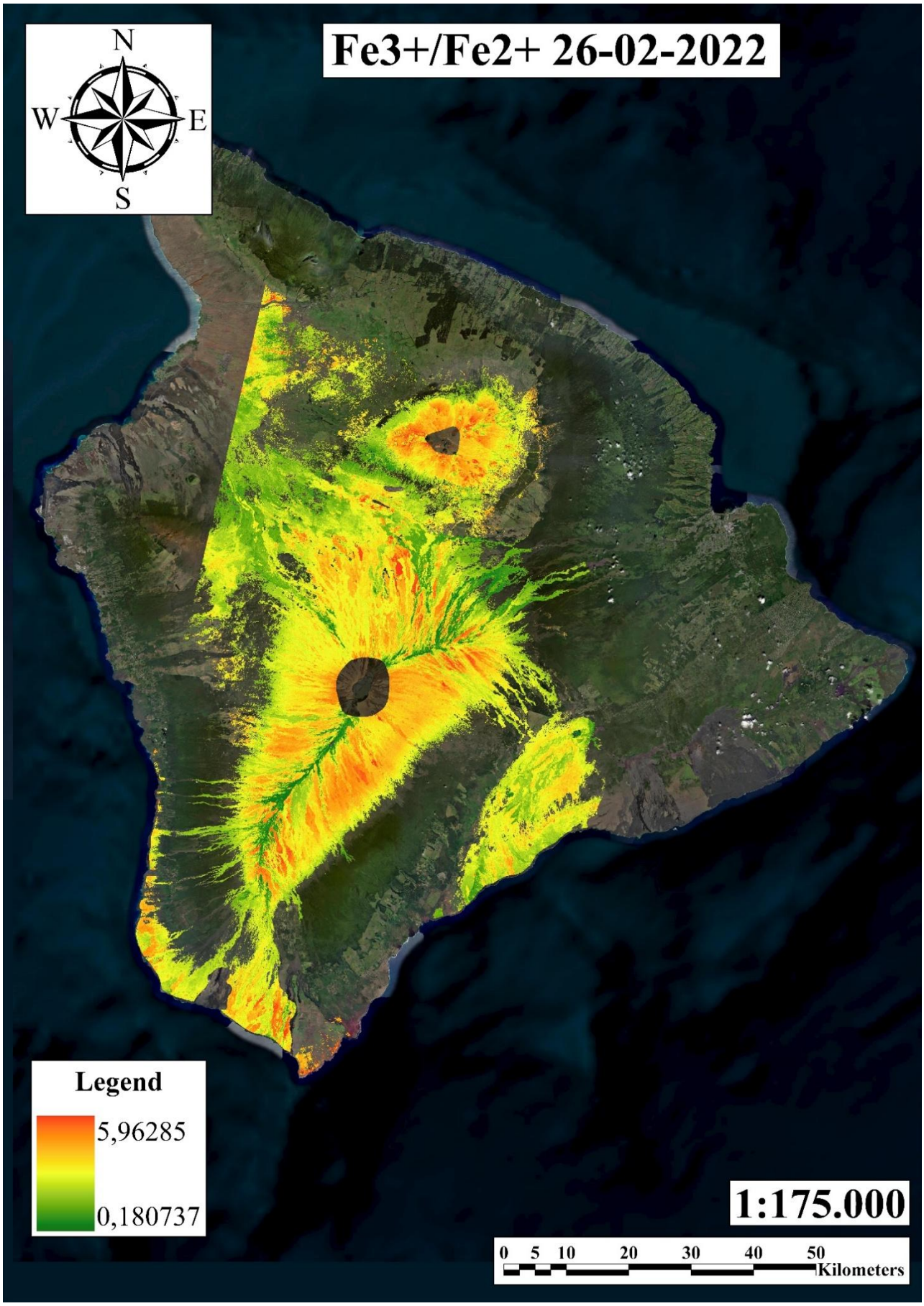

Fig. 50 Fe3+/Fe2+ index spectral signature image.

4. Conclusions

This research has systematically investigated the potential of satellite-based multispectral remote sensing, specifically leveraging Sentinel-2 imagery, for the relative dating of basaltic lava flows in diverse volcanic settings. The study proposes a scalable, cost-effective, and reproducible methodology capable of complementing traditional field-based approaches, which are often constrained by logistical, temporal, or safety limitations. Through the design and implementation of a structured workflow integrating the PolyGrid toolbox in a GIS environment, alongside rigorous band ratio analysis and moisture/infrared normalization procedures, this thesis has established a robust analytical framework. A wide array of spectral indices was tested, including those related to clay alteration, iron oxide formation, sulphur deposition, silica enrichment, and pyroxene weathering, each grounded in mineralogical and geochemical principles associated with post-eruptive surface evolution. The comparative analysis of these indices across four case studies Mount Etna, Stromboli, Grindavík region, and Hawai‘i Island provided critical insights into their relative performance and limitations. Indices sensitive to clay alteration and sulphur content, while conceptually promising, demonstrated high susceptibility to external environmental factors, such as precipitation events, biological colonization, and seasonal moisture variability. These confounding factors led to significant noise in the resulting reflectance patterns, ultimately limiting the applicability of these indices as consistent proxies for lava flow ageing. Conversely, the combined use of bivalent and trivalent iron indices, synthesized into the Fe^{3+}/Fe^{2+} ratio, emerged as the most reliable and robust indicator of relative lava flow age. This spectral metric effectively captured systematic oxidation processes occurring on basaltic surfaces over time, exhibiting minimal sensitivity to vegetation, moisture variability, or lithological heterogeneities. The results, validated through comparison with high-resolution geological maps and field-based chronological data, confirmed that this methodology is capable of resolving relative age differences at the scale of approximately one century. Such resolution is highly relevant for reconstructing volcanic chronologies, evaluating eruption

recurrence intervals, and informing hazard models. Furthermore, the case studies highlighted the importance of local geological, geomorphological, and microclimatic conditions in modulating reflectance-based signals. Processes such as hydrothermal alteration, secondary deposition of tephra, topographic controls on weathering rates, and anthropogenic factors can all introduce spatial artifacts that must be carefully considered. This emphasizes the necessity of integrating remote sensing observations with in-situ validation and pre-existing geological knowledge for rigorous, scientifically robust interpretations. By establishing a tested and validated framework for remote relative dating of lava flows, this research contributes a valuable tool for volcanic risk assessment and land-use planning in areas subject to volcanic hazards. Moreover, the scalability and repeatability of the method allow for its application across other volcanic fields worldwide, including regions where ground-based surveys are impractical or unsafe. This methodology also holds promise for comparative planetary geology, offering a transferable approach for the chronological reconstruction of volcanic surfaces on extraterrestrial bodies such as Mars or the Moon. Looking forward, future research should explore the integration of higher spectral resolution sensors, multi-temporal image series, and hyperspectral datasets to refine age discrimination even further. The adoption of advanced artificial intelligence and machine learning techniques could assist in overcoming environmental noise and enhancing the classification of spectral signatures. In addition, collaborative efforts combining satellite remote sensing, field mapping, and laboratory geochemical analyses could yield more comprehensive, multi-proxy age models, substantially improving both the precision and accuracy of volcanic surface dating. In conclusion, this thesis demonstrates that multispectral satellite data, when coupled with an appropriate analytical framework, can serve as an effective, efficient, and scientifically rigorous tool for estimating the relative ages of basaltic lava flows. The proposed methodology represents a significant advancement in remote volcanological research and provides a solid foundation for further methodological innovation, with far-reaching applications in the fields of hazard assessment, land management, and planetary exploration.

5. Limitations and Future Perspectives

While the methodology demonstrates high potential and reliability, certain limitations must be acknowledged. The accuracy of PolyGrid filtering is dependent on the quality and spatial resolution of the input satellite data, with lower-resolution imagery that potentially could introduce artifacts in polygon classification. Seasonal variations in vegetation and moisture content can influence NDVI thresholds, requiring dynamic calibration. Likewise, different environmental settings may necessitate distinct NDVI adjustments to ensure accurate vegetation masking. Additionally, some of the band ratios, although appearing robust, may be influenced by mineralogical heterogeneity across different lava flows, necessitating local adjustments. Future developments will aim to automate threshold calibration through machine learning techniques and to expand the PolyGrid toolbox by incorporating multi-temporal analysis capabilities. Furthermore, the integration of hyperspectral imagery and advanced spectral unmixing techniques represents a major future direction, as it would enable the detection of specific iron-bearing minerals rather than broader mineral groups or mixtures. Current satellite missions such as PRISMA, EnMAP, and EMIT already provide suitable hyperspectral data for this purpose, while upcoming platforms like CHIME are expected to significantly expand the availability and temporal coverage of such datasets. These advancements will enhance the scalability and precision of the methodology, better distinction of surface chemistry in volcanic monitoring and planetary geology. In conclusion, the methodology described provides a comprehensive and reproducible framework for estimating lava flow ages using satellite imagery. The integration of automated preprocessing via PolyGrid, carefully designed spectral ratios, and rigorous validation protocols highlights the potential of this approach for volcanic hazard assessment and geological research. This method enables large-scale analysis with high spatial resolution, complementing traditional field-based techniques and contributing valuable insights into volcanic landscape evolution.

An interesting direction for future research involves the potential to identify lithologies concealed beneath vegetation by analysing spatial and temporal variations in NDVI. Although vegetation typically obstructs direct reflectance analysis, it is hypothesized that plant response may, to some extent, be influenced by the underlying geological substrate. Differences in mineral composition and water retention capacity among rock types could affect vegetation density, species composition, and seasonal dynamics. By systematically analysing NDVI fluctuations over time and comparing them with areas of known geology, it may be possible to establish indirect correlations that can inform lithological interpretation. The integration of NDVI time series with climatic, pedological, and topographic data could further enhance the reliability of this approach, paving the way for non-invasive lithological mapping in vegetated regions.

5.1 Future work (Hyblean plateau)

An important avenue for future research, currently under development, concerns the refinement of mineralogical discrimination within sedimentary terrains by exploiting the capabilities of Sentinel-2 multispectral imagery. Specifically, a promising extension of the present methodology involves distinguishing between clay-rich units and carbonate (limestone) formations, with particular focus on the geological context of the Hyblean Plateau in southeastern Sicily. The Hyblean Plateau, located in southeastern Sicily, represents a geologically distinct sector of the African plate characterized by a predominantly carbonate-siliciclastic stratigraphy. Structurally defined as a foreland domain, it is bounded to the north by the Gela–Catania foredeep and to the west by the Malta Escarpment, marking the transition to the deep Ionian Basin. Among the key stratigraphic units exposed within the plateau, the Ragusa and Tellaro formations are of particular relevance for this study.

The Ragusa Formation, dating from the Upper Cretaceous to Paleocene, represents a phase of carbonate ramp development during a relatively stable tectonic regime, is subdivided into two main lithostratigraphic members:

Leonardo Member (Lower Ragusa Member): Characterized by well-cemented carbonate packstones alternated with marl-rich interbeds. These lithologies reflect deposition in a shallow-water carbonate ramp with episodic terrigenous input and moderate energy conditions.

Irminio Member (Upper Ragusa Member): Generally thicker and more variable, this member comprises grainstones and packstones with variable cementation, intercalated with marl layers and calcareous mudstones. Current stratigraphic scheme from available geological maps (Grasso et al., 2000)(Fig. 51) further subdivides the Irminio Member into three sub-units: a lower sequence of thick calcarenites separated by sandy horizons; an intermediate zone of decimetric calcarenite-marl alternations; and an upper part dominated by marly clays interbedded with thin limestone layers. This

fining-upward trend is interpreted as indicative of increasing basin subsidence and deepening depositional environments during the Burdigalian–Langhian transition.

Overlying the Ragusa Formation, the Tellaro Formation is mainly composed of marls, marly limestones, and clay-rich facies that span the Middle to Late Miocene. Its lithologies reflect more distal, deeper-water sedimentation and a shift towards pelagic-marine conditions with enhanced terrigenous input. The transition between the Ragusa and Tellaro formations is generally gradual, although in localized ancient structural highs (e.g. Ragusa High) it may be marked by angular unconformities attributed to Lower Miocene tectonic activity (Grasso et al. 1987).

The discrimination of clay deposits from surrounding limestones holds substantial importance for both stratigraphic reconstruction, geotechnical hazard assessment and hydrogeological modelling, given the variable mechanical and hydrological behaviour of these materials. The planned methodological enhancement will leverage targeted band ratios that exploit the spectral absorption features of key chemical components. In particular, the B02/B12 ratio is being investigated as a potential proxy for aluminium content associated with phyllosilicate minerals typically found in clay deposits. The aluminium-rich clays display characteristic absorption features in the visible blue range (captured by B02) relative to the shortwave infrared (captured by B12), enabling their separation from other lithologies. Conversely, the B11/B12 ratio is being explored to map carbonate-rich formations, capitalizing on the diagnostic absorption of calcite around 2.3 μm, which is sampled by Sentinel-2's shortwave infrared bands. By comparing these band ratios, it should be possible to delineate the spatial distribution of clay versus limestone, thus supporting more detailed geological mapping of the Hyblean Plateau. Future work will aim to calibrate these spectral indices against field-sampled reference materials and high-resolution geological maps. The integration of these new indices into the existing PolyGrid-based workflow will be tested to ensure compatibility with vegetation and moisture masking, as well as to validate their robustness under different seasonal and atmospheric conditions.

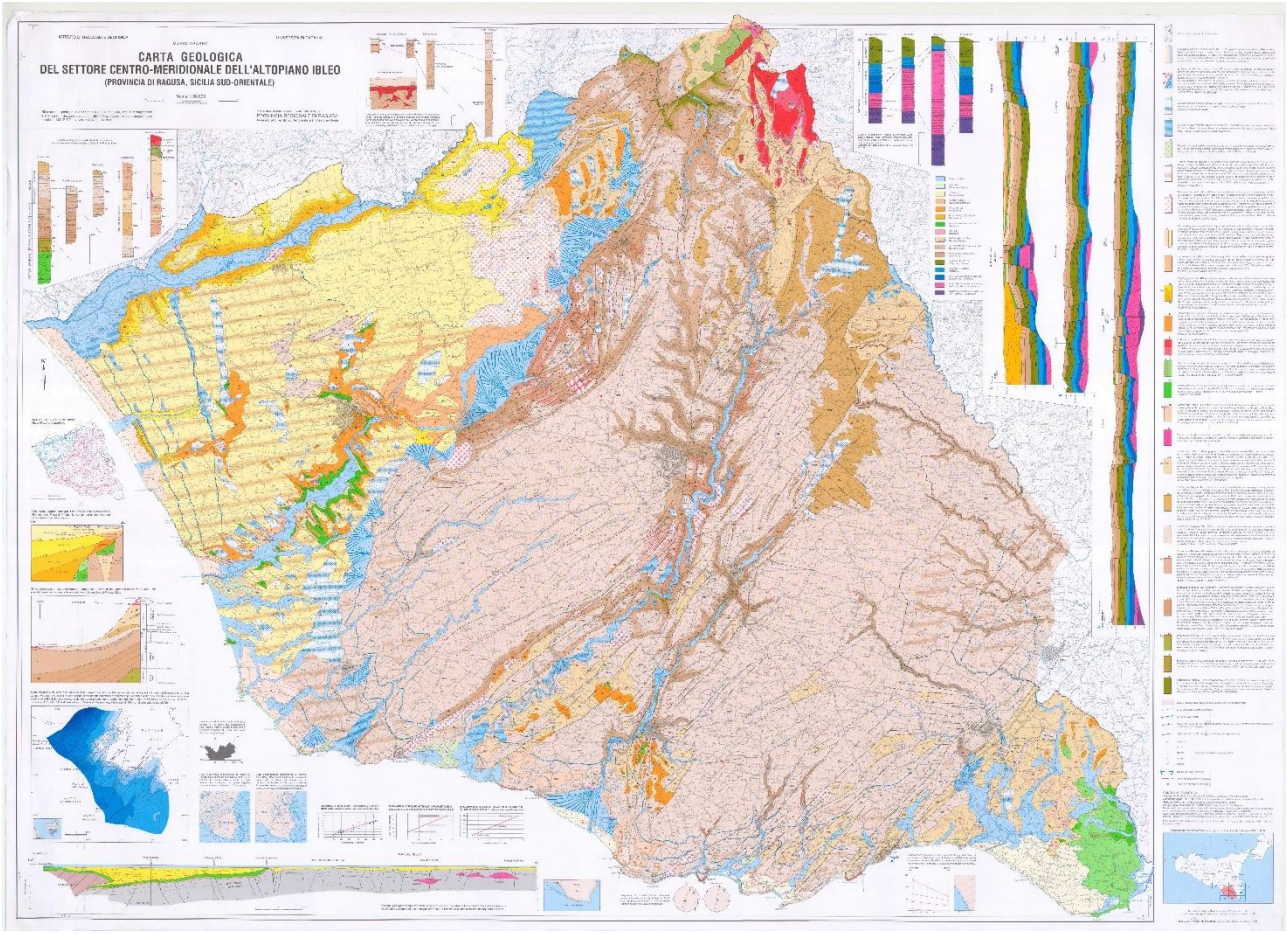

Fig. 51 Hyblean region geological map (Grasso et al., 2000)

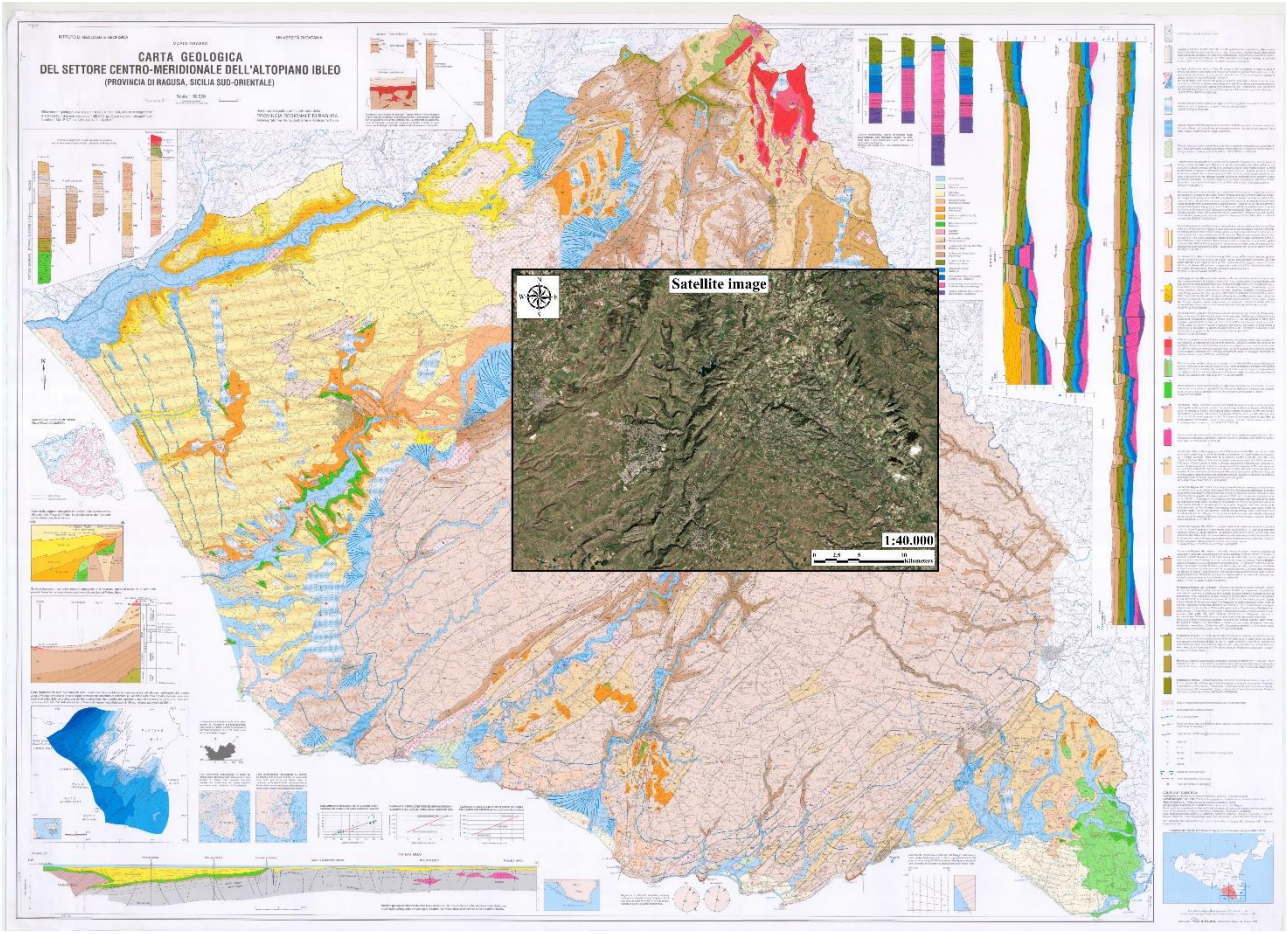

Fig. 52 Display of the 17-12-2024 images superimposed the geological map (Grasso at al., 2000)

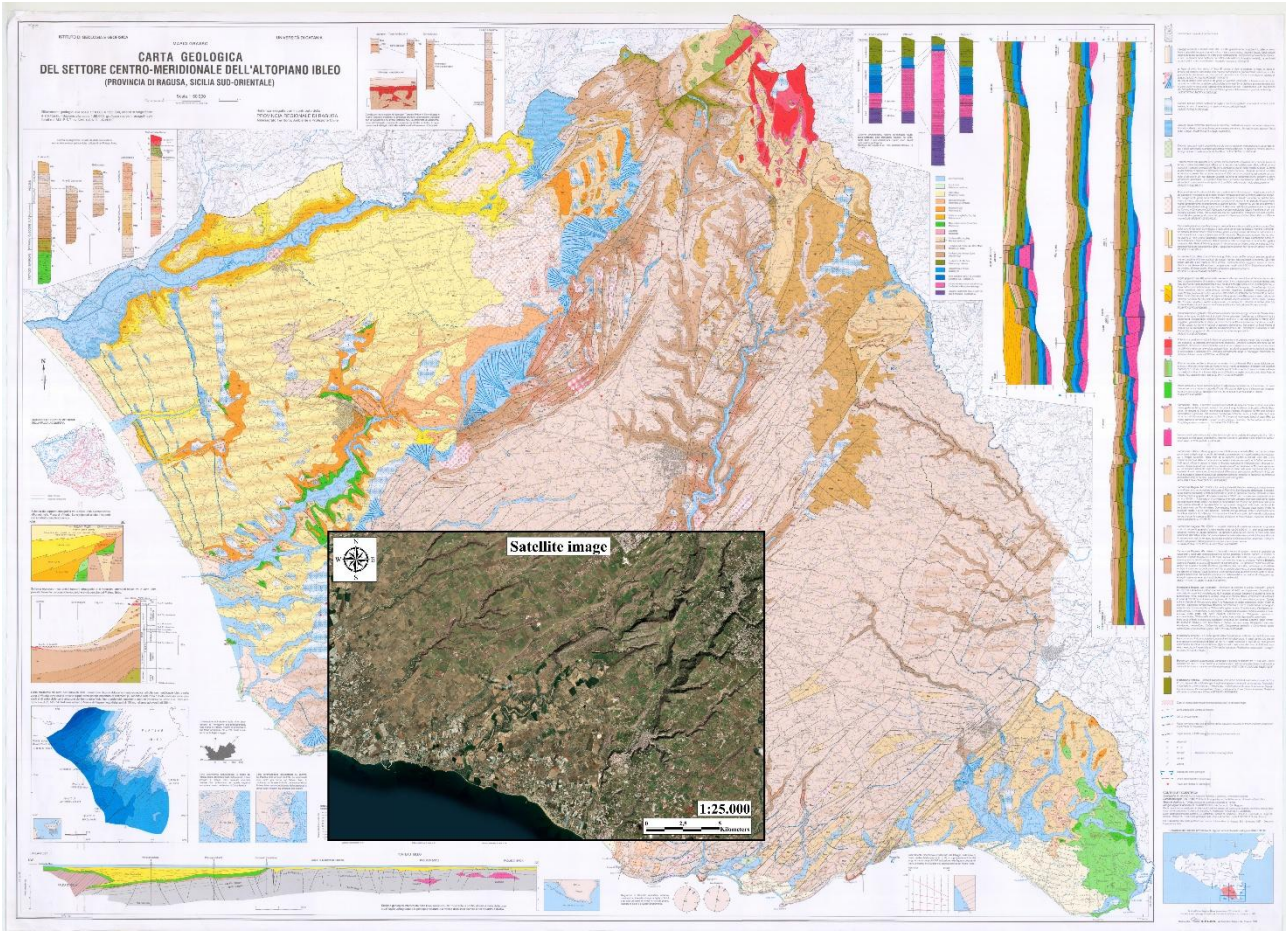

Fig. 53 Display of the 30-06-2025 images superimposed the geological map (Grasso at al., 2000)

5.2 Results

The method was first applied on images acquired in two different dates to compare different environmental conditions, 17-12-2024 (Fig. 52) to analyse winter conditions so higher humidity and wet soil, 30-06-2025 (Fig. 53) for summer conditions dryer soil. Even if future developments will be needed the first results are promising, the analysis can discriminate through clay or limestone outcropping rocks resulting in promising results. For a better visualization the two band ratios were combined resulting in a limestone/clay (calcite/aluminium) ratio image and vice versa, hereinafter referred to as Ca/Al for simplification.

17-12-2024

The Ca/Al band ratio image (Fig. 54) displays an enhanced spectral response corresponding to topographic/geological highs, where exogenic agents (such as weathering and erosion) have actively exposed the underlying limestone formations. These upland areas, being more susceptible to slope denudation and erosional processes, allow the carbonate bedrock to emerge clearly in the spectral data. Conversely, the adjacent lowland areas, naturally bounded by these geological highs, act as depositional environments that favour the accumulation of clay-rich sediments. Within these low-lying basins, the observed lower reflectance values in the Ca/Al ratio image confirm the reliability of the adopted remote sensing methodology in discriminating clayey materials from limestone rocks. In the northwestern sector of the study area, sand and calcarenite deposits infilling within the foredeep depression, exhibits higher calcite ratio values.

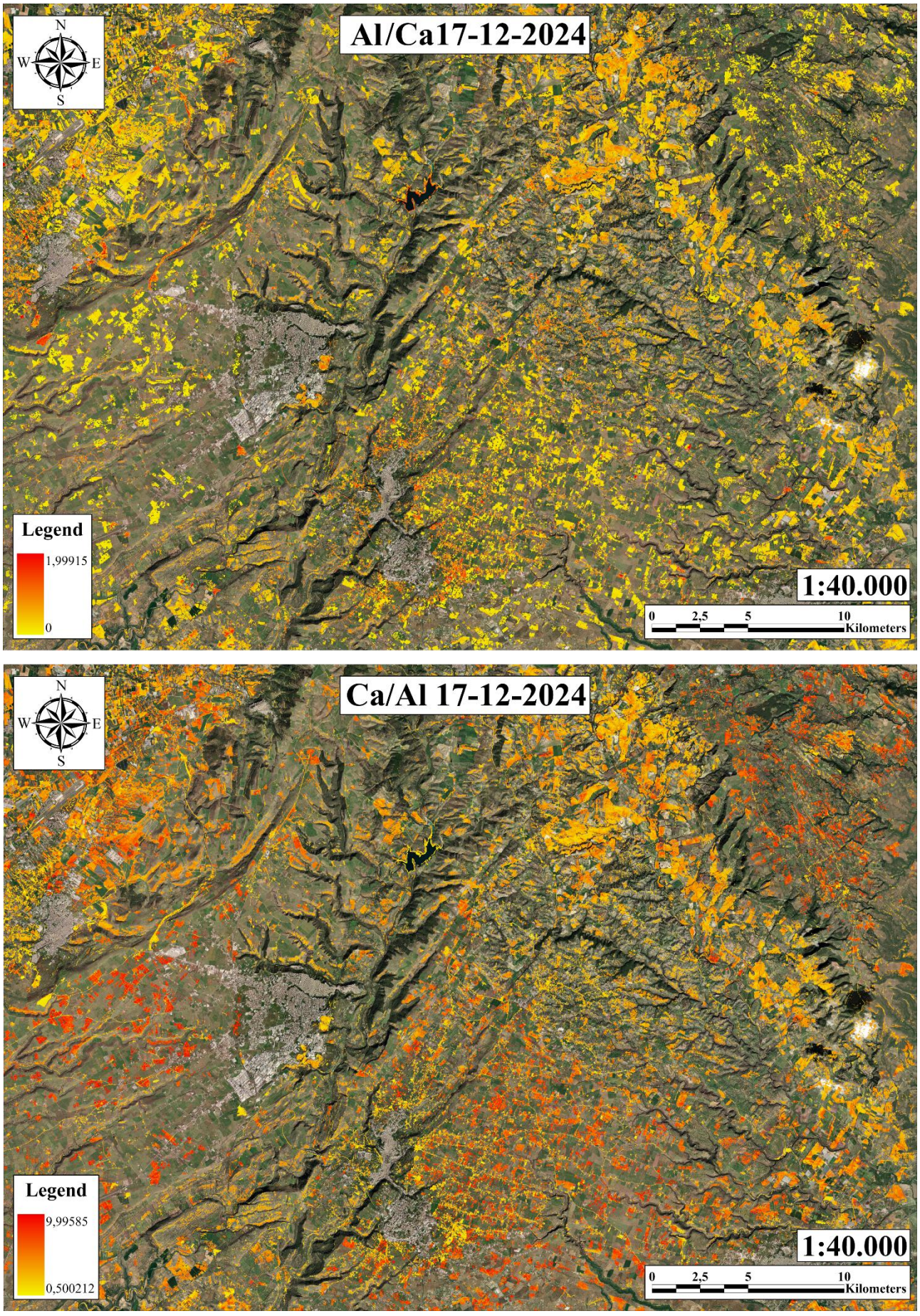

Fig. 54 Aluminium/calcite index spectral signature images of the Hyblean Plateau.

An additional point of interest emerging from the multispectral imagery analysis is the identification of clay extraction sites located in the southern sector of the study area (Fig. 55). These active quarry zones offer a unique opportunity to support and calibrate the spectral classification methodology. The recent excavation activities result in surfaces that are largely free of vegetation, thereby minimizing spectral contamination from biological cover and allowing for a clearer, more direct observation of lithological signatures in the reflectance data. The spectral characteristics of these zones are consistent with the known mineralogical composition of clay-rich deposits. As expected, the spectral response in the calcite-sensitive bands is notably low, indicating a limited presence of carbonate minerals. In contrast, spectral indices associated with aluminium-bearing minerals show markedly elevated values, confirming the clay-rich nature of the exposed material. The presence of these quarries serves as a valuable ground-truth reference. It allows for the refinement of spectral thresholds and enhances confidence in the interpretation of remotely sensed data, particularly in distinguishing between clay-rich and limestone units in more complex or vegetated areas of the landscape.

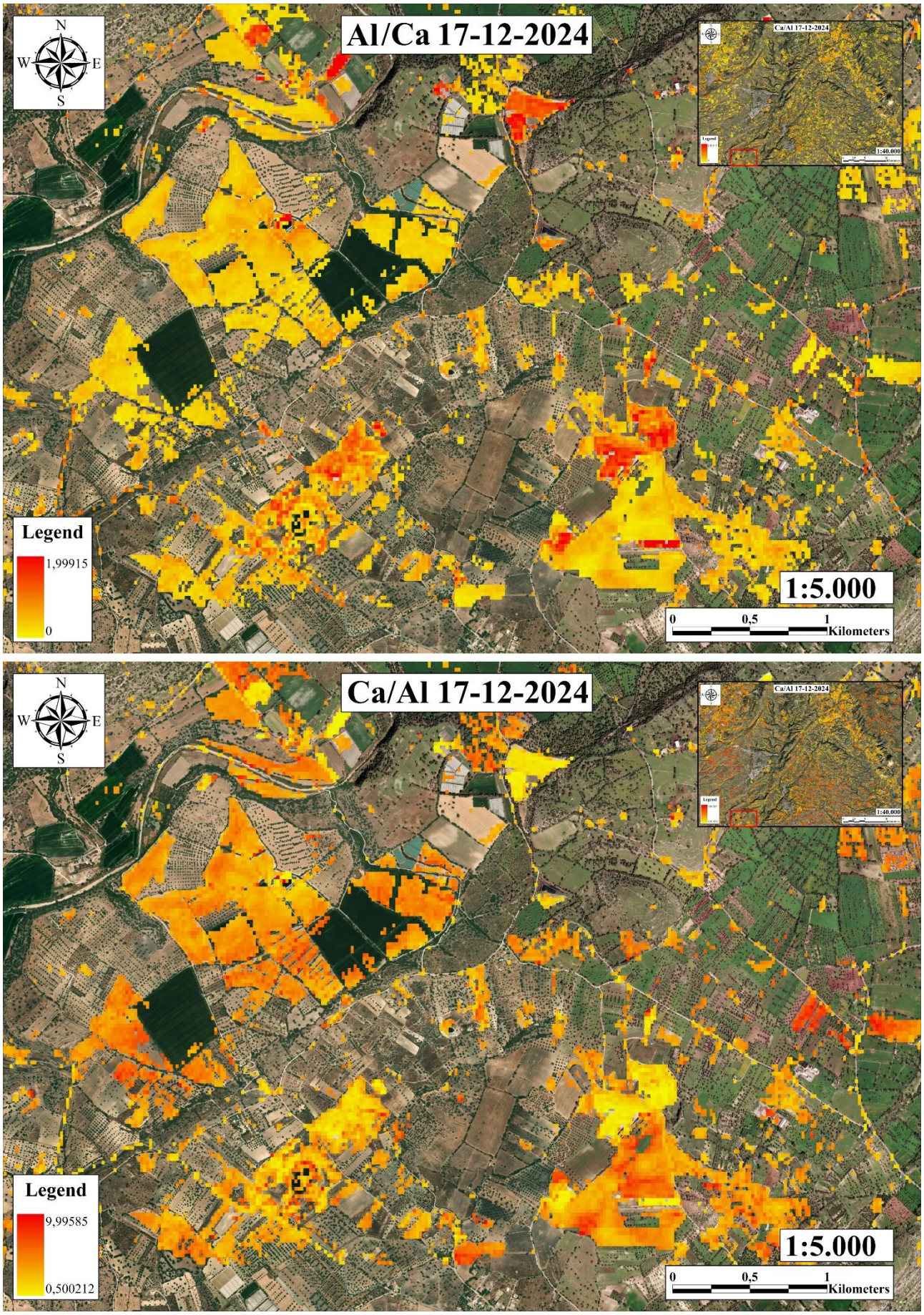

Fig. 55 Zoom of the clay quarries area.

30-06-2025

These images (Fig. 56) were specifically acquired in a more southern sector compared to those from 17-12-2024, with the objective of analysing an area where clay-rich deposits are predominant. As previously noted, the presence of active clay extraction sites serves as a valuable ground-truth reference to evaluate the reliability and discriminative power of the proposed reflectance-based method. In the northwestern portion of the scene, higher calcite values are observed, which are consistent with the emergence of the Ragusa Formation, a carbonate unit. In contrast, within the surrounding agricultural fields, some variability in the reflectance values is evident. These discrepancies can likely be attributed to anthropogenic influences, particularly agricultural practices such as liming. This technique, commonly adopted to correct soil acidity and reduce the phytotoxic effects of soluble aluminium, can lead to artificially elevated calcite signals in the spectral data. The central area is dominated by outcrops of the Tellaro Formation, which is exploited for clay extraction. Here, aluminium values generally increase, reflecting the clayey composition of the formation. However, this response is not homogeneous across the area. The observed spectral variability can be explained by the lithological heterogeneity of the Tellaro Formation itself, which includes interbedded clayey marls. These compositional variations may locally enhance the calcite signal, reducing the aluminium-to-calcite contrast and introducing minor fluctuations in the band ratio values. Nonetheless, the method remains effective in capturing the dominant compositional trends and highlights the importance of geological context in interpreting spectral responses.

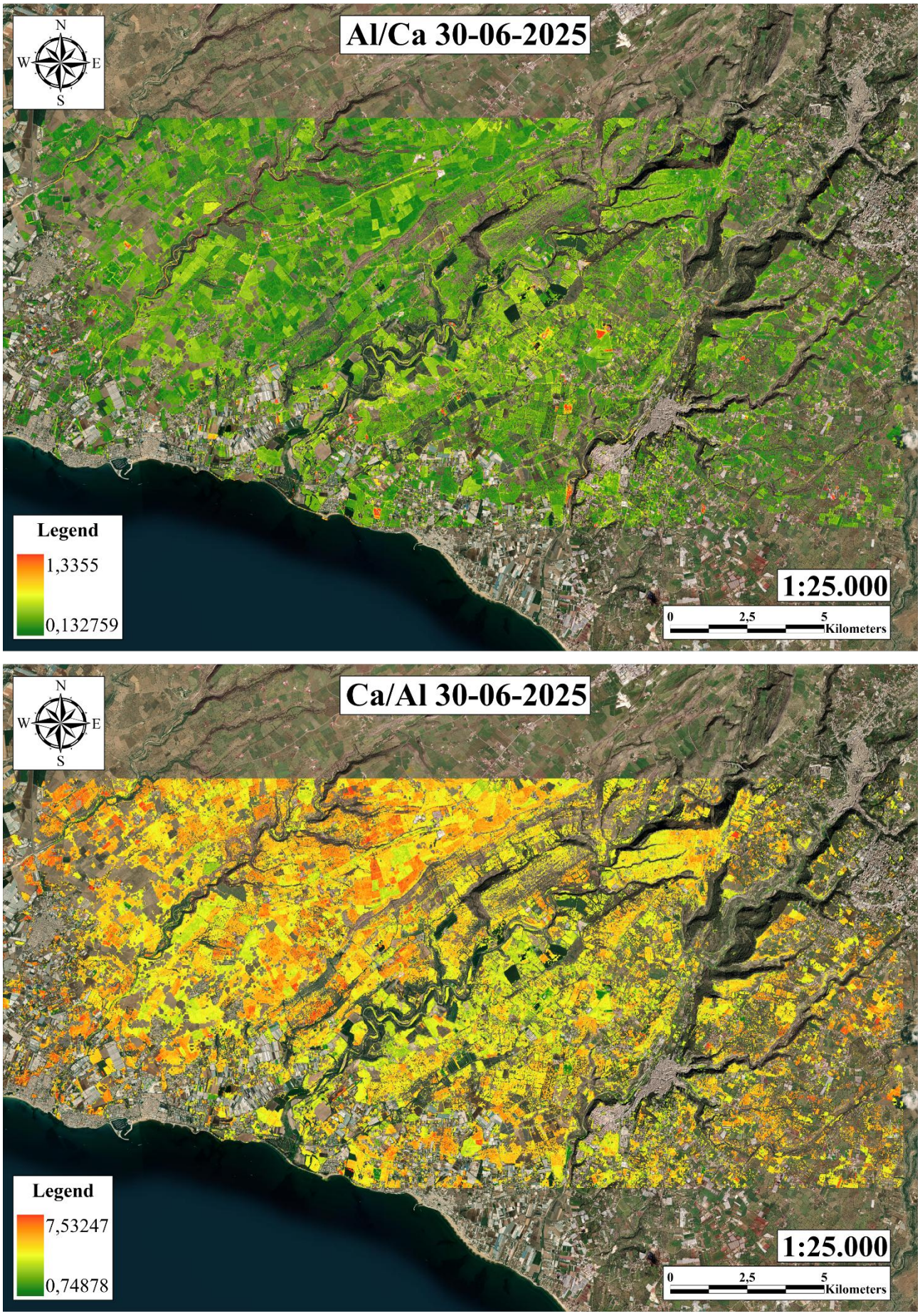

Fig. 56 Aluminium/calcite index spectral signature images of the Hyblean Plateau.

The detailed view of the quarry zone (Fig. 57) further confirms the capacity of the developed method to differentiate clay formations from limestone units. An interesting observation is the variability among the quarries themselves, which can be attributed to the lithological heterogeneity of the Tellaro Formation. This formation occasionally contains variable proportions of limestone mixed with clay, resulting in slightly higher calcite values in some quarry sectors. The presence of greenhouses with plastic coverings may introduce artefacts in the spectral analysis. Depending on the type and thickness of the plastic film used, these structures can exhibit moderate to high reflectance in the blue band (Band 02) and reduced reflectance in the Short-Wave Infrared (SWIR) bands. As a result, the aluminium band ratio may produce artificially elevated values, while the calcite band ratio appears suppressed. This spectral behaviour is not related to surface lithology but rather to the optical properties of the greenhouse materials, which must be carefully considered when interpreting results in agricultural or peri-urban areas.

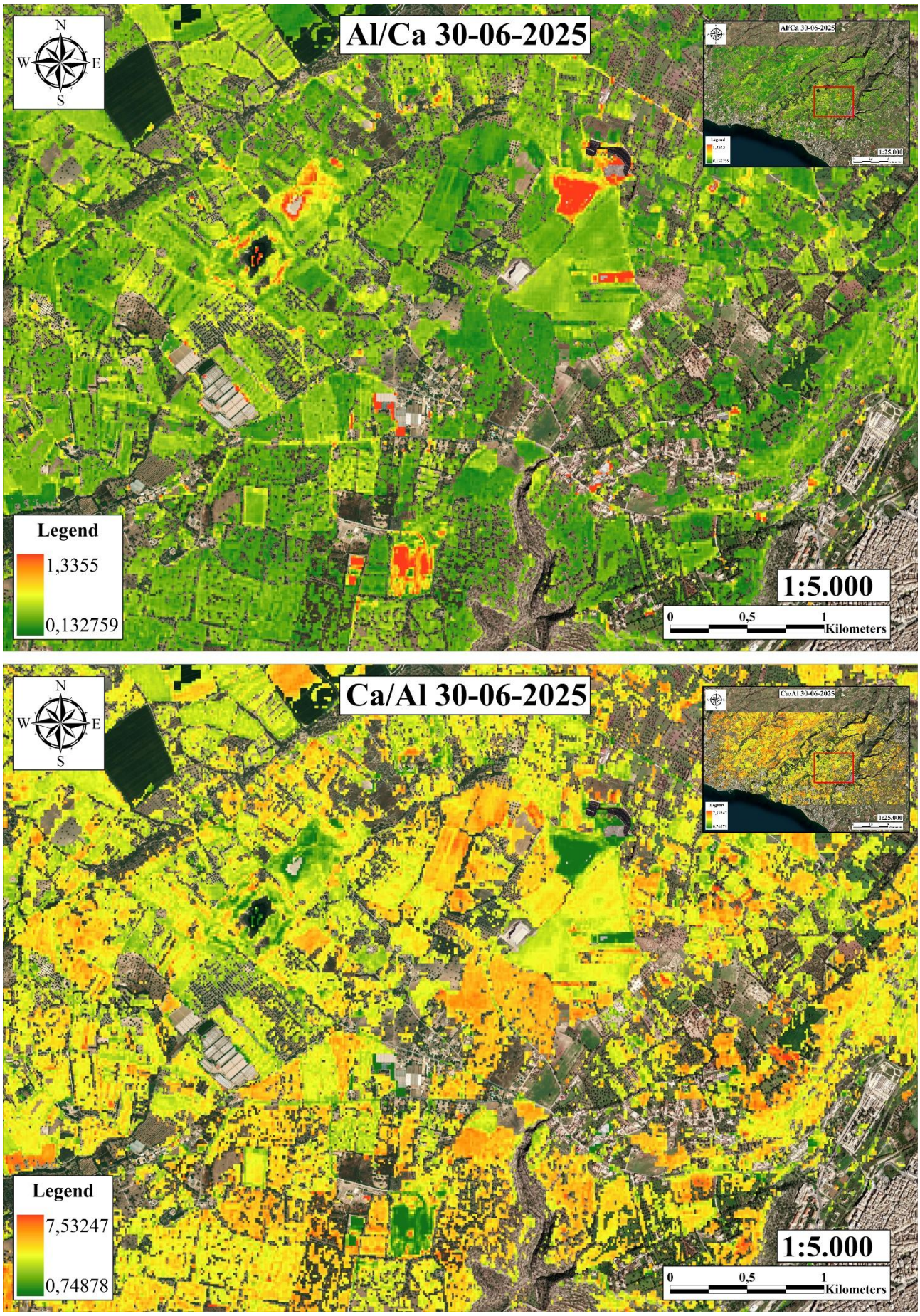

Fig. 57 Zoom of the clay quarries area.

Bibliography

Aloisi, M., Bonaccorso, A., & Gambino, S. (2006). Imaging compositional and density heterogeneities beneath Mount Etna volcano (Italy) by a joint inversion of gravity and self-potential data. Journal of Geophysical Research: Solid Earth, 111(B5). https://doi.org/10.1029/2005JB003905

Andronico, D., Corsaro, R. A., & Cristaldi, A. (2021). Eruptive dynamics and magma plumbing system of the 2021 Etna eruption. Bulletin of Volcanology, 83(59). https://doi.org/10.1007/s00445-021-01498-x

Arnórsson, S., Axelsson, G., & Sæmundsson, K. (2007). Geothermal systems in Iceland: Characteristics and conceptual models—II. High-temperature areas. Geothermics, 36(2), 131–151. https://doi.org/10.1016/j.geothermics.2007.03.004

Aschbacher, J., & Milagro-Pérez, M. P. (2012). The European Earth monitoring (GMES) programme: Status and perspectives. Remote Sensing of Environment, 120, 3–8. https://doi.org/10.1016/j.rse.2011.06.002

Aubele, J. C., Crumpler, L. S., & Elston, W. E. (1988). Zoning of lava flows: Implications for the study of volcanic surfaces on Mars. Icarus, 76(1), 18–27. https://doi.org/10.1016/0019-1035(88)90084-6

Azzaro R., Branca S., Gwinner K., Coltelli M. (2012). The volcano-tectonic map of Etna volcano, 1:100.000 scale: morphotectonic analysis from high-resolution DEM integrated with geologic, active faulting and seismotectonic data. It. J. Geosciences (Boll. Soc. Geol. It.), 131 (1), 153-170.

Bagnardi, M., et al. (2023). The 2021–2022 Fagradalsfjall eruption: Real-time geodetic modeling of magma intrusions in the Reykjanes Peninsula. Nature Communications, 14, 1024. https://doi.org/10.1038/s41467-023-36713-7

Barberi, F., Innocenti, F., & Villari, L. (1974). Chronology and petrology of the Aeolian volcanism in southern Tyrrhenian Sea: Geodynamic implications. Bulletin Volcanologique, 38(4), 1028–1052. https://doi.org/10.1007/BF02596878

Behncke, B., & Neri, M. (2003). The July–August 2001 eruption of Mt. Etna (Sicily). Bulletin of Volcanology, 65(7), 461–476. https://doi.org/10.1007/s00445-003-0274-1

Biessy, G., Dauteuil, O., Van Vliet-Lanoë, B., & Wayolle, A. (2008). Fast and partitioned postglacial rebound of southwestern Iceland. Tectonics, 27, TC3002. https://doi.org/10.1029/2007TC002177

Bonaccorso, A., et al. (2004). Magmatic processes leading to the July–August 2001 eruption of Mt. Etna (Italy): Insights from geophysical and geochemical data. Journal of Volcanology and Geothermal Research, 133(1–4), 139–160. https://doi.org/10.1016/S0377-0273(03)00392-7

Branca, S., & Del Carlo, P. (2005). Types of eruptions of Etna volcano AD 1670–2003: Implications for short-term eruptive behaviour. *Bulletin of Volcanology, 67*(8), 732–742. https://doi.org/10.1007/s00445-005-0412-z

Branca, S., Coltelli, M., Groppelli, G., & Lentini, F. (2011). Geological map of Etna volcano, 1:50,000 scale. Italian Journal of Geosciences, 130(3), 265–291. https://doi.org/10.3301/IJG.2011.15

Branca, S., Coltelli, M., Groppelli, G., & Lentini, F. (2011). Geological map of Etna volcano, 1:50.000 scale. Ital.J.Geosci. (Boll.Soc.Geol.It.), Vol. 130, No. 3 (2011), pp. 265-291, 16 figs., 3 tabs., 1 extra pl. (DOI: 10.3301/IJG.2011.15)

Calanchi, N., et al. (1993). Geology of the Panarea-Stromboli area (Aeolian Islands, southern Italy). Acta Vulcanologica, 3, 1–17.

Calvari, S., et al. (2004). Structural and eruptive evolution of Mount Etna during the past 100 ka. In A. Bonaccorso et al. (Eds.), Mt Etna: Volcano Laboratory (pp. 69–89). AGU Geophysical Monograph 143. https://doi.org/10.1029/143GM05

Calvari, S., et al. (2020). Monitoring and hazard mitigation at Stromboli volcano. Remote Sensing, 12(11), 1801. https://doi.org/10.3390/rs12111801

Chadwick, O. A., Vitousek, P. M., Hotchkiss, S., & Price, J. (2008). Vegetation-climate interactions on a gradient of substrate age in Hawaii. Ecology, 89(2), 456–466. https://doi.org/10.1890/06-1847.1

Chevrel, M. O., Harris, A. J. L., & Gurioli, L. (2021). Multispectral remote sensing of lava flows: A review of applications and perspectives. Remote Sensing, 13(6), 1124. https://doi.org/10.3390/rs13061124

Chiocci, F. L., et al. (2008). Large-scale flank collapse of Stromboli volcano, Aeolian Islands, Italy. Geology, 36(11), 951–954. https://doi.org/10.1130/G25064A.1

Cigna, F., Tapete, D., & Solari, L. (2013). Volcanic lava flow mapping from space using multispectral and SAR data: The Mount Etna eruption of May 2008. Remote Sensing of Environment, 134, 160–175. https://doi.org/10.1016/j.rse.2013.03.003

Clague, D. A., & Dalrymple, G. B. (1987). The Hawaiian-Emperor volcanic chain. Part I. Geologic evolution. USGS Professional Paper 1350.

Clague, D. A., & Sherrod, D. R. (2014). Growth and degradation of Hawaiian volcanoes. USGS Professional Paper 1801.

Corsaro, R. A., Miraglia, L., & Andronico, D. (2017). Lava fountains during Etna's 2015 eruption: Insights into summit eruptive dynamics and implications for gas release. Journal of Volcanology and Geothermal Research, 341, 53–65. https://doi.org/10.1016/j.jvolgeores.2017.05.017

Davis, A. S., & Clague, D. A. (1990). Volcanic history of the submarine Loihi Seamount, Hawaii. Journal of Volcanology and Geothermal Research, 42(3–4), 235–254. https://doi.org/10.1016/0377-0273(90)90018-E

De Beni E., Branca S., Coltelli M., Groppelli G. & Wijbrans J.R. (2011). 40Ar/39Ar isotopic dating of Etna volcanic succession. It. J. Geosci., 130 (3), 292-305. doi: 10.3301/IJG.2011.14

Dewey, J.F., Helman, L.M., Turco, E., Hutton, D.W.H., Knott, S.D., 1989. Kinematics of the western Mediterranean. Spec. Publs. Geol., Soc. London 45, 265–283.

Di Traglia, F., et al. (2014). The July–August 2014 effusive eruption at Stromboli volcano (Italy): Timeline and eruptive mechanisms. Journal of Volcanology and Geothermal Research, 286, 98–113. https://doi.org/10.1016/j.jvolgeores.2014.08.002

Drusch, M., et al. (2012). Sentinel-2: ESA's optical high-resolution mission for GMES operational services. Remote Sensing of Environment, 120, 25–36. https://doi.org/10.1016/j.rse.2011.11.026

Einarsson, P. (2008). Plate boundaries, rifts and transforms in Iceland. Jökull, 58, 35–58.

European Commission. (2015). Copernicus User Guide. https://www.copernicus.eu/en

Faccenna, C., Becker, T. W., Lucente, F. P., Jolivet, L., & Rossetti, F. (2007). Slab roll-back, trench retreat, and back-arc extension in the Mediterranean region. Nature, 446, 859–862. https://doi.org/10.1038/nature05651

Francalanci, L., et al. (2013). Magma plumbing system and structure of Stromboli volcano: Insights from petrology, seismicity and geodesy. Lithos, 180–181, 49–65. https://doi.org/10.1016/j.lithos.2013.08.019

G. Biessy, O. Dauteuil, B. Van Vliet-Lanoe¨ & A. Wayolle (2008). Fast and partitioned postglacial rebound of southwestern Iceland. *Tectonics*, 27, TC3002, doi:10.1029/2007TC002177.

Garcia, M. O., Caplan-Auerbach, J., De Carlo, E. H., Kurz, M. D., & Becker, N. (2006). Geology, geochemistry, and earthquake history of Lō‘ihi Seamount, Hawai‘i's youngest volcano. Chemie der Erde, 66(2), 81–108. https://doi.org/10.1016/j.chemer.2005.09.002

Garcia, M. O., et al. (2007). Petrology, geochemistry, and geochronology of Hawaiian volcanism: Hotspot and mantle dynamics. In G. R. Foulger & D. M. Jurdy (Eds.), Plates, plumes and planetary processes. Geological Society of America. https://doi.org/10.1130/2007.2430(04)

Gillespie, A. R., Kahle, A. B., & Walker, R. E. (1986). Color enhancement of highly correlated images. I. Decorrelation and HSI contrast stretches. Remote Sensing of Environment, 20(3), 209–235. https://doi.org/10.1016/0034-4257(86)90044-1

Gíslason, S. R., et al. (2024). Volcanic hazards in the Reykjanes Peninsula: Lessons from the recent eruptions near Grindavík. Journal of Volcanology and Geothermal Research, 438, 107679. https://doi.org/10.1016/j.jvolgeores.2024.107679

Gómez, C., Hayashi, S., & Ito, Y. (2016). Monitoring and assessing the evolution of a lava dome using Sentinel-2A data. Remote Sensing, 8(11), 954. https://doi.org/10.3390/rs8110954

Grasso, M., Lentini, F., & Carbone, S. (1987). Carta geologica del settore nord-orientale Ibleo (Sicilia sud-orientale), 1:50,000. In Lineamenti geologici del Plateau Ibleo (Sicilia S.E.): presentazione delle

carte geologiche della Sicilia sud-orientale. Memorie della Società Geologica Italiana, XXXVIII, fasc. unico.

Gurenko, A. A., et al. (2022). Mantle melting and melt ascent beneath Reykjanes from the 2021 Fagradalsfjall lavas. Geochimica et Cosmochimica Acta, 317, 72–93. https://doi.org/10.1016/j.gca.2021.11.027

Gvirtzman, Z., & Nur, A. (1999). The formation of Mount Etna as the consequence of slab rollback. Nature, 401, 782–785. https://doi.org/10.1038/44555

Harris, A. J. L., & Ripepe, M. (2007). Synergy of multiple geophysical approaches to understand volcanic processes: An example from Stromboli. Geophysical Research Letters, 34(5), L05301.

Harris, A. J. L., & Rowland, S. K. (2001). Flow geometry and effusion rate at Hawai‘i’s Pu‘u ‘Ō‘ō vent during April–September 1997: Insights from satellite and field data. Bulletin of Volcanology, 63, 110–124. https://doi.org/10.1007/s004450100124

Jakobsson, S. P., et al. (1978). Geology of the Reykjanes Peninsula: Geological map and description. National Energy Authority Report OS JHD 78.

Keller, J., Hornig-Kjarsgaard, I., Koberski, U., Stadlbauer, E., & Lenhart, R. (1993). Carta geologica dell’isola di Stromboli / Geological map of the island of Stromboli (scale 1:10,000). Freiberg: Mineralogisch-Petrografisches Institut der Universität.

Kervyn, M., et al. (2010). Remote sensing of volcanoes: A review of advances and challenges.

Kokaly, R. F., Clark, R. N., Swayze, G. A., Livo, K. E., Hoefen, T. M., Pearson, N. C., ... & Team, U.S.G.S. (2017). USGS Spectral Library Version 7. U.S. Geological Survey Data Series 1035. https://doi.org/10.3133/ds1035

Kuenzer, C., & Dech, S. (Eds.). (2013). Remote sensing time series: Revealing land surface dynamics. Springer.

Lanzafame, G., & Bousquet, J. C. (1997). The Maltese escarpment and its role in the tectonic evolution of the Mt. Etna region (Sicily). Tectonophysics, 281(1–2), 43–55.

Lentini, F., Carbone, S. & Catalano, S. (1994). Main structural domains of the central Mediterranean region and their Neogene tectonic evolution. Bollettino di geofisica Teorica ed Applicata, 36, 103.125.

Lockwood, J. P., & Lipman, P. W. (1987). Holocene eruptive history of Mauna Loa volcano. USGS Professional Paper 1350.

Macdonald, G. A., Abbott, A. T., & Peterson, F. L. (1983). Volcanoes in the sea: The geology of Hawaii. University of Hawaii Press.

McDougall, I., & Swanson, D. A. (1972). Potassium-argon ages of lavas from the Hawi and Pololu volcanic series, Kohala volcano, Hawaii. Geological Society of America Bulletin, 83(12), 3731–3738.

Métrich, N., et al. (2005). Summit activity of Stromboli volcano (Italy) during the 2002–2003 crisis: Insights from petrology and geochemistry. Journal of Volcanology and Geothermal Research, 146(1–3), 131–152.

Moore, R. B., & Clague, D. A. (1991). Volcanic geology and eruption frequency, south flank of Hualālai volcano, Hawaii. Bulletin of Volcanology, 53(8), 602–611.

Neal, C. A., et al. (2019). The 2018 rift eruption and summit collapse of Kīlauea Volcano. Science, 363(6425), 367–374.

Náttúrufræðistofnun Íslands (Icelandic Institute of Natural History). (2014). Geological map of Iceland – Bedrock geology (scale 1:600,000). Reykjavík, Iceland: Náttúrufræðistofnun Íslands.

Neri, M., Behncke, B., & Branca, S. (2011). Lava flow hazard at Mount Etna (Italy): Mapping of the exposed population and infrastructures. Natural Hazards, 58, 1071–1088. https://doi.org/10.1007/s11069-011-9713-0

Orsi G. (2022). Voclanic and deformation history of the campi Flegrei Voclanic Field, Italy. Springer Nature 2022, G. Orsi et al. (eds.), Campi Flegrei, Active Volcanoes of the World, https://doi.org/10.1007/978-3-642-37060-1_1

Peate, D. W., et al. (2010). Petrogenesis of basalts from the Reykjanes Ridge and Peninsula: The role of melting depth and source heterogeneity. Journal of Petrology, 51(7), 1405–1445.

Pichavant, M., et al. (2013). Degassing and crystallization of Stromboli basaltic magmas: Constraints from high-pressure experiments. Chemical Geology, 343, 134–145.

Pieri, D., & Abrams, M. (2004). ASTER watches the world's volcanoes: A new paradigm for volcanological observations from orbit. Journal of Volcanology and Geothermal Research, 135(1–2), 13–28. https://doi.org/10.1016/j.jvolgeores.2003.12.018

Porter, S. C. (1979). Hawaiian glacial ages. Quaternary Research, 12(2), 161–187.

Ramsey, M. S., & Flynn, L. P. (2004). Strategies for the remote detection of volcanic activity using multispectral thermal infrared data. Journal of Volcanology and Geothermal Research, 135(1–2), 127–146. https://doi.org/10.1016/j.jvolgeores.2003.12.017

Remote Sensing of Environment, 113(9), 1827–1831.

Romagnoli, C., et al. (2022). Tsunamigenic potential of Stromboli volcano: Marine geophysical evidence of submarine landslides. Scientific Reports, 12, 4931.

Romagnoli, C., Kokelaar, P., Casalbore, D., & Chiocci, F. L. (2009). Lateral collapses and active sedimentary processes along the volcanic island of Stromboli, Italy. *Marine Geology, 265*(3–4), 191–207. https://doi.org/10.1016/j.margeo.2009.07.004

Rosi, M., et al. (2000). Volcano-tectonic evolution of Stromboli volcano (Aeolian Islands, Italy). Acta Vulcanologica, 12(1–2), 163–182.

Rosi, M., et al. (2006). Warning system for paroxysmal explosions at Stromboli volcano (Italy). Bulletin of Volcanology, 69, 501–514.

Rowland, S. K., & Walker, G. P. L. (1987). Morphometric analyses of lava flows in Hawaii. Bulletin of Volcanology, 49, 631–641. https://doi.org/10.1007/BF01080347

Rust, D., & Neri, M. (1996). The structure and evolution of Mount Etna: Recent results and developments. Journal of Volcanology and Geothermal Research, 71(1), 1–10.

Serpelloni, E., Vannucci, G., Pondrelli, S., Argnani, A., Casula, G., Anzidei, M., Baldi, P., Gasperini, I., 2007. Kinematics of the Western Africa-Eurasia plate boundary from focal mechanisms and GPS data. Geophysical Journal International 169, 1180–1200. http://dx.doi.org/10.1111/j.1365-246X.2007.03367.x.

Sæmundsson, K. (1979). Outline of the geology of Iceland. Jökull, 29, 7–28.

Sæmundsson, K., et al. (2020). The volcanotectonic evolution of the Reykjanes Peninsula. Iceland GeoSurvey Report ISOR-2020/013.

Sigmundsson, F., et al. (2022). Magma plumbing system of the 2021–2022 Reykjanes Peninsula eruptions. Science, 376(6594), 845–850.

Thordarson, T., & Larsen, G. (2007). Volcanism in Iceland in historical time: Volcano types, eruption styles and eruptive history. Journal of Geodynamics, 43(1), 118–152.

Tibaldi, A. (2001). Multiple sector collapses at Stromboli volcano, Italy: How they work. Bulletin of Volcanology, 63(2–3), 112–125.

Trusdell, F. A. (1995). Lava flow hazards and risk assessment on Mauna Loa volcano, Hawaii. U.S. Geological Survey Bulletin, 2139. https://pubs.usgs.gov/bul/b2139/

USGS. (2022–2024). Hawaiian Volcano Observatory reports and eruption data. https://www.usgs.gov/observatories/hvo

USGS. (n.d.). Kīlauea Volcano—Current Activity. U.S. Geological Survey. https://www.usgs.gov/volcanoes/kilauea

Van der Meer, F. D., van der Werff, H. M. A., & van Ruitenbeek, F. J. A. (2014). Remote sensing for mineral exploration. Geological Society, London, Special Publications, 393(1), 17–27. https://doi.org/10.1144/SP393.4

Viccaro, M., Nicotra, E., Cannata, A., & Palano, M. (2019). The magma plumbing system of Mt. Etna (Italy): A review of geophysical, petrological and geochemical data. Earth-Science Reviews, 194, 291–313.

Viviano-Beck, C. E., et al. (2014). Revised CRISM spectral parameters and summary products based on the currently detected mineral diversity on Mars. Journal of Geophysical Research: Planets, 119(6), 1403–1431.

Wilson, J. T. (1963). A possible origin of the Hawaiian Islands. Canadian Journal of Physics, 41(6), 863–870.

Wolfe, E. W., Wise, W. S., & Dalrymple, G. B. (1997). Geologic map of the Island of Hawai‘i (scale 1:100,000). U.S. Geological Survey, Miscellaneous Investigations Series Map I-2524-A. Reston, VA: U.S. Department of the Interior.